2 ey

UCRL-19809

MASTER

RESONANCE PRODUCTIONS IN K^+p INTERACTIONS AT 4.6 GeV/c AND 9 GeV/c

Chumin Fu
(Ph.D. Thesis)

August 10, 1970

AEC Contract No. W-7405-eng-48

LRL

LAWRENCE RADIATION LABORATORY
UNIVERSITY of CALIFORNIA BERKELEY

UCRL-19809

DISCLAIMER

PAGES ___i___to___ii___

WERE INTENTIONALLY

LEFT BLANK

RESONANCE PRODUCTIONS IN K^+p INTERACTIONS AT 4.6 GeV/c AND 9 GeV/c

Contents

RESONANCE PRODUCTIONS IN K^+p INTERACTIONS AT 4.6 GeV/c AND 9 GeV/c

Chumin Fu

Lawrence Radiation Laboratory
University of California
Berkeley, California 94720

August 10, 1970

ABSTRACT

This thesis is a study of the reaction $K^+p \to K^+\pi^-\pi^+p$ at 9 GeV/c and 4.6 GeV/c. The Brookhaven National Laboratory 80-inch hydrogen bubble chamber was employed for both experiments. We find that one-pion exchange (OPE) plays a very important role in both the $K^{*o}_{890}\Delta^{++}_{1236}$ and the $K^{*o}_{1420}\Delta^{++}_{1236}$ double resonance productions and the low $\Delta^{++}_{1236}\pi^-$ mass enhancement in the $K^+\pi^-\Delta^{++}_{1236}$ channel. The decay properties of the double resonance channels indicate that OPE dominates over a larger t range in the lower energy (4.6 GeV/c) data than in the higher energy (9 GeV/c) data. In the small $K^+\pi^-$ mass region $[M(K^+\pi^-) < 1.54$ GeV$]$, the contribution from the non-pion exchange is not negligible for $|t'| \gtrsim 0.05$ $(\text{GeV/c})^2$ at 9 GeV/c and $|t'| \gtrsim 0.3$ $(\text{GeV/c})^2$ at 4.6 GeV/c. It becomes more important as $|t'|$ increases. Thus a $K\pi$ scattering analysis can be performed only in a region where the $|t'|$ values lie below these limits. A mass peak at ~ 1.1 GeV in the $K^+\pi^-$ mass spectrum is observed in the large $|t'|$ region $[|t'| \geq 0.05$ $(\text{GeV/c})^2]$ in the $K^+\pi^-\Delta^{++}_{1236}$ channel at 9 GeV/c. Presumably it is produced mainly via non-pion exchange.

The low $\Delta^{++}_{1236}\pi^-$ mass enhancement can be described by a double peripheral model. The dominant mechanism is a Pomeron and a pion (P,π) double Regge-pole exchange. The model gives good agreement with the data provided

that both $-t_{K^+ \to K^+}$ and $-t_{p \to \Delta^{++}}$ are less than 0.5 $(\mathrm{GeV}/c)^2$ and $M(K^+\pi^-) \geq 1.54$ GeV. Problems involved with the extrapolation into the small $K^+\pi^-$ mass region are discussed. The importance of the contribution from the extrapolation and its implication to the $K\pi$ scattering analysis are also investigated.

I. INTRODUCTION

A large amount of experimental data has been accumulated over the last decade, yet by no means is it well understood. At present only first order experimental facts have been established with little uncertainty; more detailed results are usually open to individual interpretations. They are quite often model dependent, sometimes even reaction dependent. Thus it is preferable to study many reactions at various energies to find out the regularities and the differences among those reactions. Then one can try to interpret them in a consistent manner.

In this thesis we emphasize the general features of the reaction $K^+p \to K^+\pi^-\pi^+p$ at 9 and 4.6 GeV/c.[1] Similar features are also observed in the $\pi^\pm p$ experiments in the same energy range. The production of resonance is one of the important topics we discuss here. However due to the limitation of the statistical level of the data and the uncertainties involved in the data, only the very dominant resonances, Δ^{++}_{1236}, K^{*o}_{890}, and K^{*o}_{1420} are studied in great detail. Any secondary effects depend highly on how one assumes the background. In general the background is defined according to one's interest. Here we are mainly concerned with the information of the $K\pi$ scattering that can possibly be extracted from the reaction $K^+p \to K^+\pi^-\Delta^{++}_{1236}$.[1a] We are particularly interested in the problems related to the controversial $K\pi$ s wave. To obtain a clean sample of one-pion exchange, we study the effects of the non-pion exchanges and eliminate them from the sample. We furthermore investigate the possible contribution of the nonresonant background from the double peripheral processes that produce the low $\Delta^{++}\pi^-$ mass enhancement.[1b] Effects of the various backgrounds to the $K\pi$ scattering problem are also discussed. In Section II we describe the general features of the reaction $K^+p \to K^+\pi^-\pi^+p$, namely the resonances production, low mass enhancements, and the peripheral nature of the data. Section III discusses the double resonance productions, $K^{*o}_{890}\Delta^{++}_{1236}$, $K^{*o}_{1420}\Delta^{++}_{1236}$, and some effect from the high-mass Δ^{++}'s that are associated with the K^{*o}_{890} production. Finally, in Section IV we discuss both the production and the decay properties of the $K\pi$ system in the $K^+\pi^-\Delta^{++}_{1236}$ channel. Appendix I, which is a modification of a paper to be published in Physical Review,[1b] includes a detailed discussion of a double peripheral model analysis for the low $\Delta^{++}\pi^-$ mass enhancement. Both the extension in the t variables and the extrapolation into the small subenergies are investigated. The experimental details and the cross-section calculation are given in Appendix II.

II. GENERAL FEATURES OF THE DATA

The well-known common dominant features in the hadron-hadron collisions leading to the four-body final states at high energy[2] are:

1) The peripheral nature, which is characterized by the small momentum transfer between the particles in the final state and one of the particles in the initial state.

2) The resonance productions, which means that the particles in the final states are the decay products of some resonance(s) in an intermediate stage.

3) The low-mass enhancements that occur near the threshold of a group of particles in the final states that has the same set of internal quantum numbers as one of the particles in the initial state, except possibly the spin and parity J^P. For meson resonance productions in the kaon or the pion-induced reactions, the spin parity of the resonance should be in the series 0^-, 1^+, 2^-, ..., which is usually called the unnatural parity series. The width of enhancements of this type is usually around 0.1 to 0.4 GeV.[3]

All these features and their general properties are discussed in Sections II-A through II-D.

Throughout this thesis the exchange model is used to explain the various reactions leading to the $K^+\pi^-\pi^+p$ final state. To agree on the terminologies and conventions adopted here we consider the reaction $K^+p \rightarrow K^+\pi^-\Delta^{++}_{1236}$ as shown in Fig. 1a. The incident positive kaon, K^+_{inc}, hits the target proton p with some object "e" exchanged between the K^+_{inc} and the p. The proton turns into a Δ^{++}_{1236} and the K^+_{inc} is scattered by the virtual object "e" and ends up with two particles K^+ and π^-, which may or may not be from a $(K\pi)^0$ resonant intermediate state. To fix our attention we consider the $K\pi$ system at the upper vertex. We adopt the Gottfried-Jackson frame,[4] a $K\pi$ rest frame with the z axis parallel to the K^+_{inc} momentum, $p_{K^+_{inc}}$, and the y axis parallel to the normal to the production plane,

$$\hat{n}_{prod} \equiv \frac{\vec{p}_{K^+_{inc}} \times \vec{p}_{K^+_{out}}}{\left|\vec{p}_{K^+_{inc}} \times \vec{p}_{K^+_{out}}\right|}$$

as shown in Fig. 1b. The advantage of using this frame is that the sub-magnetic quantum state of the orbital angular momentum ℓ of the system is zero ($m_\ell = 0$). For demonstration purposes we consider both the pseudo-scalar (0^-) exchange--e.g., one-pion exchange--and a vector (1^-) exchange.

(i) <u>A Pseudoscalar Exchange: $K^+_{inc}(0^-) + e(0^-) \rightarrow K^+_{out}(0^-) + \pi^-(0^-)$</u>

The spin parity of the decay products restrict the $K\pi$ system to be in the natural parity series, i.e., 0^+, 1^-, 2^+, ... Due to the choice of quantixation axis one can further conclude that the $K\pi$ system can take $m = 0$ only. Hence the $K\pi$ decay distribution can be expressed in terms of a Legendre polynomial $J(\theta) = \sum_{n=0}^{N} a_n P_n(\cos\theta)$. This gives a naive formalism for virtual $K\pi$ scattering. If there is only s wave then $I(\theta) = a_o$, the $\cos\theta$ distribution is flat. For a pure p wave, e.g., K^*_{890}, $I(\theta) \approx \cos^2\theta$. In this case the spin density matrix element $\rho_{0,0} = 1$ and the rest of the elements vanish. The subscripts 0,0 are the values of the submagnetic quantum number m of the K^*_{890}. For the case when both s and p waves are present, the intensity can be written as $I(\theta) = a_o + a_1 \cos\theta + a_2 \cos^2\theta$. The a_o and a_2 terms are the contributions from the s wave and the p wave respectively. The a_1 term gives the s- and p-wave-interference effect. Similarly a pure pseudoscalar exchange for Δ^{++} production will lead to $m = \pm 1/2$ for the Δ^{++} resonance. Hence any spin density matrix elements $\rho_{mm'}$, with either $m = 3$ or $m' = 3$ will vanish. By conservation of probability ($\mathrm{Tr}\,\rho = 1$) and a parity argument one obtains $\rho_{1,1} = \rho_{-1,-1} = 1/2$.

(ii) A Vector Exchange

We consider the case that the $K\pi$ system has a unique spin 1. In the Gottfried-Jackson frame it can take only $m = \pm 1$. Hence we have $\rho_{11} = \rho_{-1,-1} = 1/2$ and the rest of the elements vanish.

In case both the pseudoscalar and the vector exchange are present for the production of a K^* resonance of $J^P = 1^-$, all the submagnetic quantum states, 0 and ± 1, can be occupied. Hence all the independent spin density matrix elements ρ_{00}, $\rho_{1,1}$ and Re ρ_{10} are nonvanishing.

A. The Triangle Plot for the Final State $K^+\pi^-\pi^+p$

Figure 2 shows the triangle plot, $M(K^+\pi^-)$ vs $M(p\pi^+)$, for the 9-GeV/c data. The mass projections are shown in Fig. 3. In Fig. 3, we observe clear Δ^{++}_{1236} and K^{*0}_{890} bands, which contain about 61% of the events in the $K^+\pi^-\pi^+p$ final state. The Δ^{++}_{1236} band is defined as 1.12-1.32 GeV in $p\pi^+$ mass and the K^{*0}_{890} band 0.84-0.94 GeV in $K^+\pi^-$ mass. Both of these bands are close to the kinematical boundary of the triangle plot. Both resonances are essentially produced peripherally. Based on a kinematical argument, one finds that inside the K^{*0}_{890} band, events with a high $M(p\pi^+)$ value tend to fall into the low $K^{*0}_{890}\pi^+$ mass region which is known as the Q bump.[3] Similarly, inside the Δ^{++}_{1236} band, events with a high $M(K^+\pi^-)$ value form the low $\Delta^{++}_{1236}\pi^-$ mass enhancement.[3] Both of these enhancements are the subjects of recent discussions in the literature.[3] Another interesting point is that both K^{*0}_{890} and K^{*0}_{1420} (1.34-1.50 GeV) are produced together with Δ^{++}_{1236} in the double resonance productions. About 46% of the events in the Δ^{++}_{1236} band are in the $K^*\Delta^{++}$ double resonance regions.

The 4.6-GeV/c data in Figs. 4 and 5 show the same qualitative features as described above.

B. The $K^+\pi^-\Delta^{++}_{1236}$ Channel

1. The Dalitz Plot

The Dalitz plots (Fig. 6) and the corresponding mass projections (Fig. 7) for the 9-GeV/c data show three distinct features, namely, a clear K^{*0}_{890} band, a clear K^{*0}_{1420} band, and a general low $\Delta^{++}\pi^-$ mass enhancement. The enhancement is centered near 1.58 GeV in the $\Delta\pi$ mass and with a width $\Gamma_{\Delta\pi} \approx 0.35$ GeV. This effect not only shows in the high $K\pi$ mass region but also extends down to the $K\pi$ threshold. The small $|t'|$* cut does not help to remove it from the data. The events in the low $\Delta^{++}\pi^-$ mass end are mainly associated with the forward $\cos\theta(K^+\pi^-)$ values, hence the low $\Delta^{++}\pi^-$ mass enhancement production is of a diffractive nature. The angle, $\theta(K^+\pi^-)$, is the Gottfried-Jackson angle for the $K^+\pi^-$ system, i.e., the polar angle in the Gottfried-Jackson frame. The 4.6-GeV/c data (Figs. 8 and 9) show similar features except that the K^*_{1420} resonance and the $\Delta^{++}\pi^-$ enhancement are much less pronounced.

2. The Spin Density Matrix Elements for the Δ^{++}_{1236} as a Function of the $K^+\pi^-$ Mass

Figures 10a,b,c show the spin density matrix elements $\rho_{3,3}$, Re $\rho_{3,1}$, and Re $\rho_{3,-1}$ for the Δ^{++}_{1236} in the Gottfried-Jackson frame as a function of the $K^+\pi^-$ mass for the 9-GeV/c data. The average values over the whole

---

*The variable, t', is defined as $t' = (t - t_m)_{K^+_{inc}\to K^+\pi^-}$, where t_m corresponds to the Chew-Low boundary adjacent to the peripheral physical region.

Δ^{++}_{1236} band are $\rho_{3,3}$ = 0.09±0.01, Re $\rho_{3,1}$ = - 0.05±0.01, and Re $\rho_{3,-1}$ = - 0.02±0.01. The deviation of the data points shown in Fig. 10 are less than two standard deviations from the average values. There is some indication of variations in the spin density matrix elements near the neighborhood of K^*_{890} and K^*_{1420}.

For the data from the 4.6-GeV/c experiment, the spin density matrix elements for the Δ^{++}_{1236} as a function of the $K^+\pi^-$ mass are shown in Figs. 11a,b,c. Their average values are $\rho_{3,3}$ = 0.07±0.02, Re $\rho_{3,1}$ = - 0.03±0.02, and Re $\rho_{3,-1}$ = - 0.00±0.01. They agree with the results from the 9-GeV/c data.

The relation $\rho_{1,1} + \rho_{3,3} = 1/2$ indicates that $\rho_{1,1}$ is considerably larger than $\rho_{3,3}$ at both energies. Spin flip amplitude is less important than spin non-flip amplitudes. Hence the contribution from pion exchange dominates over the contribution from the other possible exchanges, i.e., ρ, A_2, A_1, and B.

Spin density matrix elements as a function of the $K^+\pi^-$ mass are also calculated for small $|t'|$ regions ($|t'| < 0.1$ (GeV/c)^2 for the 9-GeV/c data and $|t'| < 0.3$ (GeV/c)^2 for the 4.6-GeV/c data). The minimum shown in the $M(K^+\pi^-)$ vs $\rho_{3,3}$ plots with no $|t'|$ cuts (Figs. 9a and 10a) is no longer observed. In general the deviations between the data points are reduced to less than 1 or 1-1/2 standard deviations and the values of $\rho_{3,3}$, Re $\rho_{3,1}$, and Re $\rho_{3,-1}$ become very close to zero.

The variation of the spin density matrix elements for the Δ^{++}_{1236} resonance as a function of the $K\pi$ mass is small. This implies that <u>the production of the Δ^{++}_{1236} resonance, at least in the small $|t'|$ region, is rather independent of whether the $K^+\pi^-\Delta^{++}_{1236}$ final is dominated by the $K^{*0}\Delta^{++}_{1236}$ double resonance production or the low $\Delta^{++}_{1236}\pi^-$ mass enhancements.</u>

C. The $K^{*o}_{890}\pi^+ p$ Channel

1. The Dalitz Plot

The Dalitz plot for the $K^{*o}_{890}\pi^+ p$ channel for 9-GeV/c data (Fig. 12) with the corresponding mass projections (Fig. 13) show both the Δ^{++}_{1236} resonance and the Q bump. Note that there are two interesting parallelisms between the $K^+\pi^-\Delta^{++}_{1236}$ and the $K^{*o}_{890}\pi^+ p$ final states: 1) Both y's are produced close to the physical boundaries of the triangle plot, one near each of the two axes. 2) They both show similar structures in the Dalitz plots: strong resonance band(s) parallel to the horizontal axis and a low mass enhancement with a width, ~ 0.35 GeV, along the vertical axis.

The Q bump is a complex phenomenon that has been discussed in earlier publications.[3b] Here we only point out that it has two dominant decay modes, $K^*_{890}\pi^+$ and $\rho^o K^+$, which interfere with each other, and that at both energies it is centered near 1.30 GeV with a width $\Gamma_Q \approx 0.35$ GeV.

Figures 14 and 15 show the $K^{*o}_{890}\pi^+ p$ Dalitz plot and the $p\pi^+$ and $K^{*o}_{890}\pi^+$ mass projections for the 4.6-GeV/c data. They show similar qualitative features as the 9-GeV/c data. Detailed discussions of the Q' bump from the 4.6-GeV/c data were given in an earlier publication.[3b]

2. Spin Density Matrix Elements, $\rho_{mm'}$, for K^*_{890} as a Function of the $p\pi^+$ Mass

Figures 16a,b,c show the spin density matrix elements $\rho_{0,0}$, Re $\rho_{1,0}$, and $\rho_{1,-1}$ for the K^*_{890} resonance as a function of the $p\pi^+$ mass for the 9-GeV/c data. They agree with the average values over the whole K^*_{890} band, i.e., $\rho_{0,0} = 0.68\pm0.02$; Re $\rho_{1,0} = -\ 0.09\pm0.01$; and $\rho_{1,-1} = -\ 0.03\pm0.02$.

Similarly, Fig. 17a,b,c shows the spin density matrix elements of the K^*_{890} resonance as a function of the $p\pi^+$ mass for the 4.6-GeV/c data. The average values are $\rho_{0,0} = 0.70\pm0.04$, Re $\rho_{1,0} = -\ 0.12\pm0.02$, and $\rho_{1,-1} = -\ 0.03\pm0.03$, which agree with results from the 9-GeV/c data. As with the events in the Δ^{++}_{1236} band, these are produced mainly via pion exchange since ρ_{00} is large. The variation of the spin density matrix of K^*_{890} as a function of $p\pi^+$ mass is small. Hence the K^*_{890} events are produced in a way rather independent of the intermediate states, i.e., $K^*_{890}\Delta^{++}_{1236}$ double resonance and Q^+p state where $Q^+ \rightarrow K^*_{890}\pi^+$.

D. The $K^*_{1420}\pi^+p$ Channel

Figure 18 shows the Dalitz plot for the $K^*_{1420}\pi^+p$ channel at 9 GeV/c and Figs. 19a and b show the corresponding mass projections, $M(p\pi^+)$ and $M(K^*_{1420}\pi^+)$. The Dalitz plot has a structure similar to that of the $K^*_{890}\pi^+p$ channel. There is some indication of the low mass enhancement in the $K^*_{1420}\pi^+$ mass centered around 1.720 GeV near the mass where the "L meson" was observed.[5]

For completeness' sake the Dalitz plot for the $K^*_{1420}\pi^+p$ channel at 4.6 GeV/c and the corresponding mass projections are shown in Figs. 20 and 21 respectively.

III. DOUBLE RESONANCE PRODUCTIONS

It is well known that the decay properties of a resonance produced in a production experiment give not only the information about the resonance itself but also the composition of its helicity states in the t channel, which is directly related to the helicity states exchanged (in the t channel).[4] The double resonance productions afford a chance to double-check what has been exchanged in the t channel. Hence to obtain the information about the production mechanisms, double resonance channels become more favorable to analyze. This section includes the analysis of the $K^{*o}_{890}\Delta^{++}_{1236}$ and the $K^{*o}_{1420}\Delta^{++}_{1236}$ channels and some possible higher-mass $I = 3/2$ baryonic resonance productions. Due to the limitation of the statistics of our data, only the $K^{*o}_{890}\Delta^{++}_{1236}$ channel is studied in great detail.

A. The $K^{*o}_{890}\Delta^{++}_{1236}$ Channel

In Sections II.B.2 and II.C.2 we learned that both Δ^{++}_{1236} and K^{*}_{890} are produced predominantly via pion exchange. Assumption of simple one-pion exchange gives $\rho_{00} = 1$ for the K^{*}_{890} and $\rho_{11} = 1/2$ for Δ^{++}_{1236} and that the rest of the spin density matrix elements vanish. The discrepancies between the results from the ideal simple one-pion exchange model and the data can be accounted for by the following effects:

1) Processes other than K^{*}_{890} resonance productions, e.g., a $K\pi$ s wave production and the double peripheral process mentioned earlier (see Fig. 22a).

2) The K^{*}_{890} resonance production via nonpion exchange (see Fig. 22b).

3) Absorption effects.

In the following two subsections we study the $|t'|$ distribution for different $\theta(K^{+}\pi^{-})$ angular regions and the decay properties as a function t'.

1. $|t'|$ Distribution

Figure 23a shows the $|t'|$ distribution for all the events in the K^*_{890} region from the 9-GeV/c data. In order to demonstrate that for K^*_{890} production there are contributing mechanisms other than one-pion exchange, we plot the $|t'|$ distribution with $\cos\theta(K^+\pi^-) < -0.5$ (Fig. 23b), $\cos\theta(K^+\pi^-) \geqq 0.5$ (Fig. 23c), and $-0.5 \leqq \cos\theta(K^+\pi^-) < 0.5$ (Fig. 23d). Different structures in $|t'|$ distribution are observed for the two symmetrical polar regions. In Fig. 23b there is a break in slope near $|t'| = 0.05\ (\mathrm{GeV/c})^2$. The two slopes are $a = 31.2 \pm 12.4\ (\mathrm{GeV/c})^{-2}$ and $a = 7.1 \pm 3.1\ (\mathrm{GeV/c})^{-2}$. In Fig. 23c the data points are well fitted to a straight line with a slope $a = 14.4 \pm 1.8\ (\mathrm{GeV/c})^{-2}$. The slope in Fig. 23c is $a = 10.9 \pm 3.2\ (\mathrm{GeV/c})^{-2}$. For pure single resonance production the $|t'|$ distributions from the events in two symmetrical polar regions should be the same provided that there are <u>only</u> single exchange diagrams such as those shown in Fig. 22b contributing. The different structures of $|t'|$ distributions in Figs. 23b and c indicate that even in the K^*_{890} resonance region, there are non-negligible contributions from other processes, e.g., the double peripheral exchange process shown in Fig. 22a or a $K\pi$ s wave. The change of the slope in Fig. 23b is partly due to the non-pion exchange. More evidence and discussions of these points is given in the study of the decay distributions and the spin density matrix elements for the two resonances. The $|t'|$ distributions for the $K^*_{890}\Delta^{++}_{1236}$ channel from the 4.6-GeV/c data are shown in Fig. 24. Due to the limited statistics, it is not certain whether there is a break shown in the slope for this data. The slope a in each distribution in Fig. 24 is less than that of the corresponding distribution from the 9-GeV/c data.

2. Decay Properties of the K^*_{890}

a. Decay Angular Distribution

Figures 25 and 26 are the cos $\theta(K^+\pi^-)$ vs $\varphi(K^+\pi^-)$ scatter plots and the cos $\theta(K^+\pi^-)$ and the $\varphi(K^+\pi^-)$ projections for events under the $|t'|$ cuts, $|t'| < 0.10$ $(GeV/c)^2$, and $0.10 \leq |t'| < 10.0$ $(GeV/c)^2$. The cutoff, $|t'| < 10.0$ $(GeV)^2$, is applied to eliminate the events produced by the nonperipheral process. The scatter plot for $|t'| < 0.10$ $(GeV/c)^2$ (Fig. 25a) shows that there is a large forward-backward asymmetry in cos $\theta(K^+\pi^-)$ for any Treiman-Yang angle $[\varphi(K^+\pi^-)]$ interval and that events are roughly uniformly populated in $\varphi(K^+\pi^-)$ for a cos $\theta(K^+\pi^-)$ interval. For $|t'| \geq 0.10$ $(GeV/c)^2$, the events are more or less populated at two opposite corners on the scatter plot as shown in Fig. 25b and the Treiman-Yang angular distribution is <u>not flat for any cos $\theta(K^+\pi^-)$ values</u>. These very different patterns are clearly seen in the scatter plots which reveal the features of the correlation effects. Based on the assumption of a unique spin 1, for the events in the K^{*o}_{890} region, by qualitative arguments one finds, from Fig. 25, that in both $|t'|$ regions the average Re ρ_{10} is important and has to take negative values. The contribution to Re ρ_{10} is not due to the interference of the K^*_{890} resonance with a background of the phase space type, since the possible background from the phase space is negligible, especially for the small $|t'|$ region (see Figs. 6 and 8). The causes for the different correlation patterns shown in the scatter plots (Fig. 25a and b) are not well understood at present but what is clear however is that they must be different to give different correlation patterns. In Figs. 26a and c, we observe that the difference between the cos $\theta(K^+\pi^-)$ distributions in the K^*_{890} band with different $|t'|$ cuts is striking. For $|t'| < 0.1$ $(GeV/c)^2$, it is very much like

$\cos^2\theta(K^+\pi^-)$, whereas for $|t'| \geqq 0.1\ (GeV/c)^2$, it is consistent with being flat. The curve in Fig. 26a is the result of a least-squares fit to the Legendre polynomial, $\sum_{\ell=0}^{2} a_\ell P_\ell[\cos\theta(K^+\pi^-)]$. The coefficients of the polynomial fits in the K^{*o}_{890} region are given in Table I.

The $\cos\theta(K^+\pi^-)$ vs $\varphi(K^+\pi^-)$ scatter plots and their projections for the 4.6-GeV/c data are shown in Figs. 27 and 28. They show the same qualitative features as the 9-GeV/c data.

b. Spin Density Matrix ($\rho_{mm'}$) and the Expansion $\sum_{n=0}^{2} a_n \cos^n\theta(K^+\pi^-)$

In analyzing the $K\pi$ system one may take two different points of view. 1) Assume a unique spin 1 for the events in the K^*_{890} region and calculate the spin density matrix elements $\rho_{mm'}$. Then study the composition of the helicity states exchanged in the t-channel. 2) Assume π exchange and consider the incoming K^+ as being scattered by a virtual pion. One then does a partial-wave-type analysis. This point of view is proper when there is more than one $K\pi$ partial wave occurring.

We adopt both points of view in turn and study the spin density matrix ($\rho_{mm'}$) as well as the $\cos\theta(K^+\pi^-)$ power series expansion as a function of $|t'|$.

(1) $\rho_{mm'}$ and $\sigma_1^{\pm}$

Figures 29a,b,c show the ρ_{00}, $\rho_{1,-1}$ and Re ρ_{10} for the K^*_{890} as a function of $|t'|$ for the 9-GeV/c data; ρ_{00} is about 0.8 in the forward direction and drops down to ~ 0.35 for $|t'| > 0.2\ (GeV/c)^2$; $|\rho_{1,-1}|$ is less than 0.1 with a possible change of sign near the very forward direction and at $|t'| \approx 0.2\ (GeV/c)^2$. Re $\rho_{1,0}$ is about -0.2 for all $|t'|$ values, except in the very forward direction where it vanishes. The latter fact reflects the azimuthal symmetry of the $K\pi$ decay about the incoming K^+ beam in the very forward direction. One may puzzle why

ρ_{00} does not decrease much near $|t'| = 0.05\ (\mathrm{GeV}/c)^2$ where there is an essential change in the slope of $|t'|$ distribution. The explanation is that since ρ_{00} is determined purely by the $\cos\theta(K^+\pi^-)$ distribution, even if the $\cos\theta(K^+\pi^-)$ vs $\varphi(K^+\pi^-)$ scatter plots show quite different correlation patterns for the different $|t'|$ regions the $\cos\theta(K^+\pi^-)$ projections may still resemble each other.

Figure 30 shows $\sigma_1^{\pm} \equiv \frac{1}{2}(\rho_{1,1} \pm \rho_{1,-1})$ (see Ref. 5) as a function of $|t'|$. $\sigma_1^{\pm}$ corresponds to the contributions from the natural and the unnatural parity series to the helicity state 1 exchanged in the t channel. Figure 30 indicates that both contributions increase as $|t'|$ increases. They are of the same order for $|t'| \geqq 0.2\ (\mathrm{GeV}/c)^2$. In the forward direction they do not quite vanish. Due to the limitation of the statistics of our data, we cannot evaluate $\sigma_1^{\pm}$ with finer $|t'|$ intervals, therefore we cannot test whether they really vanish in the very forward direction or not. Figures 31 and 32 show the spin density matrix elements and $2\sigma_1^{\pm}$ as a function of $|t'|$ for the K^*_{890} from the reaction $K^+p \rightarrow K^{*0}_{890}\Delta^{++}_{1236}$ at 4.6 GeV/c. In general they agree with the results from the 9-GeV/c data except for the following exceptions: 1) as a function of $|t'|$, the ρ_{00} from the 4.6-GeV/c data (Fig. 31a) drops slower than that from the 9-GeV/c data (Fig. 29a); 2) the $\sigma_1^{\pm}$ for the 4.6-GeV/c data (Fig. 32) are relatively smaller than the $\sigma_1^{\pm}$ for the 9-GeV/c data.

<u>The above discussion indicates that the contribution of one-pion exchange extends farther out in t and that the vector and the pseudovector exchange are less important at lower energy.</u>

(2) <u>$\sum a_n \cos^n\theta(K^+\pi^-)$ Expansion</u>

Figure 33 shows the results from the fits of a second-order polynomial in $\cos\theta(K^+\pi^-)$, $\sum_{n=0}^{2} a_n \cos^n\theta(K^+\pi^-)$, to the 9-GeV/c data, excluding the very forward polar region [$\cos\theta(K^+\pi^-) > 0.5$]. This cut eliminates most of the contribution from the double peripheral processes. The fit is normalized to the number of events in each $|t'|$ interval. If we assume pure pseudoscalar exchange, then a_2 and a_o indicate the contributions from the $K\pi$ p- and s-wave intensities respectively and a_1 the interference between the p wave and the s wave. However, if in addition there is a vector exchange, then its $\sin^2\theta(K^+\pi^-)$ decay distribution added to the $\cos^2\theta(K^+\pi^-)$ decay distribution from the pseudoscalar exchange can fake an a_o term. We observe a_o drops more slowly than a_1 or a_2. a_o/a_2 is approximately equal to 1/8 for $|t'| < 0.05$ (GeV/c)^2, which gives the ratio of the contributions from the possible s wave to the p wave. For $|t'| \geq 0.15$ (GeV/c)^2, (a_o/a_2) and (a_o/a_1) gradually increase and presumably the non-pion exchanges become more important in this region. This indicates that in analyzing $K\pi$ scattering the sample must be restricted to very small $|t'|$ values, say less tha 0.05 (GeV/c)^2 at 9 GeV/c.

The coefficients a_o, a_1, and a_2 for the 4.6-GeV/c data have been calculated both with $\cos\theta(K^+\pi^-) < 0.5$ and no $\cos\theta(K^+\pi^-)$ cut. The two sets of coefficients agree within statistics. Figure 34 shows the coefficients for the 4.6-GeV/c data with no cut in $\cos\theta(K^+\pi^-)$. The coefficient a_2 drops twice as fast as that of the 9-GeV/c data from $|t'| = 0$ to $|t'| \approx 0.1$ (GeV/c)^2. The ratios a_o/a_2 and a_1/a_2 from the 4.6-GeV/c data are larger than those from the 9-GeV/c data by a factor of 6 and 2 respectively. The comparison indicates that in the small momentum transfer region, $|t'| < 0.1$ (GeV/c)^2, the 4.6-GeV/c data may have a larger $K\pi$ s-wave contribution (relative to the p wave) than the 9-GeV/c data.

In conclusion, from the values of the spin density matrix, $\rho_{mm'}$, and the coefficients in the expansion $\sum_{n=0}^{2} a_n \cos^n\theta_{K\pi}$, we obtain the well-known spin-parity assignment $J^P = 1^-$ for K^*_{890}. The production mechanism is dominated by pion exchange for small $|t'|$ values, say $|t'| < 0.05\ (\text{GeV}/c)^2$ for the 9-GeV/c data and $|t'| \lesssim 0.3\ (\text{GeV}/c)^2$ for the 4.6-GeV/c data. The non-pion exchange contributions become gradually more important for $|t'|$ above those values.

3. Decay Properties of Δ^{++}_{1236}

Figures 35 and 36 show the spin density matrix elements of Δ^{++}_{1236} from the 9- and 4.6-GeV/c data, respectively. In both sets of data we observe the following: 1) The $\rho_{3,3}$ is small and increases as $|t'|$ increases. 2) The Re $\rho_{3,1}$ is not negligible except possibly in the very forward direction, and it decreases as $|t'|$ increases. 3) The Re $\rho_{3,-1}$ is not important and essentially agrees with being zero. From these observations we conclude that spin nonflip amplitude dominates for small $|t'|$ values and that the spin flip amplitudes become gradually important for $|t'| > 0.05\ (\text{GeV}/c)^2$ in the 9-GeV/c data and $|t'| > 0.3\ (\text{GeV}/c)^2$ in the 4.6-GeV/c data. This agrees with our conclusions based on the decay properties of the $K\pi$ system discussed in Section III.A.1.

B. The $K^*_{1420}\Delta^{++}_{1236}$ Channel

1. $|t'|$ Distribution

Figures 37a and b show the $|t'|$ distributions for the 9- and 4.6-GeV/c data, respectively. The slopes are $a = 10.3\ (\text{GeV}/c)^{-2}$ for the 9-GeV/c data (Fig. 36a) and $a = 6.5\ (\text{GeV}/c)^{-2}$ for the 4.6-GeV/c data (Fig. 36b). No break in slope is observed in the $|t'|$ distributions even when we restrict our sample to the criterion $\cos\theta(K^+\pi^-) \leq 0.5$. This could be due to 1) the Chew-Low boundary, and hence the physical region at K^*_{1420} is relatively far away from the pion pole as compared with that in lower $K\pi$ mass; 2) low statistics. The fact that the slope at 9 GeV/c appears to be steeper than that at 4.6 GeV/c could also be due to the kinematic effect that the Chew-Low boundary is flatter at higher energy.

2. Decay Angular Distributions and the Legendre Polynomial Expansion For the K^{*o}_{1420}

Figures 38 and 39 show the cos $\theta(K^+\pi^-)$ vs $\varphi(K^+\pi^-)$ scatter plots for the events in the $K^{*o}_{1420}\Delta^{++}_{1236}$ channel at 9 and 4.6 GeV/c respectively. They reveal the same qualitative features as the cos $\theta(K^+\pi^-)$ vs $\varphi(K^+\pi^-)$ scatter plots for the $K^{*o}_{890}\Delta^{++}_{1236}$ events shown in Figs. 25 and 27.

Figures 40 and 41 show the cos $\theta(K^+\pi^-)$ and $\varphi(K^+\pi^-)$ projections of Figs. 38 and 39 respectively. A $|t'|$ cut, $|t'| < 0.1$ (GeV/c)^2, is imposed on Figs. 40a and b to eliminate part of the contribution from the non-pion exchange. The curve shown in Fig. 40a is a fourth-order Legendre polynomial $\{\sum_{\ell=0}^{4} a_\ell P_\ell[\cos\theta(K^+\pi^-)]\}$ fit to the data. The coefficients a_ℓ are given in Table I. The Treiman-Yang angular distribution shown in Fig. 40b is more or less isotropic. Figures 40c and d show the cos $\theta(K^+\pi^-)$ and the $\varphi(K^+\pi^-)$ distribution for the events with $|t'| > 0.1$ (GeV/c)^2. The cos $\theta(K^+\pi^-)$ distribution in the large $|t'|$ region (Fig. 40c) is much flatter than that in the small $|t'|$ region (Fig. 40a). The Treiman-Yang angular distribution in the large $|t'|$ region (Fig. 40d) is no longer flat.

The decay angular distributions for the 4.6-GeV/c data (Fig. 41) show the same qualitative features as those for the 9-GeV/c data. Due to the statistical limitations of the 4.6-GeV/c data we fit the cos $\theta(K^+\pi^-)$ distribution for all the $K^{*o}_{1420}\Delta^{++}_{1236}$ events to the Legendre polynomial

$[\sum_{\ell=0}^{4} a_\ell P_\ell(\cos\theta(K^+\pi^-))]$. The result is shown in Fig. 42. The coefficients a are given in Table I.

3. Spin Density Matrix Elements of Δ^{++}_{1236}

Figures 43 and 44 show the spin density matrix elements of Δ^{++}_{1236} as a function of $|t'|$. They indicate the same structure as the corresponding spin density matrix elements for the Δ^{++} produced together with the K^{*0}_{890} at 9 and 4.6 GeV/c (Figs. 35 and 36).

C. Higher Δ^{++}'s

The Δ^{++}_{1920} was observed in the $K^+p \to K^+\pi^-\pi^+p$ at 12.7 GeV/c (Ref. 7) by selecting events in the backward $\theta(p\pi^+)$ region, where $\theta(p\pi^+)$ is the Jackson angle in $p\pi^+$ rest frame. Figures 45 and 46 show the scatter plots, $M(p\pi^+)$ vs $\cos\theta(p\pi^+)$ for the events in the K^*_{890} and the K^*_{1420} regions from the 9- and 4.6-GeV/c data. In Figs. 41a and 42a there is some indication of higher population of events around 1600 to 2000 MeV in $p\pi^+$ mass. This could be due to effect of five higher Δ resonances, namely Δ_{1650}, Δ_{1670}, Δ_{1890}, Δ_{1910}, and Δ_{1950}.[2a] The widths of these resonances are of the order of 100 to 300 MeV. Based on Figs. 45b and 46b there is no evidence for high Δ's produced together with the K^*_{1420}.

IV. THE $K\pi$ SYSTEM IN THE $K^+\pi^-\Delta^{++}_{1236}$ CHANNEL

A. $K\pi$ Asymmetry

Under the assumption of one-pion exchange, the asymmetry, $A \equiv (F-B)/(F+B)$, for the $K\pi$ system reflects the interference effect of different $K\pi$ partial waves in a simple way. F and B refer to the forward and the backward events in $\theta(K^+\pi^-)$. If there is only one partial wave or many partial waves of the same parity, the asymmetry is zero. With two partial waves of opposite parities the asymmetry is proportional to $\sin\delta_1 \sin\delta_2 \cos(\delta_1 - \delta_2)$, where δ_1 and δ_2 are the decay phase angles for the two partial waves. For two nearby resonances δ_1-δ_2 may cross 90 deg twice, hence two zeroes appear in the $M(K^+\pi^-)$ vs A plot. The distance between the two zeroes measures the spacing of the two resonances. However, one should keep in mind that this simple picture could be obscured by the presence of many $K\pi$ partial waves or by the production mechanisms other than pion exchange.

Figure 47 shows a plot for forward-backward asymmetry for the $K\pi$ system as a function of $K\pi$ mass from the 9-GeV/c data. We observe that just below the K^*_{890} the asymmetry goes to zero very rapidly from a positive value and then increases rather smoothly to positive values again for higher $K\pi$ masses except for a small perturbation on passing the K^*_{1420}. The large positive asymmetry for $M(K^+\pi^-) \geqq 1.54$ GeV indicates that the K^+ goes forward and the π^- backward in the $K\pi$ rest frame. Here the backward π^- is associated with the low $\Delta^{++}\pi^-$ mass enhancement. The rapid change in asymmetry just below the K^*_{890} can be attributed to the interference of the K^*_{890} with 1) some $K\pi$ partial waves of parity opposite to that of the K^*_{890} ($J^P = 1^-$) or 2) the process that leads to the $\Delta^{++}\pi^-$ mass enhancement as discussed in Appendix I, or both. Trippe et al.,[8] in an analysis of the same four-body reaction at 7.3 GeV/c, deduced an s-wave $K\pi$ resonance at a mass of ~ 1.1 GeV and with a width of ~ 0.4 GeV on the basis of an application of the Duerr-Pilkuhn method to an OPE model. Also Antich et al.[9] have claimed the existence of a $J^P = 1^-$ wave in the neighborhood of the K^*_{1420} which interferes with the dominant $J^P = 2^+$ wave to give the observed asymmetry in this region. In addition, several K-nucleon experiments leading to three particles in the final state have shown indications of the $K\pi$ mass peaks in this region.[10] These indications were for narrow ($\Gamma \approx 0.1$ GeV) peaks at $M(K^+\pi^-) = 1.26\pm0.02$ GeV in the reaction $K^+p \rightarrow K^o\pi^+p$ at 3.9 GeV/c, at $M(K^+\pi^-) = 1.16\pm0.01$ GeV in the reaction $K^-n \rightarrow \overline{K^o}\pi^-n$ at 3.9 GeV/c, and at ≈ 1.08 GeV in $K^+p \rightarrow K^o\pi^+p$ at 3.5 and 3.9 GeV/c. These mass peaks may exist in the $K^+\pi^-\Delta^{++}$ channel and obscure the simple interpretation of the asymmetry.

We have also studied the asymmetry as a function of t', and within the limited statistics we observe: 1) at small $|t'|$ values the variation in asymmetry at the K^*_{1420} resembles that at the K^*_{890}, and 2) at large $|t'|$ values both these rapid variations in asymmetry are reduced.

Discussion of the $M(K^+\pi^-)$ vs asymmetry plot for the 4.6-GeV/c data was given in an earlier report.[3e] It shows the same qualitative features as that from the 9-GeV/c data (Fig. 47) except that the 9-GeV/c data have better statistics and wider range in $K\pi$ mass spectrum.

B. $|t'|$ Distributions

Figure 48a shows the $|t'|$ distribution for the events with $M(K\pi) <$ 1.54 GeV. The data are not consistent with one or even two exponential dependences. In order to investigate the production mechanism of the $K\pi$ system we study the structure of the $|t'|$ distribution as a function of cos $\theta(K\pi)$ as we did for the K^*_{890} events. Figure 48b shows the $|t'|$ distribution for the events with $M(K^+\pi^-) < 1.54$ GeV and $\cos\theta(K^+\pi^-) < 0.5$. The straight lines represent the results of a least-squares fit to the data for two functions of the form $e^{at'}$. We observe a very steep forward peak with slope $a = 23.6\pm5.2$ $(\mathrm{GeV}/c)^{-2}$ for $|t'| < 0.05$ $(\mathrm{GeV}/c)^2$, and a flatter distribution with slope $a = 9.5\pm2.0$ $(\mathrm{GeV}/c)^{-2}$ for $|t'| \geq 0.05$ $(\mathrm{GeV}/c)^2$. In contrast to this structure, the t' distribution for the events in the forward cos θ region (Fig. 48c) appears quite different. The data in Fig. 48c are fitted well by a single slope, $a = 13.5\pm1.2$ $(\mathrm{GeV}/c)^{-2}$ for $|t'| < 0.3$ $(\mathrm{GeV}/c)^2$. We shall associate this sharp forward peak with pion exchange. The lesser slope is due to the participation of non-pion exchanges (e.g., A_1, B, ρ, and A_2). Evidence for this assignment will be presented in the next few sections.

Figure 48d shows the $|t'|$ distribution for the events with $M(K^+\pi^-) \geq 1.54$ GeV. The relative flatness of the slope, $a = 4.4\pm0.5$ $(\mathrm{GeV}/c)^2$, can be qualitatively understood in two ways. One is that the high $K\pi$ mass region is relatively far away from the pion pole. The other is due to the factor $(s/s_o)^{\alpha_\pi(t)}$ in the Regge amplitude. Here $\alpha_\pi(t)$ is the exchanged pion trajectory and t is the square of the four-momentum transfer from the target proton to the outgoing Δ^{++}. For the low $K\pi$ mass region where a single exchange diagram (Fig. 22b) dominates, s = (total energy)^2 is about $(4.25)^2$ $(\mathrm{GeV})^2$. For the high $K\pi$ mass regions where the double exchange diagram (Fig. 22a) dominates, $s = s(\Delta^{++}\pi^-)$ which is about $(1.58)^2$ $(\mathrm{GeV})^2$. Therefore, due to the s-dependence factor the slope in the $|t|$ distribution for events with $M(K^+\pi^-) \geq 1.54$ GeV should be smaller than that for the events with $M(K^+\pi^-) < 1.54$ GeV by a factor $\approx 2\alpha'_\pi\ \mathrm{In}(4.25/1.58)^2 \approx 4$. Here we have used the linear form for the trajectory $\alpha_\pi = \alpha'_\pi(t - m_\pi^2)$, and have set $\alpha'_\pi = 1\ (\text{GeV/c})^{-2}$. The slopes in the $|t'|$ distributions should differ by a factor of the same order. Figure 48e is an enlargement of the small $|t'|$ region of Fig. 48b. The same phenomena were observed when we restricted the sample to events in the K^{*o}_{890} band in Section III.A, which represents about 33% of the events with $M(K^+\pi^-) <$ 1.54 GeV. This supports the assumption that the production mechanisms for the events with $M(K^+\pi^-) < 1.54$ GeV/c are the same as those for the events in the $K^{*o}_{890}\Delta^{++}$ double resonance region. Figures 49a,b,c show the $|t'|$ distribution from the 4.6-GeV/c data with no $\cos\theta(K^+\pi^-)$ cut, $\cos\theta(K^+\pi^-) < 0.5$, and $\cos\theta(K^+\pi^-) > 0.5$ respectively. There is no indication of a break in slope in the $|t'|$ distributions in Fig. 49b. This can be due to two reasons: 1) The one-pion exchange dominates in a wider t range and the non-pion exchanges are less important in the data at 4.6 GeV/c than the data at 9 GeV/c. (See the conclusion Section III.A.2b(1).) 2) To see a fine effect such as a break in slope one needs data with good statistics. The 4.6-GeV/c data do not have sufficiently good statistics. For $\cos\theta(K^+\pi^-) \geqq 0.5$, the $|t'|$ distribution (Fig. 49c) cannot be fitted to the form $e^{at'}$.

C. Decay Distributions

1. $M(K^+\pi^-)$ vs $\cos\theta(K^+\pi^-)$ and $M(K^+\pi^-)$ vs $\varphi(K^+\pi^-)$

Figures 50a and 50b show the $M(K^+\pi^-)$ vs $\cos\theta(K^+\pi^-)$ scatter plots for $|t'| < 0.1\ (\text{GeV/c})^2$ and $|t\ | \geqq 0.1\ (\text{GeV/c})^2$ respectively. We observe the following.

1) For $M(K^+\pi^-) > 1.54$ GeV, events tend to concentrate in the very forward $\theta(K^+\pi^-)$ region for small $|t'|$ values.

2) In both $|t'|$ regions, the K^*_{1420} is not well separated in the forward $\theta(K^+\pi^-)$ region from the events that produce the low $\Delta^{++}\pi^-$ mass enhancement.

3) The K^{*o}_{890} band shows distinctly in both $|t'|$ regions. For $|t'| < 0.1$ $(GeV/c)^2$ it is cosine-square-like but with an asymmetry in favor of the forward $\theta(K^+\pi^-)$; for $|t'| \geqq 0.1$ $(GeV/c)^2$ it agrees with being uniform in $\cos\theta(K^+\pi^-)$.

4) Between the two well-known K^*'s, there is no distinct feature in the forward $\theta(K^+\pi^-)$ region. But for $\cos\theta(K^+\pi^-) < 0$, there is some population of events separated from both K^*'s centered near 1.1 GeV with a width of ~ 0.1 GeV in Fig. 50b.

5) In the small t' region (Fig. 50a), there is a clear indication that the mean value of the K^*_{890} mass shifts from a lower value in the forward region to a higher value in the backward region in $\theta(K^+\pi^-)$.

Figures 51a and b show $M(K^+\pi^-)$ vs $\varphi(K^+\pi^-)$ plots for $|t'| < 0.1$ $(GeV/c)^2$ and for $|t'| \geqq 0.1$ $(GeV/c)^2$ respectively. An asymmetry in favor of zero degree in $\varphi(K^+\pi^-)$ shows for all values of the $K\pi$ mass in both plots. This asymmetry becomes more pronounced as $M(K^+\pi^-)$ increases, but decreases as $|t'|$ is reduced. Since the high $K\pi$ mass region is mainly associated with the low $\Delta^{++}\pi^-$ mass enhancement (discussed in Appendix I), hence the double peripheral processes yielding the latter can be an important source of the asymmetry even in the K^*'s production region. The absorption effect and the Regge cuts may also contribute to the asymmetry, but it is very difficult to state quantitatively how much each contributes.

Figures 52 and 53 show $M(K^+\pi^-)$ vs $\cos\theta(K^+\pi^-)$ and $M(K^+\pi^-)$ vs $\varphi(K^+\pi^-)$ plots for the 4.6-GeV/c data. Comparing these plots with the corresponding plots at 9 GeV/c we observe the following.

1) Events from the 4.6-GeV/c data are not so much in favor of the forward $\theta(K^+\pi^-)$ values and zero degree in $\varphi(K^+\pi^-)$ as those from the 9-GeV/c data. This fact implies that the diffractive-type process that produces the

low $\Delta^{++}\pi^-$ mass enhancement is not so prominent at lower energy as at higher energy.

2) There is no clear indication of any mass enhancements in between the well-known K^*'s shown in the 4.6-GeV/c data.

3) The same kind of K^*_{890} mass shift observed in the 9-GeV/c data (Fig. 50a) also shows in the small $|t'|$ region at 4.6 GeV/c as shown in Fig. 52a.

2. $\langle Y_L^M \rangle$ Moments

In order to study the contribution from different angular momentum states, we calculate the $\langle Y_L^M \rangle$ moments in the $K^+\pi^-$ mass intervals along the Δ^{++}_{1236} band in the triangle plots as shown in Figs. 2 and 4. $\langle Y_L^M \rangle$ is defined by

$$\langle Y_L^M \rangle_J = \frac{1}{N_J} \sum_{i=1}^{N_J} Y_L^M(\theta_i, \varphi_i) \quad ,$$

where N_J is the total number of events in the $\underline{J}$th $K^+\pi^-$ mass interval and θ_i, φ_i are the values of θ and φ for the $\underline{i}$th event in that mass interval. θ and φ are defined in the Gottfried-Jackson frame of the $K^+\pi^-$ system.

Figures 54 and 55 show the moments $\langle Y_L^M \rangle$ as a function of $K^+\pi^-$ mass for the 9- and 4.6-GeV/c data, where $L \leqq 6$ and $M = 0,1$. In order to eliminate a large part of the contribution from the non-pion exchange we make a $|t'|$ cut for the 9-GeV/c data, namely $|t'| < 0.1$ (GeV/c)^2. Due to the low statistics level of the 4.6-GeV/c data and the fact that the non-pion exchange is not important at this energy, we extend the $|t'|$ cut to $|t'| < 0.3$ (GeV/c)^2. The following observations are made:

1) Below K^*_{1420}, the higher partial waves ($\ell > 2$) are not important as compared with s and p waves.

2) There is a dominant p-wave effect near K^*_{890} shown in Figs. 54b and 55b and some indication of a d-wave effect near K^*_{1420} shown in Figs. 54d and 55d.

3) In Figs. 54a and 55a, there is an enhancement of $\langle Y_1^0 \rangle$ near K^*_{890}. This indicates the interference effect of the s and the p waves.

D. Mass Shift of K^{*0}_{890}

Figure 56 shows the $K^+\pi^-$ mass distributions for the 9-GeV/c data in different cos $\theta(K^+\pi^-)$ regions with $|t'| < 0.1$ $(GeV/c)^2$. These mass distributions show quite different shapes and mean locations for the events in the K^{*0}_{890} region. In the very forward $\theta(K^+\pi^-)$ region, cos $\theta(K^+\pi^-) >$ 0.85 (Fig. 56a), the signal-to-background ratio is small and hard to define. For $0 \leq \cos\theta(K^+\pi^-) < 0.85$ (Fig. 56b), the K^{*0}_{890} signal is very sharp and the background is very small. The mean value of the signal is close to 890 MeV. In the backward $\theta(K^+\pi^-)$ region (Fig. 56c), the signal-to-background ratio is small again. The mean value of the bump in the K^*_{890} region appears to be at least 15 or 20 MeV above 890 MeV in the $K^+\pi^-$ mass.

Figure 57 shows the $K^+\pi^-$ mass distributions for the 4.6-GeV/c data with $|t'| < 0.07$ $(GeV/c)^2$ and the same cos $\theta(K^+\pi^-)$ cuts as those shown in Fig. 56. They show the same qualitative features as the 9-GeV/c data.

Figure 58 shows the combined distributions of Figs. 56 and 57. With higher statistics in Fig. 58, all the features mentioned in the first paragraph become more pronounced. The implications of the changes indicated in three different angular regions are complicated.

1) The mean value of the mass peak in the backward region shifts a non-negligible amount above the nominal value of the K^*_{890} mass.[11] Since the double peripheral processes leading to the $\Delta^{++}\pi^-$ enhancement produce events predominantly in the forward θ region, except possibly near $K\pi$ threshold,

this upward mass shift in the backward region should be due to the interference between a p-wave K^*_{890} and some process(es) other than the mentioned double peripheral processes. In terms of $K\pi$ partial waves, one can estimate the highest order of the partial waves from $\langle Y_L^M \rangle$ moments. From the discussion given in the last section, we learned that in the $K\pi$ mass region below K^*_{1420}, the partial waves with $\ell \geqq 1$ is not important as compared with p wave and s wave. Therefore the mass shift should be mainly due to the interference of an s wave with the dominant p-wave K^*_{890}. Since $K\pi$ s wave can couple to π only and one-pion exchange dominates the small $|t'|$ region, one should expect that the mass shift and the apparent width of the K^*_{890} changes as a function of $|t'|$.

2) There is a large excess of events in the forward $\theta(K^+\pi^-)$ region ($\theta > 0$). The effect of the low $\Delta^{++}\pi^-$ mass enhancement, which is also in favor of small $|t'|$ values, is unseparable from the contribution of K^*_{890} production in the forward θ region. This may be part of the reason why there is considerable excess of events there (Figs. 78a and b).

At this stage, the first problem we should solve is to find a clean reaction to determine accurately the mass and the width of the K^*_{890}.[12] Secondly, we need to understand the effect of the double peripheral process(es) (as shown in Fig. 22a) on the small $K^+\pi^-$ mass region. Then finally we can do a partial-wave analysis for the $K\pi$ system in an inelastic reaction like $K^+p \rightarrow K^+\pi^-\Delta^{++}$.

E. <u>$K\pi$ Mass Spectra</u>

Figure 59a shows the $K^+\pi^-$ mass distribution for all our events in the $K^+\pi^-\Delta^{++}$ channel at 9 GeV/c; Fig. 59b with $|t'| < 0.1$ (GeV/c)^2, and Fig. 59c with $|t'| \geqq 0.1$ (GeV/c)^2. The shaded histograms have the cut $\cos\theta(K^+\pi^-) < 0.5$, in order to reduce the contribution from the low-mass

$\Delta^{++}\pi^{-}$ enhancement. We make the following observations.

1) In both the unshaded and the shaded histograms in Fig. 59b $[|t'| < 0.1$ $(GeV/c)^2]$ the background between the two well-known K^*'s is very large in comparison with that part of the mass spectrum above the K^*_{1420}. Since an s-wave $K\pi$ system can couple only to pion exchange and the region $|t'| < 0.1$ $(GeV/c)^2$ is dominated by pion exchange, it may be reasonable to associate at least part of this plateau with an s-wave $K\pi$ system. Whether the various mass peaks reported in the $K\pi N$ channel[10] have any relevance to this high plateau is not very clear at present.

2) In the unshaded histogram in Fig. 59 $[|t'| \geq 0.1$ $(GeV/c)^2]$ the background between the two K^*'s appears to join smoothly with the mass spectrum in the high $K\pi$ mass region. In addition, a small mass peak is seen at a mass of about 1.1 GeV, where a change in the decay angular distribution is also observed, as mentioned in the preceding section. This mass peak at 1.1 GeV shows more prominently in the shaded histogram in Fig. 59c, where the effects of the low-mass $\Delta^{++}\pi^{-}$ enhancement have been reduced. This could be the same enhancement as those in the 1080 to 1160-MeV region mentioned in Ref. 10a,c, but present statistics do not permit a definitive statement. Since this enhancement appears only for $|t'| \geq 0.10$ $(GeV/c)^2$, it is presumably produced by a non-pion-exchange mechanism. The shaded histogram in Fig. 59b shows a greater number of events in the plateau than in the region above the K^*_{1420}, but the effect is somewhat reduced in Fig. 59c. Since the plateau in Fig. 59c, where pion exchange is very suppressed, cannot be due to s wave, and there is an indication of a narrow mass peak at 1.1 GeV here, possible higher spin $(J \geq 1)$ resonances in this region may be the explanation. To improve the statistics we extend the $|t'|$ cut down to $|t'| = 0.05$ $(GeV/c)^2$ where a break in the

slope of the $|t'|$ distribution occurs. Figure 60 shows the $M(K^+\pi^-)$ distribution with $|t'| \geq 0.05$ (GeV/c)^2 and $\cos\theta(K^+\pi^-) < 0$. Note that the signal at 1.1 GeV is considerably enhanced. By an eyeball estimation the signal-to-background ratio is about 1:1 and the signal itself is roughly a four-standard-deviation effect relative to the background.

3) All the discussions given above agree with the assignment of the forward t' peak as due to pion exchange, and the region with lesser slope as due to the participation of non-pion exchanges. We note that Trippe et al.[8] in their OPE analysis of this $K\pi$ mass region have used data with $|t|$ as large as 0.5 (GeV/c)^2 at 7.3 GeV/c, which, on the basis of the present work, must contain considerable contributions from non-pion-exchange mechanisms that cannot lead to s-wave $K\pi$ scattering.

The $K^+\pi^-$ mass spectra for the 4.6-GeV/c data under different $|t'|$ cuts are shown in Fig. 61. The mass spectrum in the small $|t'|$ region (Fig. 58b) qualitatively agrees with Fig. 56b. However, there is no statistically significant mass enhancement near 1100 MeV observed in the high $|t'|$ region (Fig. 61c). This seems not surprising because the non-pion-exchange is not very important even at $|t'| \approx 0.6$ (GeV/c)^2 [$\rho_{00} \approx 0.5$ at $|t'| \approx 0.6$ (GeV/c)^2 for the K^*_{890} as shown in Fig. 31a].

F. Conclusions

We conclude:

1. Pion exchange appears to dominate the reaction $K^+p \rightarrow K^+\pi^-\Delta^{++}$ at 9 GeV/c for $|t'| < 0.1$ (GeV/c)^2, but non-pion exchanges become important for $|t'| \geq 0.1$ (GeV/c)^2. This has been demonstrated in studies of the t' distributions, the decay angular distributions of the $K\pi$ system, and the spin-density matrix elements. For the 4.6-GeV/c data, one-pion exchange dominates over a relatively larger $|t'|$ region [$|t'| \lesssim 0.3$ or 0.4 (GeV/c)^2].

2. The well-known asymmetry in the $K\pi$ decay angular distribution is due to the interference of the dominant resonant waves for the K^*_{890} and K^*_{1420} with background terms. We note that the observed asymmetries in the K^*_{890} and K^*_{1420} region require an even-parity background term near the K^*_{890} and an odd-parity background term under the K^*_{1420} (p wave?). Although we cannot ascertain quantitatively the contribution from the background terms such as 1) an important partial wave of opposite parity, to the dominant K^* resonance, 2) the low-mass $\Delta^{++}\pi^-$ enhancement, and 3) any other possible source of background, we emphasize the importance of accounting for the various origins of this asymmetry in any analysis of $K\pi$ scattering.

3. A fact which is closely related to the asymmetry is that we observe a mass shift between the K^*_{890} events in the forward region ($\cos\theta \geqq 0$) and those in the background region ($\cos\theta < 0$). This together with the $\langle Y_L^M \rangle$ moments for the $K\pi$ system indicates a strong $K\pi$ s wave near K^*_{890}. The effect of $\Delta^{++}\pi^-$ is difficult to estimate. Due to these interference effects with K^*_{890}, the determination of the mass and width for K^*_{890} becomes nontrivial. A reasonable place to study the properties of K^*_{890} would be reactions like $K^+p \to K^o\pi^+p$ and $K^-n \to \overline{K^o}\pi^-n$ where the K^*_{890} production is dominated by vector exchange except in the very forward direction and the diffractive-type process like $\Delta^{++}\pi^-$ enhancement in the $K^+\pi^-\Delta^{++}$ is suppressed.

Table I. Coefficients of $\sum_{\ell=0} a_\ell P_\ell(\cos\theta)$ for the K^*_{890} and K^*_{1420}.

(a) The $K^*_{890}\Delta^{++}_{1236}$ channel at 9 GeV/c with $|t'| < 0.1$ (GeV/c)^2

a_0	a_1	a_2	a_3	a_4
1.0	0.73±0.06	1.33±0.06		
1.0	0.70±0.07	1.31±0.06	-0.09±0.09	
1.0	0.69±0.07	1.34±0.08	-0.08±0.10	0.06±0.11

(b) The $K^*_{890}\Delta^{++}_{1236}$ channel at 4.6 GeV/c with $|t'| < 0.07$ (GeV/c)^2

a_0	a_1	a_2	a_3	a_4
1.0	0.65±0.12	1.53±0.10		
1.0	0.64±0.14	1.53±0.10	-0.01±0.17	
1.0	0.64±0.14	1.57±0.14	0.01±0.18	0.10±0.19

(c) The $K^*_{1420}\Delta^{++}_{1236}$ channel at 9 GeV/c with $|t'| < 0.1$ (GeV/c)^2

a_0	a_1	a_2	a_3	a_4	a_5	a_6
1.0	0.63±0.09	1.90±0.09	0.20±0.11	1.23±0.13		
1.0	0.68±0.10	2.06±0.08	0.18±0.14	1.35±0.12	0.41±0.13	
1.0	0.67±0.10	2.14±0.10	0.21±0.16	1.68±0.16	0.20±0.14	0.59±0.15

(d) The $K^*_{1420}\Delta^{++}_{1236}$ channel at 4.6 GeV/c with no $|t'|$ cut

a_0	a_1	a_2	a_3	a_4	a_5	a_6
1.0	0.14±0.15	1.01±0.19	0.01±0.22	0.66±0.23		
1.0	0.16±0.15	1.02±0.19	0.07±0.23	0.67±0.23	0.25±0.28	
1.0	0.16±0.16	1.08±0.19	0.12±0.23	0.66±0.26	0.29±0.28	-0.18±0.32

ACKNOWLEDGMENTS

I would like to express my sincere appreciation and gratitude to Professor Gerson Goldhaber for his guidance, encouragement and interest during the years I have studied under him.

I am deeply indebted to the late Dr. Sulamith Goldhaber for her teaching and encouragement at the beginning of my research career in high energy physics.

I would like to thank Professor George H. Trilling for his advice and interest and for many useful discussions with him.

I wish to thank Dr. Benjamin C. Shen whom I worked with on the experiment K^+p at 4.6 GeV/c. Thanks are also due Professor Gideon Alexander and Dr. Alexander Firestone who shared the analysis of part of the experiment K^+p at 9 GeV/c.

I have been enlightened by the comments from Professor J. D. Jackson through several discussions with him.

I would like to thank Professor L. M. Stevenson for his comments on my thesis.

I would like to thank Dr. Edmond L. Berger and Dr. Peter D. Ting for interesting discussions.

I wish to thank Dr. R. Shutt and staff of the 80-inch bubble chamber and Dr. H. Foelsche and the AGS crew for helping with our runs at Brookhaven.

I would like to thank Jimmy N. MacNaughton who has worked with me on the analysis of part of the 4.6-GeV/c data and has helped me to understand the complicated bookkeeping system.

I wish to thank Dr. Sharon Hagopian and William S. Little who participated in the early stage of the experiment K^+p at 4.6 GeV/c.

Many thanks are due Dr. John A. Kadyk, Dr. Donald G. Coyne, Dr. W. Ralph Butler, Jonathan Chan, Allan Hirata, and Victor Seeger for useful conversations during the years I have been working in the Trilling-Goldhaber Group.

I would like to express my appreciation to Derik Armstrong, Emmett Burns, Bronwyn Hall, and Jim Miller for their aid in programming; Willie Lacy, Michael Healy, and Harriett Rice for bookkeeping; all the scanners who have worked on the experiments, especially Belinda Sieh and Bryce Sheldon, for their scanning and measuring the events.

I would like to thank the computer center staff and the Data Handling Group under Howard S. White for their aid and cooperation.

I wish to thank Charles Pezzotti who has patiently and carefully edited my thesis, Christina Frank for her careful and efficient typing, and Evelyn Grant for her help in making the drawings.

This work was supported by the U. S. Atomic Energy Commission.

APPENDIX I*

DOUBLE PERIPHERAL MODEL ANALYSIS OF THE REACTION $K^+p \rightarrow K^+\pi^-\Delta^{++}_{1236}$ AT 9 GeV/c

Chumin Fu

Lawrence Radiation Laboratory
University of California
Berkeley, California 94720

ABSTRACT

Using a double Regge-pole-exchange model, we studied the low $\Delta^{++}\pi^-$ mass enhancement in the reaction $K^+p \rightarrow K^+\pi^-\Delta^{++}_{1236}$ at 9 GeV/c. We found that P and π double exchange dominate the process. In general the model agrees with the data in the region where $M(K^+\pi^-) \gtrsim 1.54$ GeV and $-t_{KK} < 0.5$ (GeV/c)^2 and $-t_{p\Delta} < 0.5$ (GeV/c)^2. The possibility of extending the model into the large t region and problems involved in the extrapolation of the model to the $K\pi$ threshold are investigated. The importance of the contribution from the double peripheral process in low $M(K^+\pi^-)$ region and its implications to the analysis for the $K\pi$ system are discussed.

I. INTRODUCTION

The general features of the reaction $K^+p \rightarrow K^+\pi^-\Delta^{++}_{1236}$ at 9 GeV/c were discussed in an earlier communication.[1] In this paper we study the reaction in the high $K\pi$ mass region ($M(K^+\pi^-) \gtrsim 1.54$ GeV) on the basis of a double Regge-pole-exchange model. The advantage of this model is that it has the same simple form as a single Regge-pole-exchange model and theoretically the Regge parameters (except the coupling at the internal vertex) used here can be wholly taken from those that were determined by the data from two-body or quasi-two-body final states. As a known fact, a double-Regge-pole model can usually describe the data of the three-body or quasi-three-body final states at high energies fairly well. However, in applying the model, there are still some unsolved problems; namely,

1) The commonly used Regge parameters are known only to their order of magnitude. The exact values are not well determined. Hence when one finds that the fits of the model to the data are insensitive to the variation of the parameters, one cannot distinguish whether it is due to the effect of a collective change of the many Regge parameters or due to an incomplete study of the data. Poor statistics of the data and unclean samples could also contribute to the sources of uncertainties.

2) There is no evidence for Toller angular dependence at the internal vertex. By the same argument given in 1) above, it is not clear at all whether or not there should be a Toller angular dependence for the Reggeon-Reggeon-particle coupling.

3) How far in momentum transfer variables (t's) a peripheral model can extend is not well known.

4) Granted that the duality is a valid concept,[2]

*Modified version of paper to be published in Physical Review.

how would one extrapolate the model to small subinvariant energies (s's)? Would the extrapolation be insensitive to the variation of Regge parameters also? Answers to these questions are not known either.

With an attempt to understand these problems we analyze our data in an exhaustive manner. The method and the results of the analysis are presented in Secs. II and III. Section IV discusses the extrapolation of the model to small subinvariant energies. Section V gives our conclusions.

This experiment was carried out in the Brookhaven National Laboratory 80-inch hydrogen bubble chamber, which was exposed to a 9-GeV/c rf-separated K^+ beam at the AGS. The details of the experiments, the measurements, and the kinematical fitting procedures are described in Ref. 1 and the Ref. 5 therein.

II. THE MODEL AND THE METHOD OF ANALYSIS

A. The Model

There are many multiperipheral models and the phenomenological analyses of the data discussed in the literature.[3,4] Here we adopt the one given in Ref. 3c. Consider Fig. 1a, a diagram for the reaction a + b → 1 + 2 + 3. The invariant amplitude is

$$A(s, s_1, s_2, t_1, t_2) \approx \beta_1(t_1)\, \xi_1(t_1) \left(\frac{\tilde{s}_1}{s_{10}}\right)^{\alpha_1(t_1)} \times \beta_2(t_2)\xi_2(t_2)\left(\frac{\tilde{s}_2}{s_{20}}\right)^{\alpha_2(t_2)} \beta_3(t_1, t_2, \omega), \quad (1)$$

where s, s_1, s_2, and t_1 and t_2 are as indicated in Fig. 1a.

$$\tilde{s}_1 = s_1 - t_2 - m_a^2 + \frac{1}{2} t_1^{-1}(m_1^2 - m_a^2 - t_1)(m_3^2 - t_1 - t_2)$$

and $\tilde{s}_2$ is obtained by interchanging the subscripts 1 and 2. The Toller angle, ω, is defined by

$$\cos\omega = \frac{\vec{p}_a \times \vec{p}_1 \cdot \vec{p}_b \times \vec{p}_2}{|\vec{p}_a \times \vec{p}_1|\,|\vec{p}_b \times \vec{p}_2|}$$

in the rest frame of the particle 3. The α_i's are the Regge trajectories exchanged and

$$\xi_i = \frac{1 \pm e^{-i\pi\alpha_i(t_i)}}{\sin \pi\alpha_i(t_i)} .$$

The β_i's are the residue function. The s_{i0}'s are the energy scale constants.

For the reaction $K^+p \to K^+\pi^-\Delta^{++}_{1236}$, the allowable exchange pairs (α_1, α_2) are (P, π), (P, A_1), (ρ, π), (ρ, A_2), (ρ, A_1) and (ω, ρ). Consider the (P, π) pair only and further assume that P is a fixed pole with an intercept 1 in the Chew-Frautschi plot. After squaring Eq. (1) and some simplifications one obtains an intensity

$$I = N_0 e^{\gamma t_1} \frac{(\pi\alpha_\pi')^2}{1-\cos\pi\alpha_\pi(t_2)} (\tilde{s}_1)^2 \left(\frac{\tilde{s}_2}{s_0}\right)^{2\alpha_\pi(t)} f(\omega, t_1, t_2), \quad (2)$$

where $\alpha_\pi = \alpha_\pi'(t_2 - m_\pi^2)$ and N_0 is a normalization constant. This equation is the same as that given in Ref. 3e provided that we set $f(\omega, t_1, t_2)$ to be constant.

Since Pomeranchukon is not well understood at present and there are five exchange pairs other than (P,π) also allowed, for $K^+\pi^-$ mass between 1.54 and 2.8 GeV it is reasonable to replace $(\tilde{s}_1)^2$ by $(s_1)^{2c}$ in Eq. (2), where c is a constant parameter.

Using the notations indicated in Fig. 1b, we rewrite Eq. (2) as

$$I = N_0 e^{\gamma t_{KK}} \frac{(\pi\alpha_\pi)^{2c}}{1-\cos\pi\alpha_\pi(t_{p\Delta})} (\tilde{s}_{K\pi})^{2c} \left(\frac{\tilde{s}_{\Delta\pi}}{s_0}\right)^{2\alpha_\pi(t)} \times f(\omega, t_{p\Delta}, t_{KK}), \quad (3a)$$

which is to be used in this analysis. We assume that f takes the form

$$f = [1 + a(t_{p\Delta}/m_\pi^2)\cos\omega]^2, \quad (3b)$$

where a is a constant parameter. Equation (3b) is purely empirical. It has the property that f has no Toller angular dependence at $t_{p\Delta} = 0$, which is required on a theoretical basis.[4] In this analysis, there are five parameters involved, i.e., γ, α'_π, c, s_0 and a. Two cases are considered, namely

1) Case I: a = 0,
2) Case II: a is a free parameter.

B. The Method of Analysis

In comparing the data with the theoretical calculations we follow the procedures below:

1) Generate Monte Carlo events for the $K^+\pi^-\Delta^{++}_{1236}$ final states with a variable mass for the Δ^{++}_{1236} given by a Breit-Wigner distribution. [6]

2) Assign to each Monte Carlo event a weight according to Eq. (3a).

3) Compare the various distributions from the Monte-Carlo events with those from the data, and vary the parameters in Eq. (3a) until we obtain the best fit for all those distributions considered. The goodness of the fit is determined by a χ^2 calculation. [7]

In order to investigate the problems stated in the introduction, we choose to study the following three samples with $M(K^+\pi^-) > 1.54$ GeV:

Sample A: $-t_{K^+K^+}$ and $-t_{p\Delta^{++}} < 1.0$ (GeV/c)^2 (511 events).

Sample B: $-t_{K^+K^+}$ and $-t_{p\Delta^{++}} < 0.5$ (GeV/c)^2 (287 events).

Sample C: $-t_{K^+K^+}$ and $-t_{p\Delta^{++}} < 0.3$ (GeV/c)^2 (115 events).

The N_0 is determined by normalizing to sample B the Monte Carlo events with the same kinematic cuts as those imposed on sample B. The parameters γ, α'_π, c, s_0, and a are obtained by comparing the distributions of 12 variables from the events in sample B with those from the corresponding Monte Carlo events [three invariant masses, $M(K^+\pi^-)$, $M(\Delta^{++}\pi^-)$, and $M(K^+\Delta^{++})$, four four-momentum transfers, $-t_{KK'}$, $-t_{p\Delta'}$, $-t_{K\pi'}$, and $-t_{p\pi'}$, and five angular variables, $\cos\theta(K^+\pi^-)$, $\phi(K^+\pi^-)$, $\cos\theta(\Delta^{++}\pi^-)$, $\phi(\Delta^{++}\pi^-)$, and ω]. The θ and ϕ are the Jackson angle and the Treiman-Yang angle for a two-particle composite. If the model is valid and the parameters obtained are correct, then one should expect good agreements between the various distributions from the Monte Carlo events and those from the data in a t region where the t cuts are smaller than what sample B has. Furthermore one can also test the validity of the model in a large t region by extending the t cuts imposed on the data and the Monte Carlo events. These are the motivations for studying samples C and A. In principle one should compare the model with the data in different noninclusive t intervals. Due to the statistical limitations of our data, we can only choose the t criteria as we described earlier.

III. RESULTS

Various values for the parameters in Eq. (3a) have been tried; the best values obtained are

Case I: a = 0, $\gamma = 4$ (GeV/c)$^{-2}$, $\alpha'_\pi = 1.2$ (GeV/c)$^{-2}$, $s_0 = 1.0$ (GeV)^2, and c = 0.85

Case II: a = 0.015, $\gamma = 3.2$ (GeV/c)$^{-2}$, $\alpha'_\pi = 1.12$ (GeV/c)$^{-2}$, $s_0 = 1.0$ (GeV)^2, and c = 0.85.

A. The Distributions of the Various Kinematic Variables

For each variable the distributions are to be presented in the order of Samples A, B, and C. The corresponding distributions from the Monte Carlo events are shown in solid lines for case I and long dash lines for case II.

Figure 2 shows the Δ^{++}_{1236} mass distributions. Here we check whether the Monte Carlo events generated for the $K^+\pi^-\Delta^{++}_{1236}$ final state indeed have a $p\pi^+$ mass distribution similar to that of the samples. Comparing the data with the curve shown in Fig. 2b, we obtain a $\chi^2 = 16.4$ and a confidence level = 12.6% with 14 degrees of freedom. (We consider M_0, Γ_0, and a as parameters in the Breit-Wigner distribution discussed in Ref. 6. The curves corresponding to case I and case II are very close, therefore only the result of case I is shown in Fig. 2.)

Figure 3a, b, and c shows the $K^+\pi^-$ mass spectra for samples A, B, and C respectively. The short-dash lines are the extrapolations of the model calculations to the region where $M(K^+\pi^-) < 1540$ MeV. Discussions of the extrapolation are given in Sec. IV. In Fig. 3b the two curves are close in the region where $M(K^+\pi^-) \geq 1700$ MeV. Below 1700 MeV in the $K^+\pi^-$ mass two curves start to deviate. The deviation between the solid and the long dash lines become larger for sample A and smaller for sample B. This seems to be a general trend shown also in the other distributions we discuss later.

Figures 4a, b, and c and Figs. 4d, e, and f show the $\Delta^{++}\pi^-$ mass distributions and the $K^+\Delta^{++}$ mass distributions. In Fig. 4a the data peak at around 1500 MeV, where there are three I = 1/2 baryonic resonances, P_{11}, D_{13}, and S_{11}.[8] The calculated curves peak at about 80 MeV above 1500 MeV. However, in Figs. 4b and c the curves agree with the data. The curves from the model shift their peak by 80 MeV in the $\Delta^{++}\pi$ mass from Fig. 4a to Figs. 4b and c, yet the data do not show such an apparent change. This indicates that the model may very well apply to small t regions (e.g., samples B and C) but does not apply to the large t regions (e.g., sample A). Similar disagreements also show some of the distributions from sample A discussed in the following paragraphs. In Fig. 4d the dashed curve agrees with the data better than the solid curve, but it is not so obvious in Figs. 4e and f.

Figures 5 and 6 show the distributions of $-t_{KK}$ and $-t_{p\Delta}$, and $-t_{K\pi}$ and $-t_{p\pi}$. Except for $-t_{p\pi}$ in Fig. 6e and f, in general the model (for both case I and case II) agrees well with the data.

Figure 7 shows the decay angular distributions for the $K^+\pi^-$ system in its rest frame. The cos θ distribution (Figs. 7a, b, and c) are plotted from 0 to 1.0 since there are no events from the data and the model in the backward region. As the t cuts decrease, the events are populated even in a smaller forward region [e.g., $\cos\theta(K^+\pi^-) \geq 0.7$ for both $-t_{KK}$ and $-t_{p\Delta}$ less than 0.3 $(\mathrm{GeV}/c)^2$]. The Treiman-Yang angular distribution (Figs. 72, f, and g) becomes flatter as $t_{p\Delta}$ decreases. This indicates that the Treiman-Yang angular distribution tends to agree with the well-known prediction of single-pion particle exchange in the limit of very small $-t_{p\Delta}$.[9] The solid curve and the dashed curve show considerable discrepancy in Fig. 7d (sample A). Otherwise, for both case I and case II the model agrees with the data rather well.

Figure 8 shows the distributions of the cosθ and ϕ for the $\Delta^{++}\pi^-$ system. Again a large discrepancy between the curves is observed in large t regions (Figs. 8a and d). Figure 9 shows the Toller angular distributions. The model agrees with the data fairly well for Sample B, but does not agree with the data in both the large t region (sample A) and the small t region (sample C). The dash-dot lines in Fig. 9 represent the phase space which is normalized to each sample. It strongly peaks near ω = 180 deg. At ω = 180 deg, the two particles in the initial state and the three particles in the final state lie in the same plane. As t cuts decrease, the phase space curve is getting closer to the results of the model and the data points.

The χ^2 values of the various distributions for sample B are given in Table I. Table I indicates:

1) Over all the kinematical variables studied the confidence level of case II is more uniform than that of case I. Consider the latter if one happens to choose to fit the distributions of $M(K^+\pi^-)$, $M(K^+\Delta^{++})$, $-t_{p\Delta}$, and $-t_{K\pi}$ one may claim very good agreement between the model and the data. On the other hand if one chooses the variables $M(\Delta^{++}\pi^-)$, $-t_{KK}$, $-t_{p\pi}$, and the

Toller angle, ω, one may consider that the model is a failure. The results could be even worse if only some of the distribution from sample A were considered.

2) The agreement between the model and the data is poor for the distributions of $-t_{KK}$, $-t_{p\pi}$, and ω.

B. A Quantitative Analysis

Comparison of the number of events from the model and the phase space with the data under different kinematical criteria is shown in Table II. The normalization was described in Sec. IIB.

We observe the following:

1) Comparing the numbers from the data and those from the phase space, one can easily see the peripheral nature of the data.

2) For $M(K^+\pi^-) \geq 1540$ MeV, the number of events from the data agrees with the result of the model for both case I and case II. The model completely disagrees with the data in the low $K^+\pi^-$ mass region [$M(K^+\pi^-) < 1540$ MeV] as we expect (because of the strong K^* resonance productions). One important point to note is that the predictions of case I and case II disagree in this $K^+\pi^-$ mass region also.

IV. EXTRAPOLATION OF THE MODEL TO SMALL SUBENERGIES

In this section we discuss: (a) the importance of the contribution from the extrapolation, (b) the reliability of the extrapolation with the present knowledge of Regge parameters, and (c) the isospin structure of the $K\pi$ system on the basis of (P, π) exchange in the model.

(a) In order to demonstrate the contribution from the double peripheral process by extrapolation, in Figs. 10a, b, and c we plot the complete $K^+\pi^-$ mass spectra under the t cuts, $-t_{KK}$ and $-t_{p\Delta}$ less than 1.0 $(GeV/c)^2$, 0.5 $(GeV/c)^2$, and 0.3 $(GeV/c)^2$ respectively. The curves shown in Figs. 10a, b, and c are the same as those shown in Figs. 3a, b, and c.

The extrapolation of the model to the small $K\pi$ mass region as shown by the dashed curves in Fig. 10 does not describe the data in the K^*_{890} resonance region, not in a crude average sense. This seems to be in favor of Harari postulate[10] that Pomeranchukon exchange is responsible for the background only. The double peripheral process would contribute at least 30 to 60% of the background in the low $K\pi$ mass region [$M(K^+\pi^-) < 1540$ MeV]. Due to the $e^{\gamma t_{KK}}$ factor in Eq. (3a), the model yields a large intensity in the forward $\theta(K^+\pi^-)$ region even in the low $K\pi$ mass region (except near the $K\pi$ threshold). This contributes to part of the well-known forward-backward asymmetry in the $K\pi$ system.[11] Ignoring the isospin structures, calculations involving a p-wave K^*_{890} and a d-wave K^*_{1420} with a coherent and an incoherent double peripheral process with (P, π) exchange have been tried. They do not produce some of the important features in $K\pi$ asymmetry as a function of $K\pi$ mass. Since the contribution from the extrapolation to the background is large and yet it cannot account for all the background beside the two well-established K^*'s, one may ask whether the double peripheral process or the K^* resonance productions can be isolated from the data in order to obtain a relatively clean sample. The answer to this question is no, because both processes are dominated by pion exchange and in favor of small $-t_{p\Delta}$.

(b) In Table II the numbers of events in the low $K\pi$ mass region from the extrapolation of the model differ by about 30% between case I and II. This is a typical fluctuation, introduced to a certain extent by the uncertainties of the parameters used in Eq. (3a). With the present knowledge about Regge parameters and the statistical level of the data, one cannot determine how much each exchange pair (discussed in Sec. IIA) contributes, or whether one should try to find a better new model. Hence at the present stage the extrapolation of the model can only offer a qualitative description for the data.

(c) In order to determine the isospin of the $\Delta^{++}\pi$ enhancement, we compare the $\Delta^{++}\pi$ mass spectrum from both $K^0\pi^0\Delta^{++}$ and $K^+\pi^-\Delta^{++}$ final states as shown in Fig. 11. We note that for the reactions $K^+p \to K^0\pi^0\Delta^{++}$ and $K^+p \to K^+\pi^-\Delta^{++}$, the initial channel has a unique isospin state, namely $I = 1$, $I_z = 1$. Conservation of I and I_z requires $I = 3/2$ for the $\Delta^{++}\pi^0$ system and $I = 3/2$ or $1/2$ for the $\Delta^{++}\pi^-$ system. Since there is no excess of events near 1.58 GeV in the $M(\Delta^{++}\pi^0)$ plot (Fig. 11a) and the Clebsch-Gordan coefficients for an $I = 3/2$ ($\Delta\pi$) system predict a ratio of 9:2 for the intensity of the $\Delta^{++}\pi^0$ and $\Delta^{++}\pi^-$ states, the $\Delta^{++}\pi^-$ low-mass enhancement is predominantly $I = 1/2$. This isospin assignment is in favor of an $I = 0$ object exchanged at the $K^+_{in}K^+_{out}$ vertex. Among all the allowed exchange pairs (see Sec. IIA) the P is the only candidate with $I = 0$.

In fact we obtain $C \approx 0.85$, which is close to unity, in this analysis. This agrees with the assumption that P is the dominant object exchanged at the K^+K^+ vertex. Comparing (P, π) and (P, A_1), if one assuming α_π and α_{A_1} have the same slope, then A_1 would be a lower trajectory and its pole is farther away from the physical region than the pion pole. Hence the contribution of A_1 is less important than that of π. If one assumes π and A_1 degeneracy then there should be no essential difference whether (P, A_1) is included or not in addition to (P, π). The comparison of the model and the data also indicates that our (P, π) assumption is rather good at least in the region where $-t_{KK}$ and $-t_{p\Delta}$ are small. These arguments justify the assumption that the (P, π) exchange pair dominates the double peripheral process. Then one can further study the upper part of the diagram in Fig. 1b as a K^+_{in} scattered by a virtual pion producing the $K^+\pi^-$ final state with P exchanged in the t channel.[12] By isospin crossing for the reaction $K^+\pi^- \to K^+\pi^-$ via an $I = 0$ object exchanged in the t channel, the $I = 3/2$ and $I = 1/2$ parts of the amplitude are in 1:2 ratio. The implications of this is that we cannot neglect the $I = 3/2$ component in doing analysis for the $K\pi$ system in low $K\pi$ mass region. Whether the $K\pi$ asymmetry can be explained by including the $I = 3/2$ component is completely unclear.

V. CONCLUSIONS

1. (P, π) exchange dominates the reaction $K^+p \to K^+\pi^-\Delta^{++}_{1236}$ at 9 GeV/c for $M(K^+\pi^-) \geq 1540$ MeV. In general the model agrees with the data fairly well for $-t_{KK} < 0.5\ (\mathrm{GeV/c})^2$ and $-t_{p\Delta} < 0.5\ (\mathrm{GeV/c})^2$. The validity of the model above these t cuts is definitely in doubt.

2. The introduction of an empirical Toller angular dependence at the internal vertex helps to improve the condifence level to be more uniform over the distribution of all the variables considered except that the fit to the Toller angular distributions itself has not been improved much. In the small t region, the Toller angular distribution (as shown in Fig. 9c) indicates a large discrepancy between the model and the data. Further investigation on Toller angular dependence is necessary.

3. With the present knowledge of the Regge parameters determined by the data from two-body final states, the many possibilities of the exchange pairs, and the statistical limitation of our data, the values of the Regge parameters we used are subject to considerably large uncertainties. However, this should not affect the conclusion that the contribution from the extrapolation is large. By comparing the data with the result from the extrapolation to small $K\pi$ mass region, we find that the latter agrees with Harari's postulate that Pomeran exchange is responsible for the background only.

ACKNOWLEDGMENTS

I would like to acknowledge Professor G. Goldhaber, Dr. E. L. Berger, Dr. A. Firestone, and Dr. P. D. Ting for their critical comments and discussions. I thank Dr. R. Shutt and the staff of the 80-inch bubble chamber and Dr. H. Foelsche and the AGS staff at Brookhaven for helping with the exposure. I am also thankful for the valuable support given by the White and the FSD staff and by our programming and scanning staff, in particular Emmett R. Burns.

FIGURE CAPTIONS

Fig. 1. A double-Regge-pole-exchange diagram for (a) a reaction $a + b \to 1 + 2 + 3$ and (b) the reactions $K^+p \to K^+\pi^-\Delta^{++}_{1236}$.

Fig. 2. Mass distributions for Δ^{++}_{1236} (1120 to 1320 MeV) for samples (a) A, (b) B, and (c) C. The solid curves show the distributions for Monte Carlo events.

Fig. 3. $K^+\pi^-$ mass distributions for samples (a) A, (b) B, and (c) C. The solid and the long-dash curves correspond to cases I and II respectively. The short-dash curves are the extrapolation of the cases I and II.

Fig. 4. $\Delta^{++}\pi^-$ mass distributions for samples (a) A, (b) B, and (c) C, and $K^+\Delta^{++}$ mass distributions for samples (d) A, (e) B, and (f) C. The solid and the long-dash curves, the results from the model, bear the same meaning as those shown in Fig. 3.

Fig. 5. $-t_{K^+K^+}$ distributions for samples (a) A, (b) B, and (c) C, and $-t_{p\Delta^{++}}$ distributions for samples (d) A, (e) B, and (f) C. The curves bear the same meaning as those shown in Fig. 4.

Fig. 6. $-t_{K^+\pi^-}$ distributions for samples (d) A, (e) B, and (f) C. The curves bear the same meaning as those shown in Fig. 4.

Fig. 7. $\cos\theta(K^+\pi^-)$ distributions for samples (a) A, (b) B, and (c) C and $\phi(K^+\pi^-)$ distributions for samples (d) A, (e) B, and (c) C. $\theta(K^+\pi^-)$ and $\phi(K^+\pi^-)$ are the Jackson angle and the Treiman-Yang angle for the $K^+\pi^-$ system. The curves bear the same meaning as those shown in Fig. 4.

Fig. 8. $\cos\theta(\Delta^{++}\pi^-)$ distributions for samples (a) A, (b) B, and (c) C and $\phi(\Delta^{++}\pi^-)$ distributions for samples (d) A, (e) B, and (f) C. $\theta(\Delta^{++}\pi^-)$ and $\phi(\Delta^{++}\pi^-)$ are the Jackson angle and the Treiman-Yang angle for the $\Delta^{++}\pi^-$ system. The curves bear the same meaning as those shown in Fig. 4.

Fig. 9. Toller angular distributions for samples (a) A, (b) B, and (c) C. The solid and the long-dash curves bear the same meaning as those shown in Fig. 4. The dash-dot curve indicates the phase space normalized to each sample.

Fig. 10. $K^+\pi^-$ mass distributions with $-t(K^+K^+)$ and $-t(p\Delta^{++})$ less than (a) 1.0 $GeV/c)^2$, (b) 0.5 $(GeV/c)^2$, and (c) 0.3 $(GeV/c)^2$. The solid and the dashed curves bear the same meaning as those shown in Fig. 3.

Table I. χ^2 values for sample B.[a]

Distribution	χ^2	d. f.[b]	Confidence level (%)	χ^2	d. f.[b]	Confidence level(%)
$M(K^+\pi^-)$	8.1	14	88.3	16.1	13	17.1
$M(\Delta^{++}\pi^-)$	18.3	11	7.3	15.2	10	12.5
$M(K^+\Delta^{++})$	8.7	9	46.4	10.8	8	21.5
$-t_{KK}$	20.8	6	0.2	11.4	5	4.4
$-t_{p\Delta}$	3.8	3	27.9	3.5	2	17.7
$-t_{K\pi}$	5.9	5	31.5	6.1	4	19.1
$-t_{p\pi}$	20.3	7	0.5	12.9	6	4.5
$\cos\theta\,(K^+\pi^-)$	22.2	12	3.5	12.9	11	29.4
$\phi\,(K^+\pi^-)$	23.3	17	14.1	19.6	16	23.9
$\cos\theta\,(\Delta^{++}\pi^-)$	32.3	15	0.6	19.3	14	15.3
$\phi\,(\Delta^{++}\pi^-)$	28.2	12	0.8	18.0	11	11.5
Toller angle ω	29.1	10	1.2	15.8	9	7.0

[a] See Ref. 6.

[b] Degrees of freedom.

Table II. Comparison of the number of events from the model and the phase space with the data under different kinematical criteria.

	$M(K^+\pi^-) \geq 1540$ MeV			$M(K^+\pi^-) < 1540$ MeV		
	Sample A	Sample B	Sample C	$-t_{KK}$ and $-t_{p\Delta}$ $< 1.0\ (\mathrm{GeV}/c)^2$	$-t_{KK}$ and $-t_{p\Delta}$ $< 0.5\ (\mathrm{GeV}/c)^2$	$-t_{KK}$ and $-t_{p\Delta}$ $< 0.3\ (\mathrm{GeV}/c)^2$
Data	511	287	115	1804	1375	953
Case I	536	287	127	327	307	251
Case II	500	287	132	461	404	318
Phase space	1805	287	54	2565	824	330

FOOTNOTE AND REFERENCES

*Work supported by the U. S. Atomic Energy Commission.

1. C. Fu, A. Firestone, G. Goldhaber, and G. H. Trilling, Nucl. Phys. B18, 93 (1970).

2. a) R. Dolen, D. Horn, and C. Schmid, Phys. Rev. 166, 1768 (1968).

b) G. F. Chew and A. Pignotti, Phys. Rev. Letters 20, 1078 (1968).

3. a) N. F. Bali, G. F. Chew, and A. Pignotti, Phys. Rev. Letters 19, 614 (1967) and Phys. Rev. 163, 1572 (1967).

b) Chan Hong-Mo, K. Kajantie, and G. Ranft, Nuovo Cimento 49, 157 (1967) and E. Flamino, Nuovo Cimento 51, 696 (1967).

c) Review talks given by Chan Hong-Mo and S. Ratti in Topical Conference on High-Energy Collisions of Hadrons, CERN, January 1968.

d) Review talks by Chan Hong-Mo and O. Czyzewski, in Proceedings of the 14th International Conference on High-Energy Physics, Vienna, 28 August-5 September, 1968 (CERN, 1968).

e) Review talk given by J. D. Jackson, in Proceedings of the Lund International Conference on Elementary Particles, Lund, Sweden, June 25-July 1, 1969 (Berlingska Boktryckeriet Lund, Sweden, 1969).

f) G. Ranft, Fortschr. Physik (in press).

g) E. L. Berger, Phys. Rev. 179, 1567 (1969).

4. Double peripheral model analyses on $K\pi\Delta^{++}$ final states; see:

a) G. Bassompierre et al., Nucl. Phys. B14, 143(1969) on the reaction $K^+p \rightarrow K^+\pi^-\Delta^{++}$ at 5 GeV/c.

b) J. Andrews, J. Lach, T. Ludlam, J. Sandweiss, H. D. Taft, and E. L. Berger, Phys. Rev. Letters 22, 731(1969) on the reaction $K^-p \rightarrow K^-\pi^-\Delta^{++}$ at 12.6 GeV/c.

Many phenomenological analyses on the other reactions were reviewed in references 3(b), (c), (d), and (e).

5. J. M. Kosterlitz, Nucl. Phys. B9, 273 (1969).

6. A. Breit-Wigner distribution of the form $M_0\Gamma/[M_0{}^2 - M)^2 + \Gamma^2 M_0{}^2]$ with $\Gamma = (\Gamma_0/M)(p/p_0)^3\,(am_\pi{}^2 + p_0{}^2)/(am_\pi{}^2 + p^2)$ is used. The M is the $p\pi^+$ invariant mass. The M_0 is the mass of M at resonance. The p and p_0 are the momenta of the proton in the $p\pi^+$ cm system at a mass M and M_0 respectively. Here we take $M_0 = 1236$ MeV, $\Gamma_0 = 120$ MeV, and a = 1. Detailed discussions on the phenomenological analysis of resonances are in J. D. Jackson, Nuovo Cimento 36, 1644 (1964).

7. The $\chi^2 = \sum_{i=1}^{N} [N_D^i - N_{mc}^i)]$ where the N_D^i and the N_{mc}^i are the number of events from the data and the Monte Carlo calculation of the model in the ith bin of a distribution. Due to the statistical fluctuations we, in some cases, combine several bins into one.

8. Particle Data Group, Rev. Mod. Phys. 42, 87 (1970).

9. S. B. Treiman and C. N. Yang, Phys. Rev. Letters 8, 140 (1962).

10. H. Harari, Phys. Rev. Letters 20, 1395 (1968).

11. a) An earlier discussion was given by C. Fu, A. Firestone, G. Goldhaber, and G. H. Trilling in APS Washington Meeting, April 1969; Study of the $K\pi$ System in the Reaction $K^+p \quad K^+\pi^-\Delta^{++}$ at 9 GeV/c; see also Ref. 1.

b) C. Fu, A. Firestone, G. Goldhaber, G. H. Trilling, and B. C. Shen, Lawrence Radiation Laboratory Report UCRL-18201 (1968).

12. Huan Lee, J. Math. Phys. 10, 779 (1969) and the references therein.

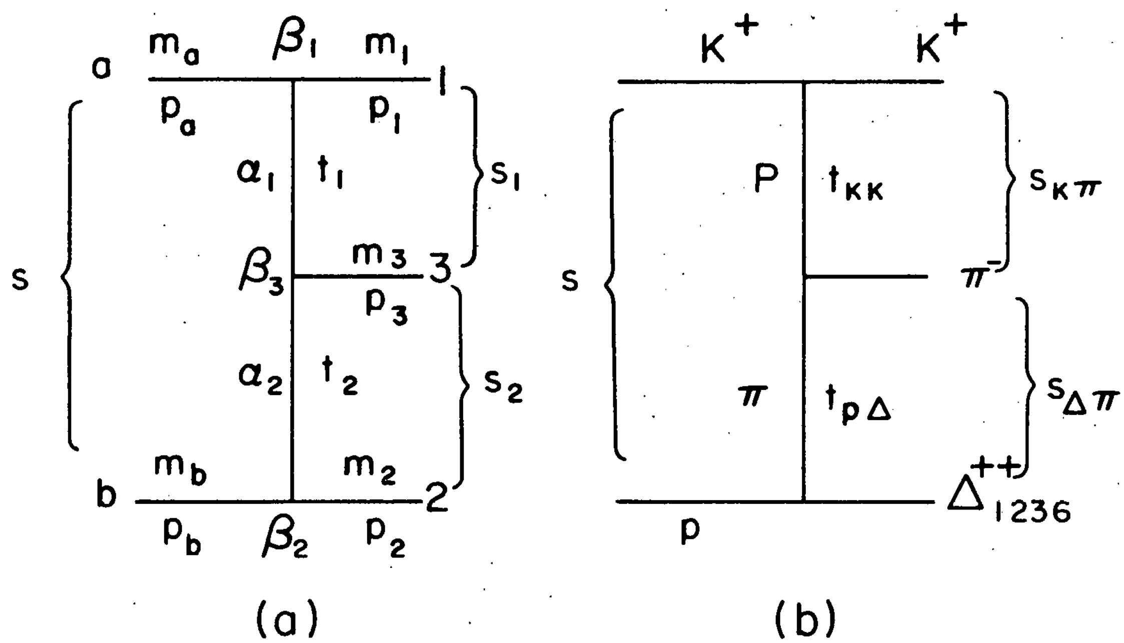

Fig. 1. XBL703-2462

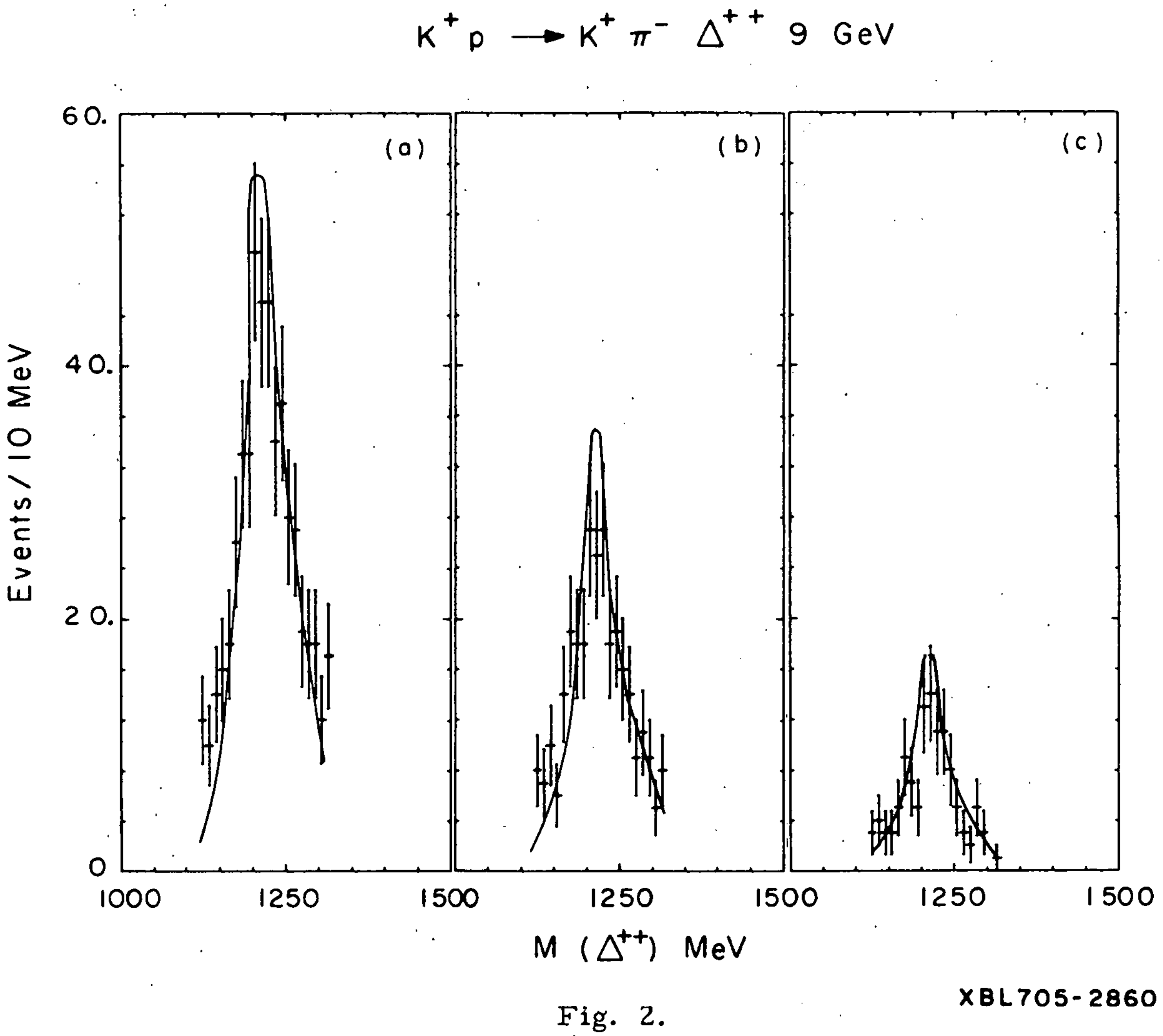
K+p → K+ π- Δ++ 9 GeV
(a)
(b)
(c)
Events / 10 MeV
60.
40.
20.
0
1000
1250
1500
1250
1500
1250
1500
M (Δ++) MeV
XBL705-2860

Fig. 2.

$K^+ \pi^- \Delta^{++}$ 9 GeV/c

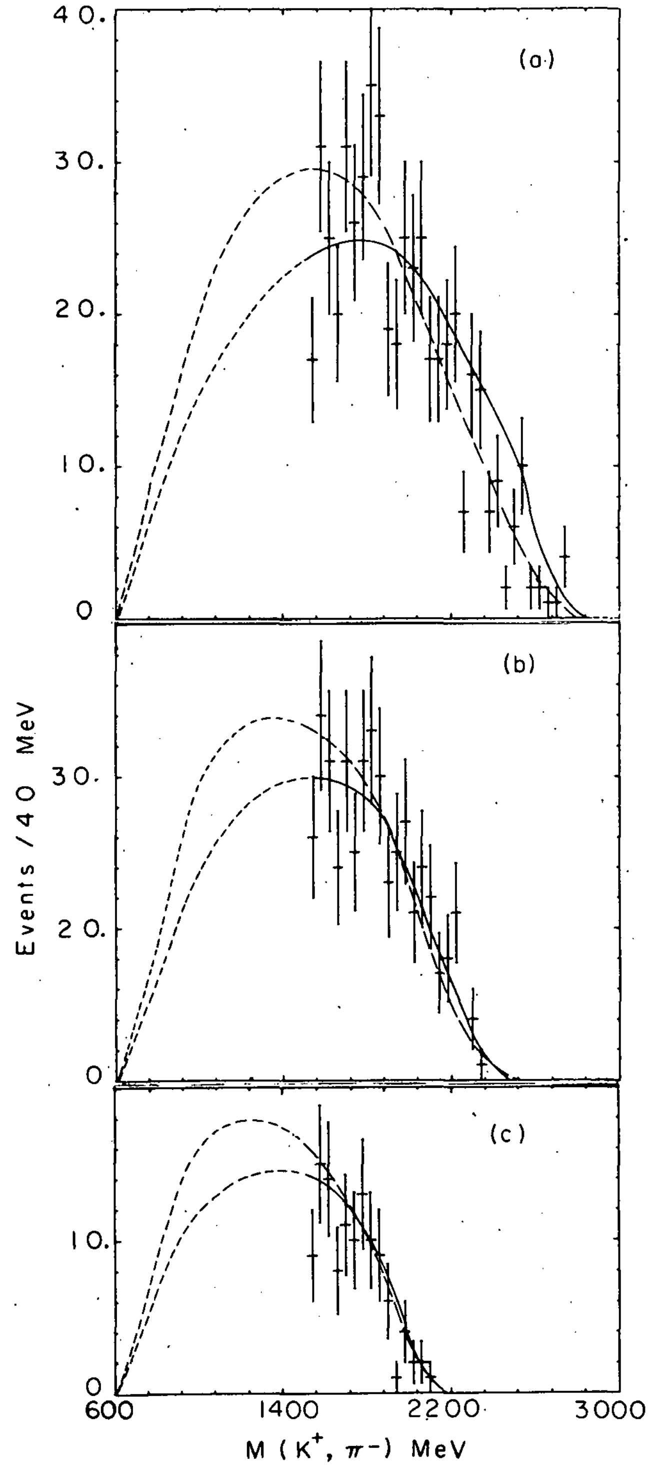

Fig. 3.

XBL705-2859

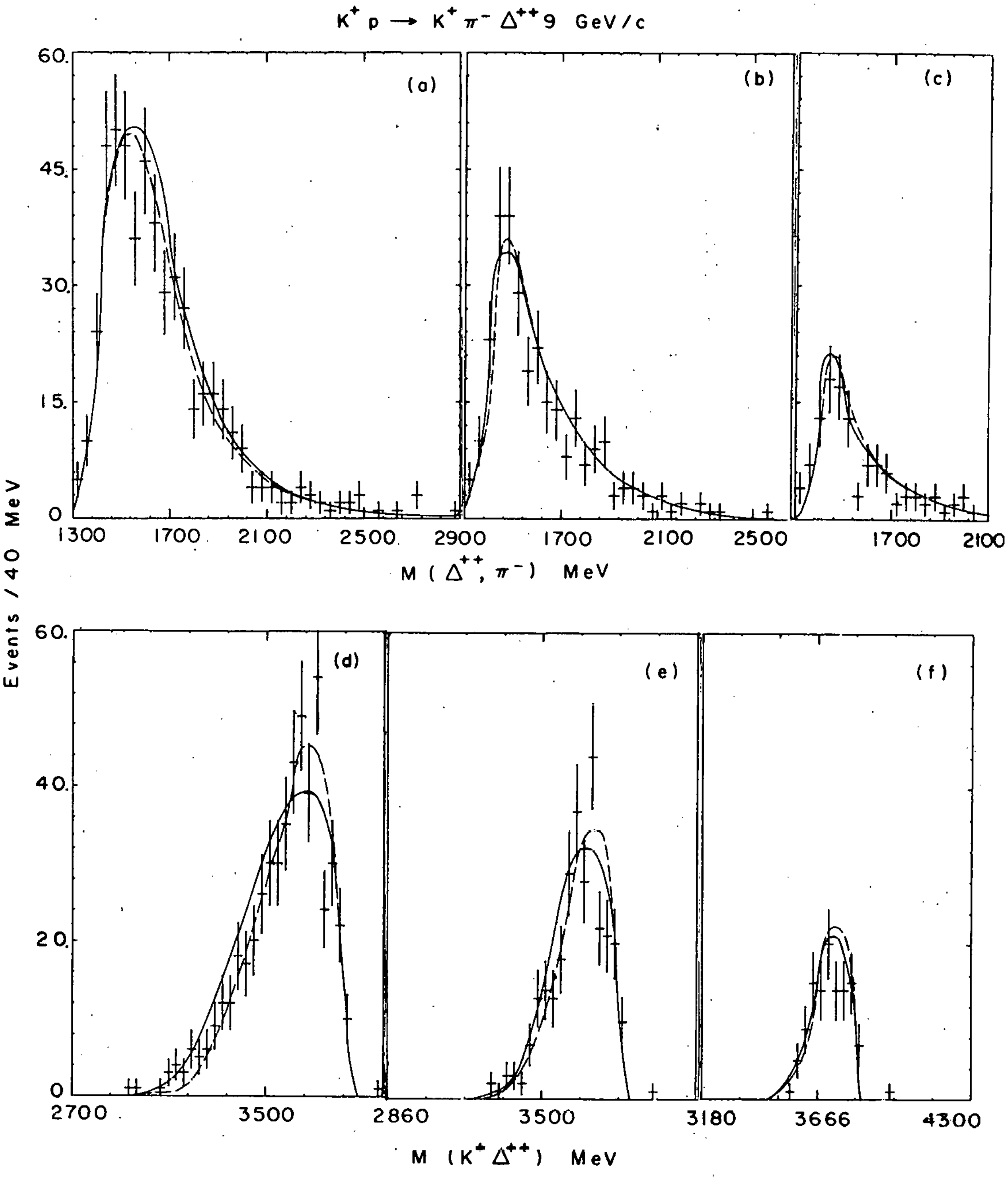

Fig. 4.

XBL705-2855

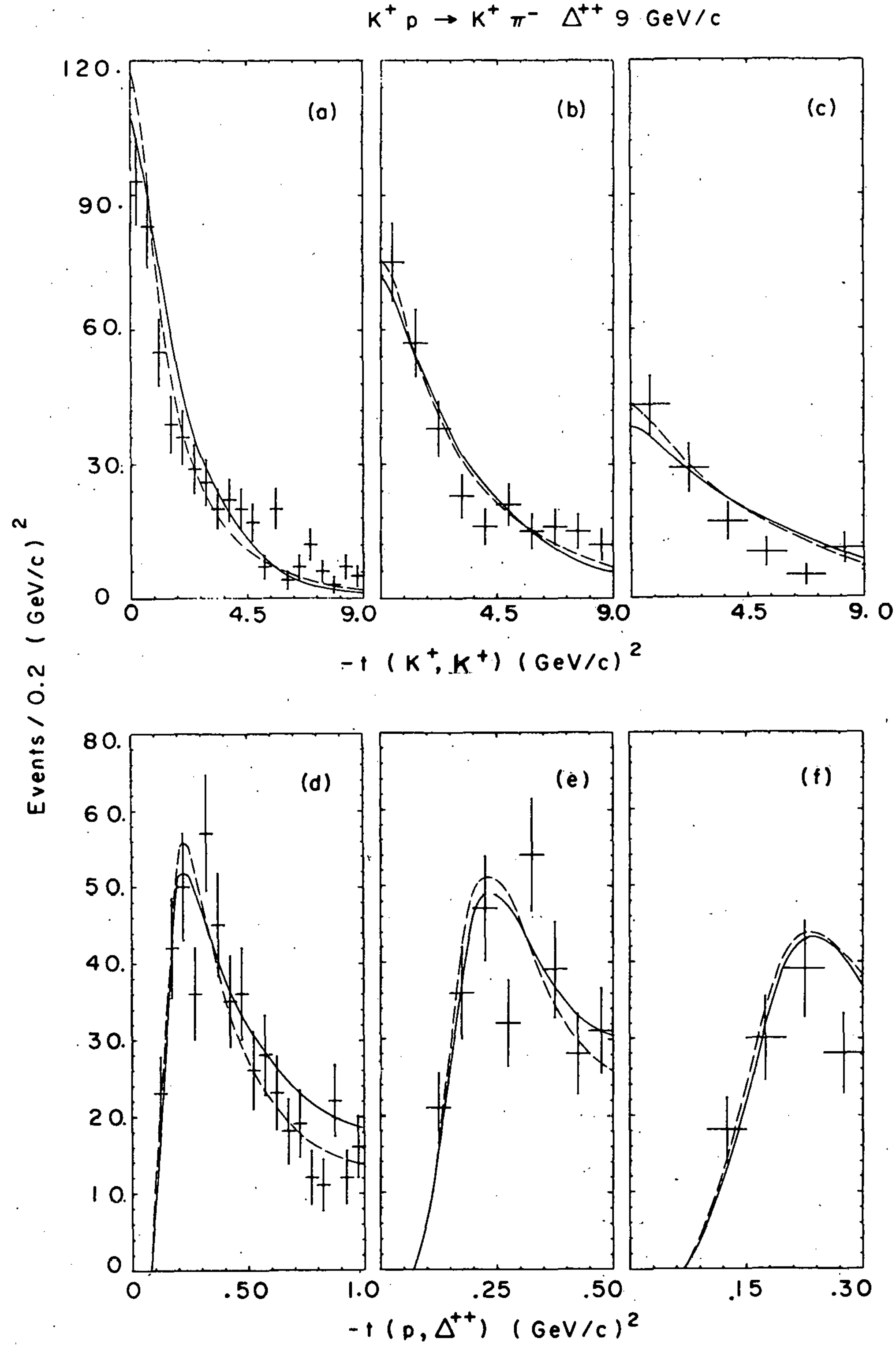

Fig. 5.

XBL705-2861

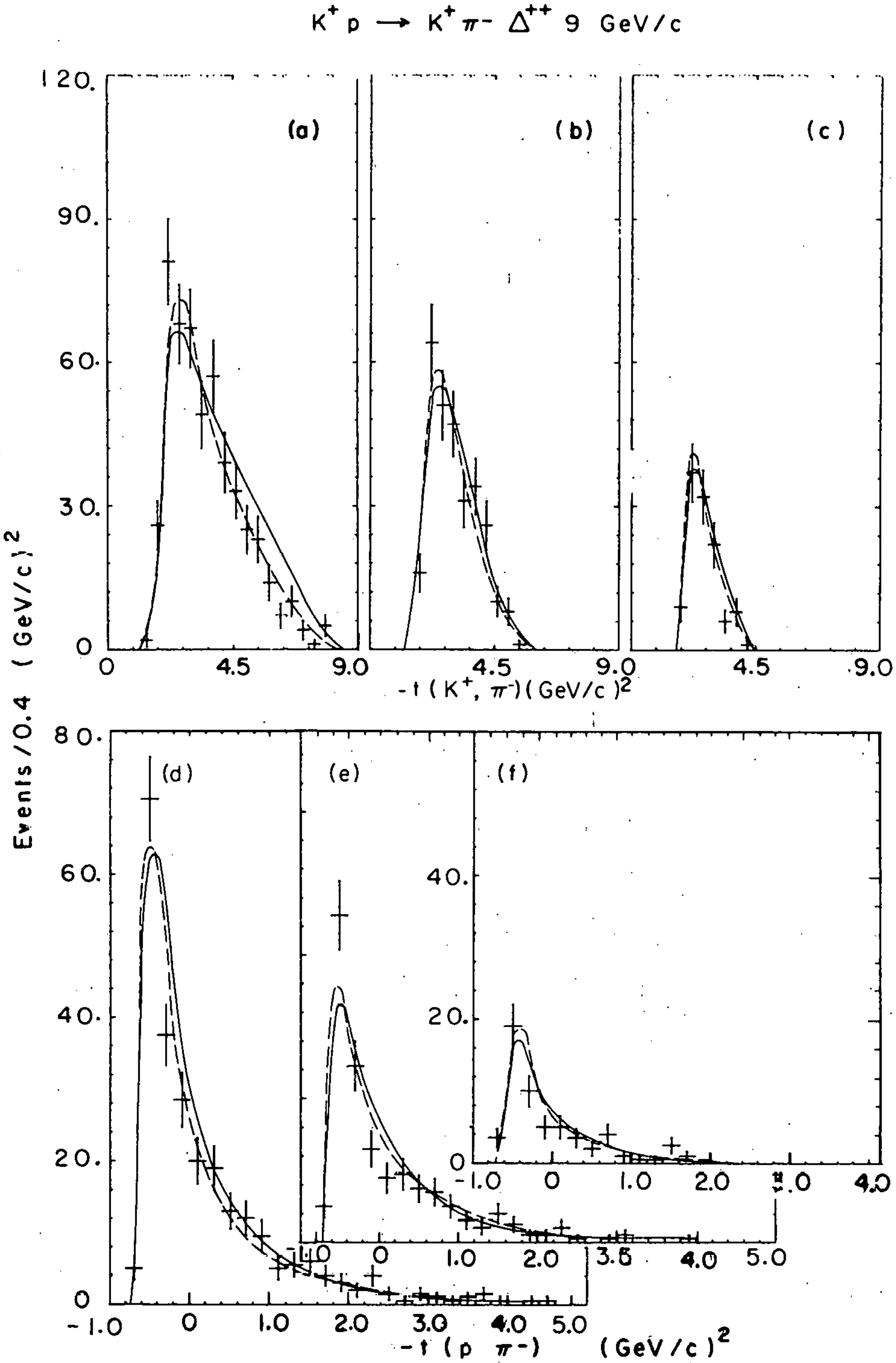

Fig. 6.

XBL705-2856

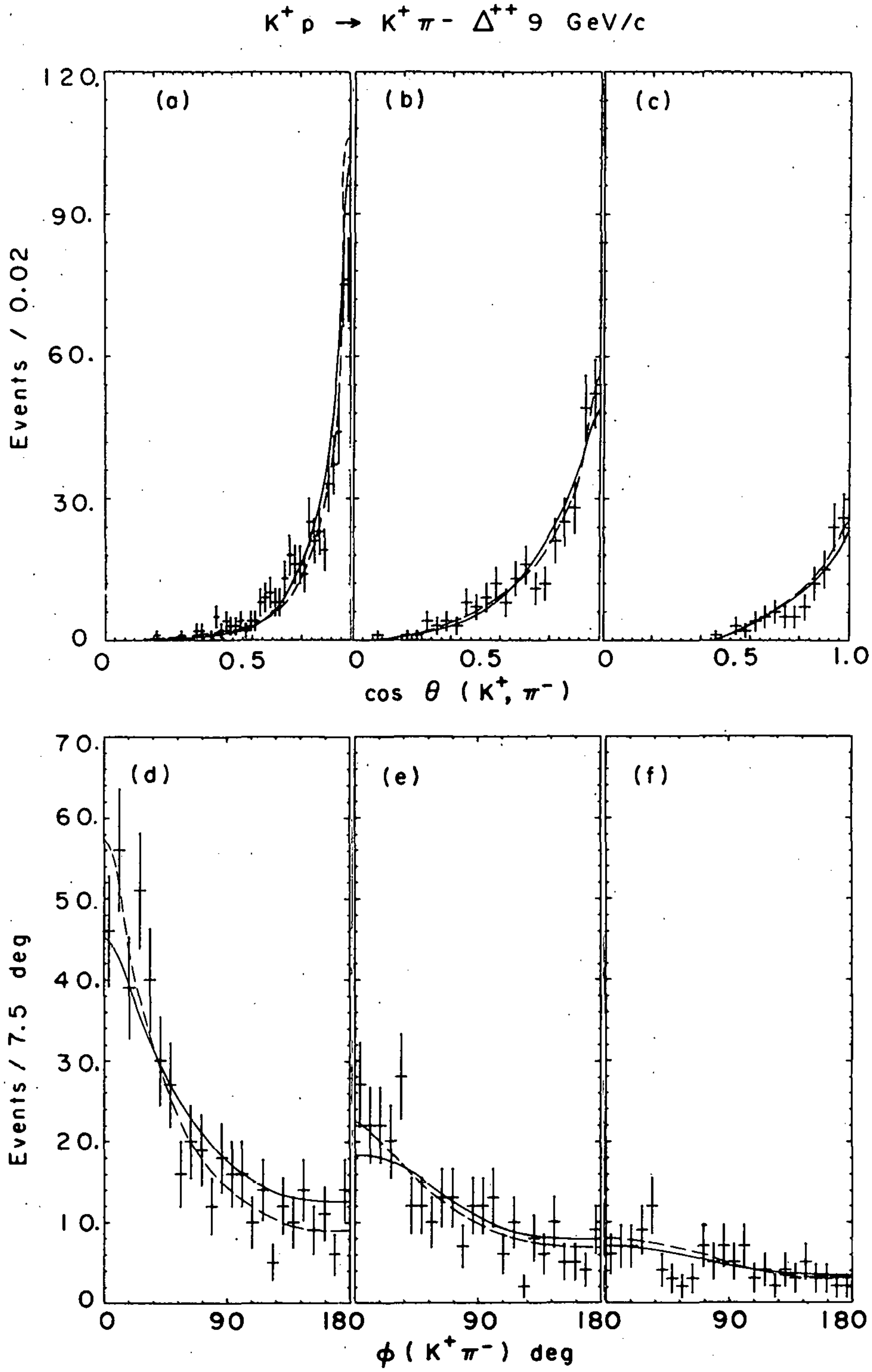

Fig. 7.

XBL705-2854

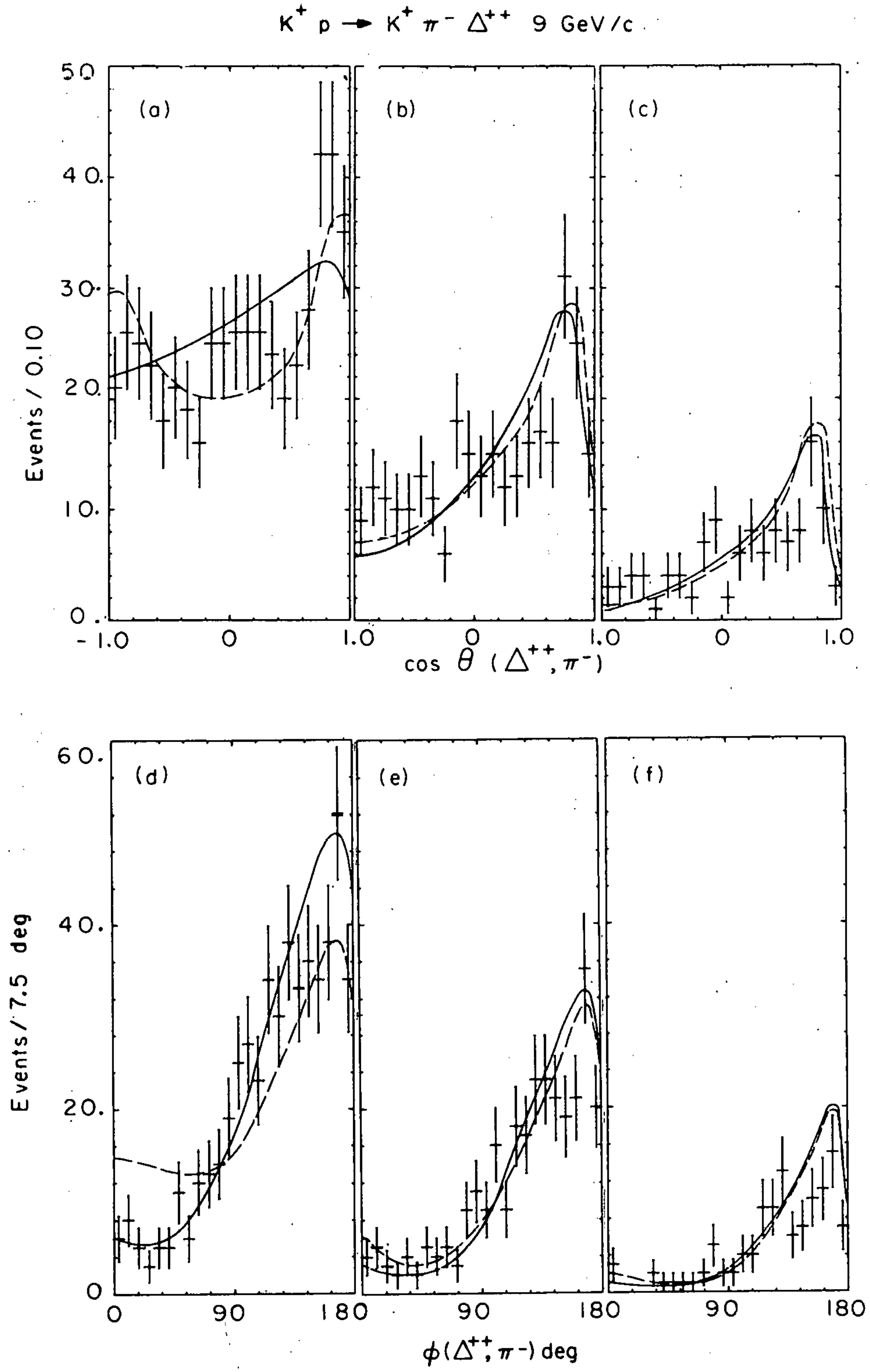

Fig. 8.

XBL705-2857

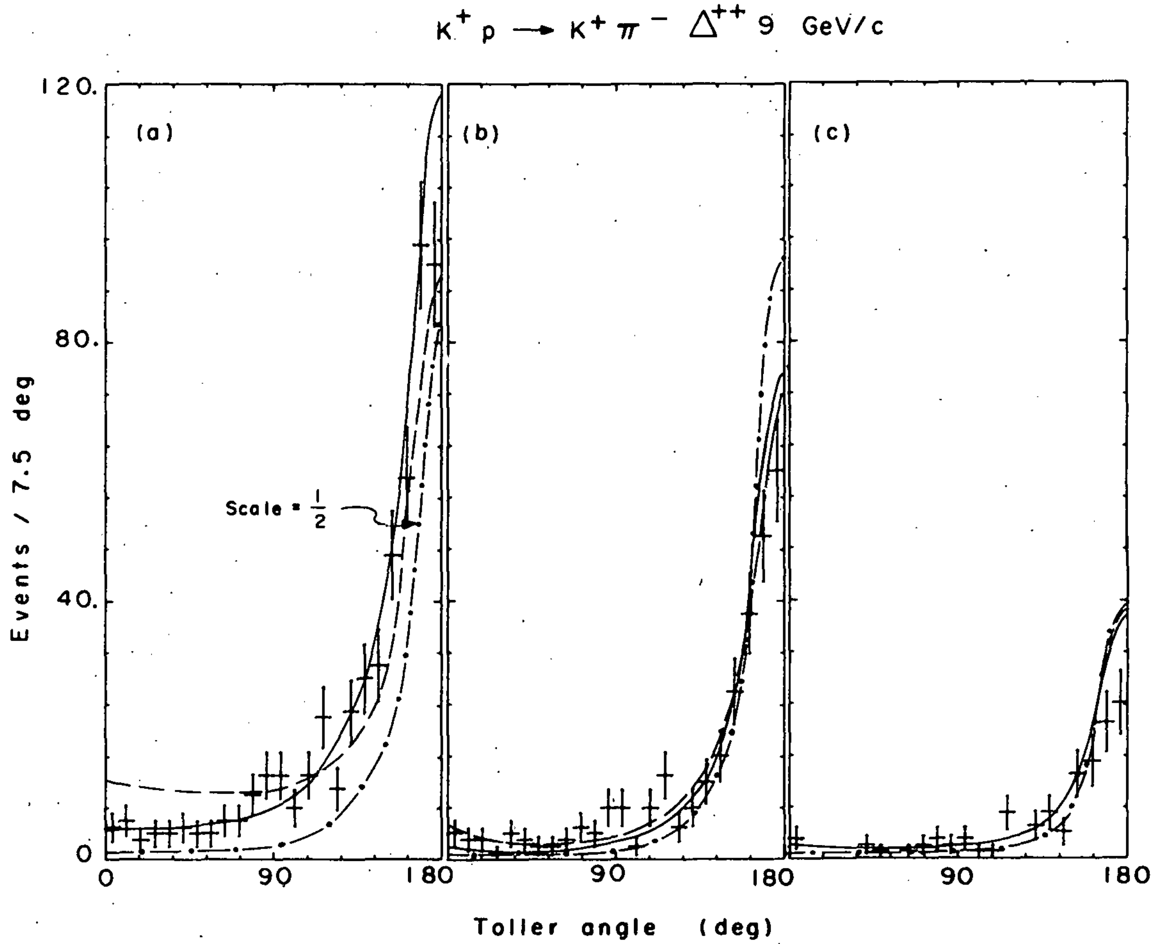

Fig. 9.

XBL705-2858

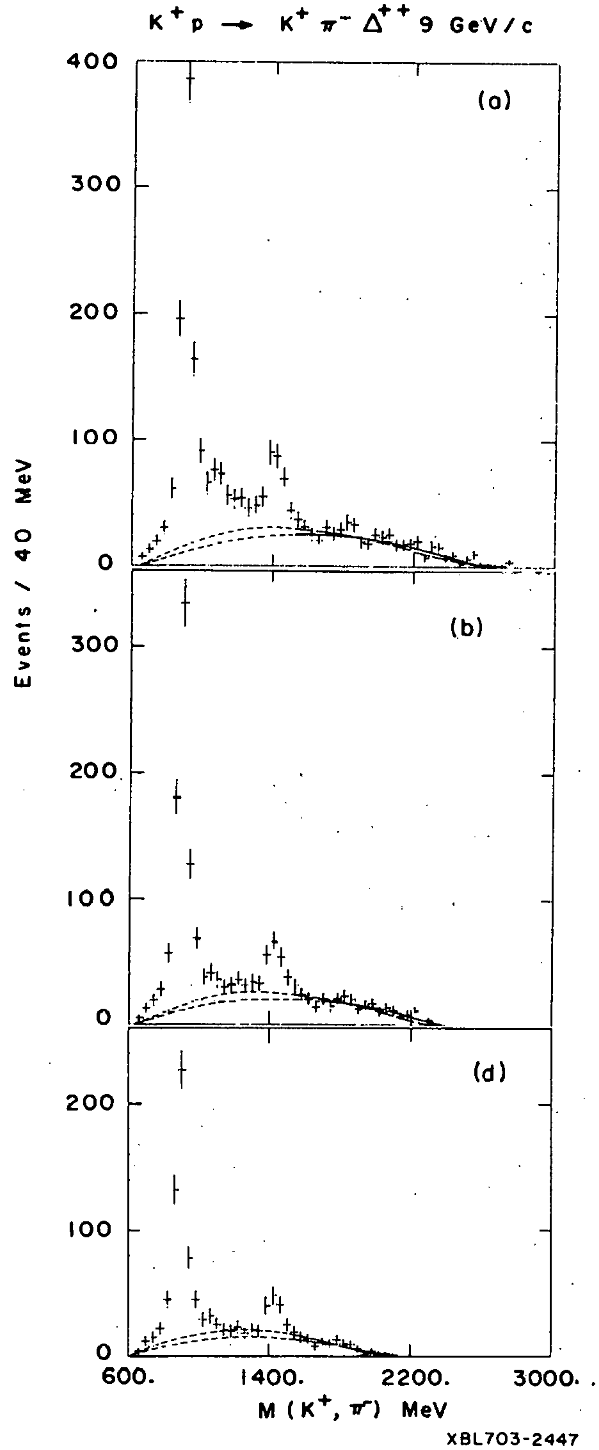

K+ p → K+ π− Δ++ 9 GeV/c
Events / 40 MeV
400
300
200
100
0
(a)
(b)
(d)
600.
1400.
2200.
3000.
M (K+, π−) MeV
XBL703-2447

Fig. 10.

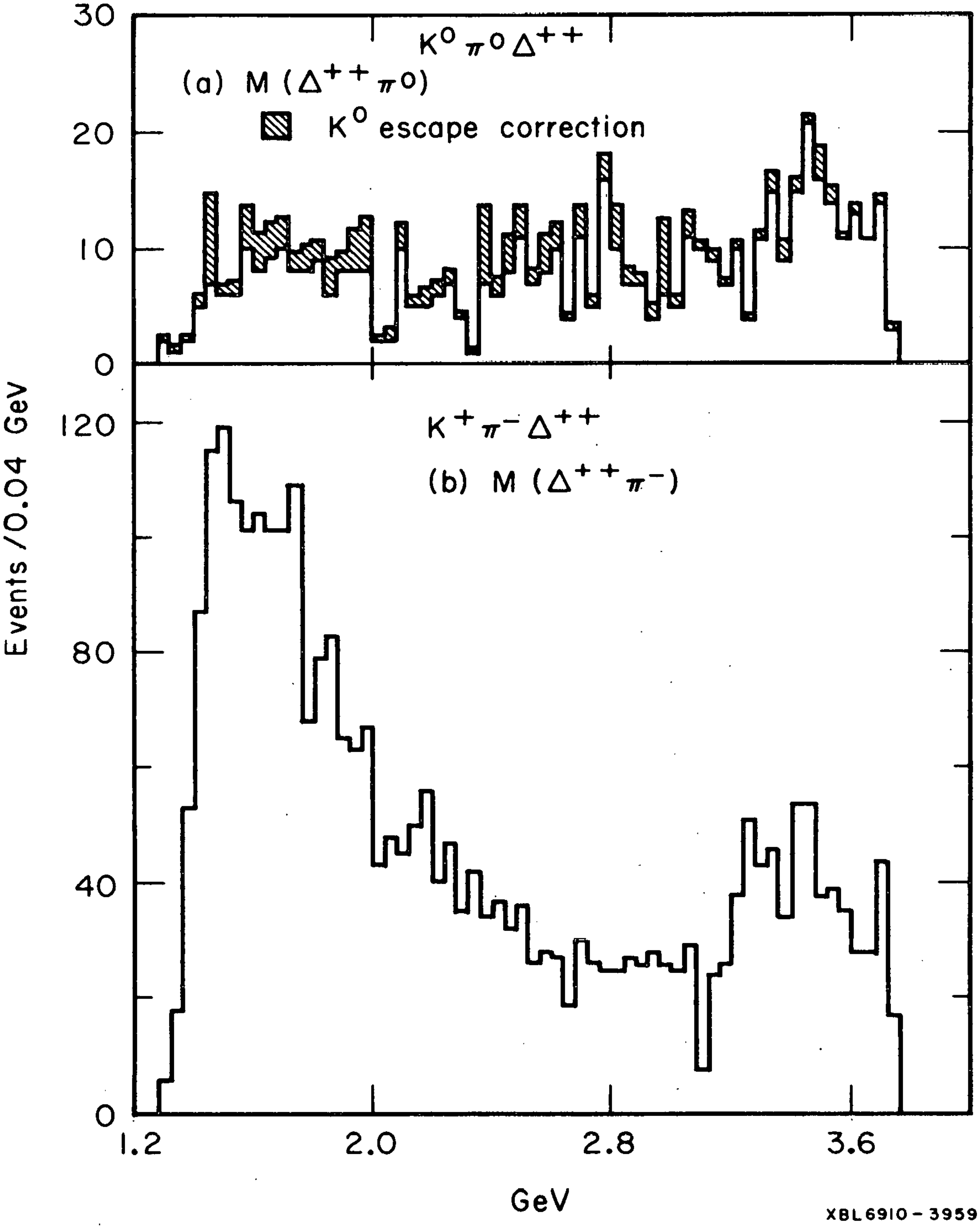

30
20
10
0
$K^0 \pi^0 \Delta^{++}$
(a) M ($\Delta^{++} \pi^0$)
K^0 escape correction
120
80
40
0
$K^+ \pi^- \Delta^{++}$
(b) M ($\Delta^{++} \pi^-$)
Events /0.04 GeV
1.2
2.0
2.8
3.6
GeV
XBL6910-3959

Fig. 11.

APPENDIX II

EXPERIMENTAL DETAILS AND THE CROSS SECTION FOR THE REACTION $K^+p \rightarrow K^+\pi^-\pi^+p$ AT 9 GeV/c

A. Experimental Details

The experiments were carried out in the Brookhaven National Laboratory 80-inch hydrogen bubble chamber exposed to a 4.6-GeV/c and a 9-GeV/c rf-separated K^+ beam at the Alternating Gradient Synchrotron (AGS). There were about 50,000 and 200,000 exposures taken for the 4.6- and 9-GeV/c experiments respectively. The events from both experiments were measured on the Lawrence Radiation Laboratory Flying-Spot Digitizer (FSD) and remeasurements were carried out on the conventional digitizing machine (Franckenstein).

1. K^+p at 4.6 GeV/c

The K^+ beam momentum was 4600±40 MeV at the entrance to the bubble chamber. A beam track was defined as one with a measured momentum within three standard deviations of 4600 MeV, i.e., $3\sqrt{(\Delta p_{meas})^2 + (\Delta p_{beam})^2}$. The Δp_{meas} was the measured error of the momentum and $\Delta p_{beam} = \pm 40$ MeV. For a beam track event, the coordinates of the main vertex (x_o, y_o, z_o) were constrained to lie inside the interaction fiducial volume:

$$- 63.8 - 0.48z_o \leqq x_o \leqq 38.55 + 0.0345z_o \text{ cm},$$

$$- 9.5 - 0.209z_o \leqq y_o \leqq 25.0 \text{ cm, and}$$

$$- 3.0 \leqq z_o \leqq 66.0 \text{ cm}.$$

The K^+ beam is approximately parallel to the x direction. For events with an associated "V", the decay vertex (x_V, y_V, z_V) is further restricted to lie within a decay fiducial volume:

$$-63.8 - 0.48z_V \leqq x_V \leqq 51.5 \text{ cm},$$
$$-25.0 \leqq y_V \leqq 25.0 \text{ cm, and}$$
$$5.0 \leqq z_V \leqq 60.0 \text{ cm}.$$

If an event failed to satisfy the above criteria it was rejected. Other sources of rejects were: frame number errors, unreadable data boxes, immeasurable tracks due to chamber distortion, film damage, etc. To accept an event, two criteria had to be satisfied: The χ^2 of the fit had to be within the 1% confidence level, and the observed ionization had to be consistent with the fitted momentum and the mass assignment for each track. The geometric reconstruction and the kinematical fitting of the events were performed through the program PACKAGE. To analyze the accepted events, the program CHAOS was used at various stages: calculating the kinematical variables interested, selecting events under particular kinematic criteria, and making histograms and scatter plots, etc.

2. K^+p at 9 GeV/c

The 9-GeV/c experiment consists of two runs with about 100,000 exposures for each. The K^+ beam momentum at the entrance to the chamber was 9000±65 MeV for the first run and 8950±65 MeV for the second run. A beam track was defined as one with a measured momentum within three standard deviations of 9000 and 8950 McV respectively for the two runs. The interaction fiducial volume was defined as

$$-100.0 \leqq x_o \leqq 100.0 \text{ cm},$$
$$-40.0 \leqq y_o \leqq 40.0 \text{ cm, and}$$
$$-3.0 \leqq z_o \leqq 66.0 \text{ cm}.$$

For these events with a "V", a decay fiducial volume was defined for the decay vertex (x_V, y_V, z_V) as

$$- 90.0 \leq x_o \leq 50.0 \text{ cm},$$
$$- 23.0 \leq y_o \leq 23.0 \text{ cm, and}$$
$$0.0 \leq z_o \leq 50.0 \text{ cm}.$$

The reject and acceptance criteria for the events were the same as those described in the preceding section for the 4.6-GeV/c experiment. The geometric reconstruction and the kinematical fitting of the events were performed through SIOUX and the data analysis by CHAOS.

B. The Cross Section for the Reaction $K^+p \rightarrow K^+\pi^-\pi^+p$ at 9 GeV/c

Normalizing to the K^+p total cross section, the cross section for the reaction

$$K^+p \rightarrow K^+\pi^-\pi^+p \quad \text{at } 9 \text{ GeV/c} \tag{II-1}$$

can be written as

$$\sigma = \sigma_T \frac{N}{N_T} , \tag{II-2}$$

where σ_T is the K^+p total cross section at 9 GeV/c, and N_T and N are the total number of events and the number of events fitted as $K^+\pi^-\pi^+p$ final state in an unbiased sample. To determine the cross section of the reaction (II-1), we rescanned three rolls of film and fitted those four-prong and four-prong-with-a-"V" events. Comparing the events from the rescan with the results of the first scan and the old measurements, we found 2211 events in gross total, of which 182 events were newly found and 120 events were found with a possible wrong event type assignment in the old (the first and the second) measurements. The latter included all the four-prong and four-prong-with-a-"V" events that were not fitted and some six-prong and two-prong events that might be assigned wrong. The results of the three measurements are summarized in the following table.

Results of the measurements for the events of event type 40.[a]

	$K^+\pi^-\pi^+p$ 4C-fits	1C-fits and MM events	Accepted events	Failed in geometrical reconstruction
1st measurement (FSD)	54	375	429	264
2nd measurement (FSD)	20	49	69	203
3rd measurement (Franckenstein)	26	138	164	74
Results after three measurements	100	562	662	74

[a]Event type 40 refers to four-prong events with no sudden change of curvature of any track.

After the third measurement we found that among the 40's there are 17 rejects and 23 events that do not fit as $K^+\pi^-\pi^+p$ 4C-fits or 1C-fits but have a missing mass less than 300 MeV. There were 21 events of the latter category after the second FSD measurement. But from the third (Franckenstein) measurement, 10 of them remain in the same category, another 10 of them either are fitted as 1C-fits or have a missing mass greater than 300 MeV, and one of them is fitted as the $K^+\pi^-\pi^+p$ final state.

Events from other topologies, e.g., 4-prong-with-a-"V" and 4-prong with one of the tracks decaying, may also fit as the $K^+\pi^-\pi^+p$ final state because of wrong assignment of V or that K^+ or $\pi^{\pm}$ decay. There were 120 events of this category remeasured in the third (Franckenstein) measurement; 4 of them were fitted as the $K^+\pi^-\pi^+p$ final state, 14 of them failed the geometrical reconstruction, and 102 of them were fitted as final states other than the $K^+\pi^-\pi^+p$ final state.

Based on the above information we found the cross section in the following steps:

1) There were 100 + 562 + 23 + 74 + 17 = 776 "4O's" of which 100 events were $K^+\pi^-\pi^+p$ 4C-fits, 17 events were rejects, and 23 + 74 = 97 events were unresolved.

2) We assumed that rejects were independent of topology. Based on the reject rate of 4O's, we corrected the total number as

$$N_T = 2211 - 2211 \times \frac{17}{776} \approx 2162.6 \quad . \tag{II-3}$$

3) The number of $K^+\pi^-\pi^+p$ 4C-fits was equal to

$$N = \underbrace{100 + 74 \times \frac{100}{662} + 23 \times \frac{1}{21}}_{\text{contribution from 4O's}} + \underbrace{4 + 14 \times \frac{4}{102}}_{\text{contribution from non-4O's}} \approx 116.8 \quad . \tag{II-4}$$

4) We assumed that the errors in N and N_T were purely statistical. Based on $N_T = 2162.6 \pm 46.4$, $N = 116.8 \pm 10.8$, and $\sigma_T = 17.3 \pm 0.2$ mb, we found that the cross section for the reaction $K^+p \to K^+\pi^-\pi^+p$ at 9 GeV/c was

$$\sigma = 0.94 \pm 0.18 \text{ mb} \quad . \tag{II-5}$$

The K^+p total cross section at 9 GeV/c, σ, was estimated from the existing data points between 8 GeV/c and 10 GeV/c in Ref. 13.

Based on a total of 7555 events of the $K^+\pi^-\pi^+p$ final state in the whole experiment, one finds that this cross section corresponds to approximately 8 events/μb.

The error of the cross section given in (II-5) is quite large because both N and N_T are small numbers and their statistical error is large. An alternative method for reducing the error of the cross section is to use the information available in a larger sample and assume that the correction made in (II-3) and (II-4) is true even for the larger sample.

Consider an unbiased sample and let N_T' and N_T be the total number of events before and after the correction, N_{40}' and N_{40} be the number of 40's before and after the correction, and N' and N be the number of the $K^+\pi^-\pi^+p$ 4C-fits before and after the correction. Write

$$N_T = N_T'(1 + C_T) \quad \text{and} \quad N = N'(1 + C) \quad . \tag{II-6}$$

From (II-3) and (II-4) we obtain

$$C_T = -\frac{17}{776} \tag{II-7a}$$

$$\begin{aligned} C &= \frac{74}{662} + \frac{1}{N'}\left(\frac{23}{21} + 4 + 14 \times \frac{4}{102}\right) \cong \frac{74}{662} + \frac{5.65}{N'} \\ &= \frac{74}{662} + \frac{5.65}{100} \quad . \end{aligned} \tag{II-7b}$$

The last step of Eq. (II-7b) was to replace N' by 100, since 5.65 events is the correction for $N' = 100$. By treating the numerator and denominator of each fraction in Eq. (II-7) as independent numbers and considering the statistical error in each independent number, we obtain the error in C and C_T, namely $\overline{\Delta C} = 0.137$ and $\overline{\Delta C_T} = 0.005$. Re-express Eq. (II-1) as

$$\sigma = \sigma_T \frac{N'(1 + C)}{N_T'(1 + C_T)} = \left(\frac{N'}{N_{40}'}\right)\left(\frac{N_{40}'}{N_T'}\right) \sigma_T \frac{(1 + C)}{(1 + C_T)} \quad . \tag{II-8}$$

From a large unbiased sample, we found that $N_{40}' = 33891$ and $N' = 3690$. Substitute these numbers in the first factor in Eq. (II-8) and use $N_{40}' = 776$ and $N_T' = 2211$ (found in the three rolls rescanned) in the second factor in (II-8). We obtain

$$\sigma = \left(\frac{3690}{33891}\right) \times \left(\frac{776}{2211}\right) \times 17.3 \times \frac{\left(1 - \frac{17}{776}\right)}{\left(1 + \frac{74}{662} + \frac{5.65}{100}\right)} = 0.79 \text{ mb} \quad .$$

Neglect the error introduced by $\left(\frac{N'}{N_{40}'}\right)_{\text{large sample}} \times \left(\frac{N_{40}'}{N_T'}\right)_{\text{3 rolls rescanned}}$ and consider the error introduced by σ_T, C, and C_T only; we obtain $\overline{\Delta\sigma} = 0.09$ mb. Therefore the cross section for the $K^+\pi^-\pi^+p$ channel at 9 GeV/c is

$$\sigma = 0.79 \pm 0.09 \text{ mb} \quad . \tag{II-9}$$

Comparing this result with what we obtained earlier (based on three rolls of film), we found that the values of the cross section, σ, in the two cases are comparable and within errors they are consistent. The new error given in Eq. (II-9) has been reduced by a factor of 2 as compared with the old result [Eq. (II-5)].

For a total of 7555 $K^+\pi^-\pi^+p$ 4C-fits we found that the cross section given in Eq. (II-9) corresponds to approximately 9.6 events/μb.

We adopt the value given in (II-9) as the cross section for the reaction $K^+p \rightarrow K^+\pi^-\pi^+p$ at 9 GeV/c.

REFERENCES

1. A major part of this thesis was discussed in two earlier reports:

(a) C. Fu, A. Firestone, G. Goldhaber, and G. H. Trilling, Nucl. Phys. B18, 93 (1970), and

(b) C. Fu, Lawrence Radiation Laboratory Report UCRL-19807 (1970) (to be published in Physical Review).

2. Data on the hadron-hadron collisions leading to the four-body final states appear too frequently in the literature; it would be impossible for the author to list all the relevant references here. For the general experimental information on the recent developments in particle physics the following articles will be very useful:

(a) N. Barash-Schmidt, A. Barbaro-Galtieri, C. Bricman, S. E. Derenzo, L. R. Price, A. Rittenberg, M. Roos, A. H. Rosenfeld, P. Söding, and C. G. Wohl, Review of Particle Properties, Rev. Mod. Phys. 42, 87 (1970).

(b) Rapporteur talks in the Proceedings of the Lund International Conference on Elementary Particles (1969) given by:

(i) L. DiLella on "Pion Reactions,"

(ii) E. Lillethun on "Nucleon Reactions,"

(iii) L. Montanet on "Antiproton Reactions,"

(iv) D. R. O. Morrison on "Kaon Reactions,"

(v) B. Maglić on "Meson Resonances,"

(vi) R. Plano on "Baryon Non-Strange Resonances," and

(vii) R. Levi-Setti on "Baryon Strange Resonances,"

and the references therein, and also the Rapporteur talks in the proceedings of earlier international conferences.

(c) F. Loeffler and E. Malamud, in Proceedings of the Conference on $\pi\pi$ and $K\pi$ Interactions (May 1969, at Argonne National Laboratory).

(d) G. Goldhaber and S. Goldhaber, Recent Developments in Boson Resonances, in Advances in Particle Physics, edited by R. L. Cool and R. E. Marshak (Interscience, New York, 1968).

3. Here we refer the low enhancements to Q observed in the $(K^*\pi)^+$ or $(K\rho)^+$ mass spectrum, A_1 in the $(\rho\pi)^+$ mass spectrum, and the $\Delta^{++}\pi$ mass enhancement in the $\Delta^{++}\pi^-$ mass spectrum. The widths of the Q and the $\Delta^{++}\pi^-$ mass enhancement are about 0.35 GeV and that of A_1 is on the order of 0.1 GeV. References on these objects are listed below:

(a) Both Q and A_1 have been controversial subjects of discussion. The developments of the early studies and a detailed comparison of A_1 and Q was given by G. Goldhaber and S. Goldhaber, in Symposia on Theoretical Physics and Mathematics, Vol. 6 (Plenum Press, New York, 1968); for more recent data see Refs. 3.

(b) The discussions of the Q-bump from data of K^+p at 4.6 GeV/c and 9 GeV/c were published earlier:

(i) B. C. Shen, I. Butterworth, C. Fu, G. Goldhaber, S. Goldhaber, and G. H. Trilling, Phys. Rev. 17, 726 (1966).

(ii) G. Goldhaber, A. Firestone, and B. C. Shen, Phys. Rev. Letters 19, 972 (1967).

(iii) G. Alexander, A. Firestone, G. Goldhaber, and D. Lissauer, Nucl. Phys. B13, 503 (1969).

(c) A. Firestone, The Q Region of $K\pi\pi$ Mass, talk presented at the 1970 Conference on Meson Spectroscopy, Philadelphia, UCRL-19846.

(d) The experimental evidence of the low $\Delta^{++}\pi^-$ mass enhancement was presented as early as 1964 by 1) G. Goldhaber, Multipion and Baryon Resonances in the π^+p Reaction, and 2) S. Goldhaber, A Comparison of Resonance Formation in π^-p and π^+p Reactions, in Proceedings of the

Conference on Particle and High Energy Physics at Boulder, Colorado, July 1964. A recent discussion on this subject was given by J. G. Rushbrooke, Nucleon Resonances in Production Processes, in Proceedings of the XIVth International Conference on High-Energy Physics, Vienna, 1968.

(e) Early results on the study of the low $\Delta^{++}\pi^{-}$ mass enhancement in the reaction $K^{+}p \rightarrow K^{+}\pi^{-}\Delta^{++}_{1236}$ at 4.6 and 9 GeV/c was given by C. Fu, A. Firestone, G. Goldhaber, G. H. Trilling, and B. C. Shen: Contribution to the Informal Meeting on Experimental Meson Spectroscopy, Philadelphia, April 1968, Lawrence Radiation Laboratory Report UCRL-18201.

4. K. Gottfried and J. D. Jackson, Nuovo Cimento 33, 309 (1964).

5. (a) Chih-Yung Chien, The L and A_3 Regions of $K\pi\pi$ and 3π Masses, Invited Talk at the Second Conference on Meson Spectroscopy, Philadelphia, May 1, 1970, Johns Hopkins University Report JHU-7010.

(b) A. Barbaro-Galtieri, P. J. Davis, S. M. Flatté, J. H. Friedman, M. A. Garnjost, G. R. Lynch, M. J. Matison, M. S. Rabin, F. T. Solmitz, N. M. Uyeda, V. Waluch, R. Windmolders, and J. J. Murray, Phys. Rev. Letters 22, 1207 (1969) and the references therein.

6. J. P. Ader, M. Capdeville, G. Cohen-Tannoudji, and Ph. Salin, Nuovo Cimento 56A, 952 (1968) and the references therein.

7. S. M. Flatté, invited talk on "12 GeV/c $K^{+}p$ Interactions," American Physical Society Meeting, New York, March 1969.

8. T. G. Trippe, C.-Y. Chien, E. Malamud, J. Mellema, P. E. Schlein, W. E. Slater, D. H. Stork, and H. K. Ticho, Phys. Letters 28B, 203 (1968).

9. P. Antich, A. Callahan, R. Carson, B. Cox, D. Denegri, L. Ettlinger, D. Gillespie, G. Goodman, G. Luste, R. Mercer, A. Pevsner, and R. Zdanis, Phys. Rev. Letters 21, 842 (1968).

10. (a) W. P. Dodd, T. Joldersma, R. B. Palmer and N. P. Samios, Phys. Rev. 177, 1991 (1969);

(b) David J. Crennell, Uri Karshon, Kwan Wu Lai, John S. O'Neall, and J. Michael Scarr, Phys. Rev. Letters 22, 487 (1969);

(c) W. de Baere, J. Debaisieux, P. Dufour, F. Grard, J. Heughebaert, L. Pape, P. Peeters, F. Verbeure, R. Windmolders, Y. Goldschmidt-Clermont, V. P. Henri, B. Jongejans, A. Moiseev, F. Muller, J. M. Perreau, A. Prokes, and V. Yarba, Nuovo Cimento 51A, 401 (1967).

11. From Ref. 3a we find that $M_{K^{*\pm}} = 892.1\pm0.4$, $\Gamma_{K^*} = 50.1\pm0.8$, and $M_{K^{*o}} - M_{K^{*\pm}} = 7\pm3$ MeV.

12. See suggestion given at the end of the conclusions of this section.

13. L. R. Price, N. Barash-Schmidt, O. Benary, R. W. Bland, A. H. Rosenfeld, and C. G. Wohl, A Compilation of K^+N Interactions, Lawrence Radiation Laboratory Report UCRL-20000 K^+N, September 1969.

FIGURE CAPTIONS

Fig. 1. (a) The exchange diagram for the reaction $K^+p \to K^+\pi^-\Delta^{++}_{1236}$.

(b) The Gottfried-Jackson frame for the $K^+\pi^-$ system.

Fig. 2. Triangle plot, $M(K^+\pi^-)$ vs $M(p\pi^+)$, for the 9-GeV/c data.

Fig. 3. (a) $M(K^+\pi^-)$ and (b) $M(p\pi^+)$ projections of Fig. 2.

Fig. 4. Triangle plot, $M(K^+\pi^-)$ vs $M(p\pi^+)$, for the 4.6-GeV/c data.

Fig. 5. (a) $M(K^+\pi^-)$ and (b) $M(p\pi^+)$ projections of Fig. 4.

Fig. 6. Dalitz plots for the $K^+\pi^-\Delta^{++}$ channel at 9 GeV/c with (a) no $|t'|$ cut and (b) $|t'| < 0.1\ (\mathrm{GeV}/c)^2$.

Fig. 7. (a) $M(K^+\pi^-)$ and (b) $M(\Delta^{++}\pi^-)$ spectra for the $K^+\pi^-\Delta^{++}$ channel at 9 GeV/c.

Fig. 8. Dalitz plots for the $K^+\pi^-\Delta^{++}$ channel at 4.6 GeV/c with (a) no $|t'|$ cut and (b) $|t'| < 0.3\ (\mathrm{GeV}/c)^2$.

Fig. 9. (a) $M(K^+\pi^-)$ and (b) $M(\Delta^{++}\pi^-)$ spectra for the $K^+\pi^-\Delta^{++}$ channel at 4.6 GeV/c.

Fig. 10. $M(K^+\pi^-)$ vs (a) $\rho_{3,3}$, (b) Re $\rho_{3,1}$, and (c) Re $\rho_{3,-1}$ for the Δ^{++}_{1236} in the $K^+\pi^-\Delta^{++}_{1236}$ channel at 9 GeV/c.

Fig. 11. $M(K^+\pi^-)$ vs (a) $\rho_{3,3}$, (b) Re $\rho_{3,1}$, and (c) Re $\rho_{3,-1}$ for the Δ^{++}_{1236} in the $K^+\pi^-\Delta^{++}_{1236}$ channel at 4.6 GeV/c.

Fig. 12. Dalitz plots for the $K^{*0}_{890}\pi^+p$ channel at 9 GeV/c with (a) no $|t'|$ cut and (b) $|t'| < 0.3\ (\mathrm{GeV}/c)^2$.

Fig. 13. (a) $M(p\pi^+)$ and (b) $M(K^{*0}_{890}\pi^+)$ spectra for the $K^{*0}_{890}\pi^+p$ channel at 9 GeV/c.

Fig. 14. Dalitz plots for the $K^{*0}_{890}\pi^+p$ channel at 4.6 GeV/c with (a) no $|t'|$ cut and (b) $|t'| < 0.3\ (\mathrm{GeV}/c)^2$.

Fig. 15. (a) $M(p\pi^+)$ and (b) $M(K^{*0}_{890}\pi^+)$ spectra for the $K^{*0}_{890}\pi^+p$ channel at 4.6 GeV/c.

Fig. 16. $M(p\pi^+)$ vs (a) $\rho_{0,0}$, (b) Re $\rho_{1,0}$, and (c) $\rho_{1,-1}$ for the K^{*0}_{890} in the $K^{*0}_{890}\pi^+p$ channel at 9 GeV/c.

Fig. 17. $M(p\pi^+)$ vs (a) $\rho_{0,0}$, (b) Re $\rho_{1,0}$, and (c) $\rho_{1,-1}$ for the K^{*0}_{890} in the $K^{*0}_{890}\pi^+p$ channel at 4.6 GeV/c.

Fig. 18. Dalitz plots for the $K^{*0}_{1420}\pi^+p$ channel at 9 GeV/c with (a) no $|t'|$ cut and (b) $|t'| \leq 0.3$ $(\text{GeV/c})^2$.

Fig. 19. (a) $M(p\pi^+)$ and (b) $M(K^{*0}_{1420}\pi^+)$ mass spectra for the $K^{*0}_{1420}\pi^+p$ channel at 9 GeV/c.

Fig. 20. Dalitz plots for the $K^{*0}_{1420}\pi^+p$ channel at 4.6 GeV/c with (a) no $|t'|$ cut and (b) $|t'| \leq 0.3$ $(\text{GeV/c})^2$.

Fig. 21. (a) $M(p\pi^+)$ and (b) $M(K^{*0}_{1420}\pi^+)$ mass spectra for the $K^{*0}_{1420}\pi^+p$ channel at 4.6 GeV/c.

Fig. 22. (a) A double-Regge-pole-exchange diagram associated with the low $\Delta^{++}\pi^-$ enhancement (for the $K^+\pi^-\Delta^{++}$ channel). (b) A single-exchange diagram for K^* resonance productions (for the $K^+\pi^-\Delta^{++}$ channel).

Fig. 23. $|t'|$ distributions for the events in the K^{*0}_{890} region in the $K^{*0}_{890}\Delta^{++}_{1236}$ channel at 9 GeV/c. (a) All events in the K^{*0}_{890} region, (b) $\cos\theta(K^+\pi^-) < -0.5$, (c) $\cos\theta(K^+\pi^-) \geq 0.5$, and (d) $-0.5 \leq \cos\theta(K^+\pi^-) < 0.5$.

Fig. 24. $|t'|$ distributions for the events in the K^{*0}_{890} region in the $K^{*0}_{890}\Delta^{++}_{1236}$ channel at 4.6 GeV/c. (a) All events in the K^{*0}_{890} region, (b) $\cos\theta(K^+\pi^-) < -0.5$, and (c) $\cos\theta(K^+\pi^-) \geq 0.5$.

Fig. 25. $\cos\theta(K^+\pi^-)$ vs $\varphi(K^+\pi^-)$ decay angular correlation plots for the events in the $K^{*0}_{890}\Delta^{++}_{1236}$ channel at 9 GeV/c with (a) $|t'| < 0.1$ $(\text{GeV/c})^2$ and $|t'| > 0.1$ $(\text{GeV/c})^2$.

Fig. 26. (a) $\cos\theta(K^+\pi^-)$ and (b) $\varphi(K^+\pi^-)$ projections of Fig. 25a, and (c) $\cos\theta(K^+\pi^-)$ and (d) $\varphi(K^+\pi^-)$ projections of Fig. 25b.

Fig. 27. cos $\theta(K^+\pi^-)$ vs $\varphi(K^+\pi^-)$ decay angular correlation plots for the events in the $K^{*0}_{890}\Delta^{++}_{1236}$ channel at 4.6 GeV/c with (a) $|t'| < 0.07$ $(\mathrm{GeV/c})^2$ and (b) $|t'| > 0.07$ $(\mathrm{GeV/c})^2$.

Fig. 28. (a) cos $\theta(K^+\pi^-)$ and (b) $\varphi(K^+\pi^-)$ projections of Fig. 27a, and (c) cos $\theta(K^+\pi^-)$ and (d) $\varphi(K^+\pi^-)$ projections of Fig. 27b.

Fig. 29. Spin density matrix elements (a) $\rho_{0,0}$, (b) $\rho_{1,-1}$, and (c) Re $\rho_{1,0}$ for the K^{*0}_{890} as a function of $|t'|$ in the $K^{*0}_{890}\Delta^{++}_{1236}$ channel at 9 GeV/c.

Fig. 30. The $\sigma^{\pm}_{1}$ for the K^{*0}_{890} as a function $|t'|$ in the $K^{*0}_{890}\Delta^{++}_{1236}$ channel at 9 GeV/c.

Fig. 31. Spin density matrix elements (a) $\rho_{0,0}$, (b) Re $\rho_{1,0}$, and (c) $\rho_{1,-1}$ for the K^{*0}_{890} as a function of $|t'|$ in the $K^{*0}_{890}\Delta^{++}_{1236}$ channel at 4.6 GeV/c.

Fig. 32. (a) $2\sigma^{+}_{1}$ and (b) $2\sigma^{-}_{1}$ for the K^{*0}_{890} as a function $|t'|$ in the $K^{*0}_{890}\Delta^{++}_{1236}$ channel at 4.6 GeV/c.

Fig. 33. The coefficients of the expansion $\Sigma\, a_n \cos \theta^n(K^+\pi^-)$ for the events in the K^{*0}_{890} region for the 9-GeV/c data with cos $\theta(K^+\pi^-) < 0.5$; (a) a_o, (b) a_1, and (c) a_2.

Fig. 34. The coefficients of the expansion $\Sigma\, a_n \cos \theta^n(K^+\pi^-)$ for the events in the K^{*0}_{890} region for the 4.6-GeV/c data with no cut in cos $\theta(K^+\pi^-)$; (a) a_o, (b) a_1, and (c) a_2.

Fig. 35. Spin density matrix elements (a) $\rho_{3,3}$, (b) Re $\rho_{3,1}$, and (c) Re $\rho_{3,-1}$ for the $K^{*0}_{890}\Delta^{++}_{1236}$ events from the 9-GeV/c data as a function of $|t'|$.

Fig. 36. Spin density matrix elements (a) $\rho_{3,3}$, (b) Re $\rho_{3,1}$, and (c) Re $\rho_{3,-1}$ for the $K^{*0}_{890}\Delta^{++}_{1236}$ events from the 4.6-GeV/c data as a function of $|t'|$.

Fig. 37. The $|t'|$ distributions for the events in the $K^{*}_{1420}\Delta^{++}_{1236}$ channel from (a) the 9-GeV/c and (b) the 4.6-GeV/c data.

Fig. 38. The cos $\theta(K^+\pi^-)$ vs $\varphi(K^+\pi^-)$ decay angular correlation plots for the events in the $K^{*0}_{1420}\Delta^{++}_{1236}$ channel at 9 GeV/c with (a) $|t'| < 0.1$ $(\mathrm{GeV/c})^2$ and (b) $|t'| > 0.1$ $(\mathrm{GeV/c})^2$.

Fig. 39. The cos $\theta(K^+\pi^-)$ vs $\varphi(K^+\pi^-)$ decay angular correlation plots for the events in the $K^{*0}_{1420}\Delta^{++}_{1236}$ channel at 4.6 GeV/c with (a) $|t'| < 0.07$ $(\mathrm{GeV/c})^2$ and (b) $|t'| > 0.07$ $(\mathrm{GeV/c})^2$.

Fig. 40. (a) The cos $\theta(K^+\pi^-)$ and (b) the $\varphi(K^+\pi^-)$ projections of Fig. 38a and (c) the cos $\theta(K^+\pi^-)$ and (d) the $\varphi(K^+\pi^-)$ projections of Fig. 38b. The curve shown in Fig. 40a is a fit to the Legendre polynomial $\sum_{\ell=0}^{4} a_\ell P_\ell(\cos\theta(K^+\pi^-))$.

Fig. 41. (a) The cos $\theta(K^+\pi^-)$ and (b) the $\varphi(K^+\pi^-)$ projections of Fig. 39a, and (c) the cos $\theta(K^+\pi^-)$ and (d) the $\varphi(K^+\pi^-)$ projections of Fig. 39b.

Fig. 42. The cos $\theta(K^+\pi^-)$ distribution for all the events in the $K^{*0}_{1420}\Delta^{++}_{1236}$ channel at 4.6 GeV/c.

Fig. 43. Spin density matrix elements for the Δ^{++}_{1236} in the $K^{*0}_{1420}\Delta^{++}_{1236}$ channel at 9 GeV/c; (a) $\rho_{3,3}$, (b) Re $\rho_{3,1}$, and (c) Re $\rho_{3,-1}$.

Fig. 44. Spin density matrix elements for the Δ^{++}_{1236} in the $K^{*0}_{1420}\Delta^{++}_{1236}$ channel at 4.6 GeV/c; (a) $\rho_{3,3}$, (b) Re $\rho_{3,1}$, and (c) Re $\rho_{3,-1}$.

Fig. 45. $M(p\pi^+)$ vs cos $\theta(p\pi^+)$ for the events in (a) the K^{*0}_{890} and (b) the K^{*0}_{1420} regions from the 9-GeV/c data.

Fig. 46. $M(p\pi^+)$ vs cos $\theta(p\pi^+)$ for the events in (a) the K^{*0}_{890} and (b) the K^{*0}_{1420} regions from the 4.6-GeV/c data.

Fig. 47. $M(K^+\pi^-)$ vs the forward-backward asymmetry (F-B)/(F+B) plot for the $K^+\pi^-$ system in the $K^+\pi^-\Delta^{++}$ channel at 9 GeV/c.

Fig. 48. The $|t'|$ distributions for the events in the $K^+\pi^-\Delta^{++}$ channel at 9 GeV/c with the criteria (a) all events with $M(K^+\pi^-) < 1.54$ GeV, (b) cos $\theta(K^+\pi^-) < 0.5$ and $M(K^+\pi^-) < 1.54$ GeV, (c) cos $\theta(K^+\pi^-) \geq 0.5$ and $M(K^+\pi^-) < 1.54$ GeV, and (d) cos $\theta(K^+\pi^-) \geq 0.5$ and $M(K^+\pi^-) \geq 1.54$ GeV. Actually most of the events with $M(K^+\pi^-) > 1.54$ GeV are in the forward cos $\theta(K^+\pi^-)$ region. (e) The same $|t'|$ distribution as Fig. 48a with a large scale.

Fig. 49. The $|t'|$ distributions for the events in the $K^+\pi^-\Delta^{++}$ channel at 4.6 GeV/c with the criteria (a) all the events, (b) $\cos\theta(K^+\pi^-) < 0.5$, and (c) $\cos\theta(K^+\pi^-) \geqq 0.5$.

Fig. 50. $M(K^+\pi^-)$ vs $\cos\theta(K^+\pi^-)$ plots for the events in the $K^+\pi^-\Delta^{++}$ channel at 9 GeV/c with (a) $|t'| < 0.1$ $(GeV/c)^2$ and (b) $|t'| \geqq 0.1$

Fig. 51. $M(K^+\pi^-)$ vs $\varphi(K^+\pi^-)$ plots for the events in the $K^+\pi^-\Delta^{++}$ channel at 9 GeV/c with (a) $|t'| < 0.1$ $(GeV/c)^2$ and (b) $|t'| \geqq 0.1$ $(GeV/c)^2$.

Fig. 52. $M(K^+\pi^-)$ vs $\cos\theta(K^+\pi^-)$ plots for the events in the $K^+\pi^-\Delta^{++}$ channel at 4.6 GeV/c with (a) $|t'| < 0.07$ $(GeV/c)^2$ and (b) $|t'| \geqq 0.07$ $(GeV/c)^2$.

Fig. 53. $M(K^+\pi^-)$ vs $\varphi(K^+\pi^-)$ plots for the events in the $K^+\pi^-\Delta^{++}$ channel at 4.6 GeV/c with (a) $|t'| < 0.07$ $(GeV/c)^2$ and (b) $|t'| \geqq 0.07$ $(GeV/c)^2$.

Fig. 54. $M(K^+\pi^-)$ vs $\langle Y_L^0\rangle$ and Re $\langle Y_L^1\rangle$ for the $K^+\pi^-$ system in the $K^+\pi^-\Delta^{++}$ channel at 9 GeV/c with $|t'| < 0.1$ $(GeV/c)^2$ and with (a) L = 1, (b) L = 2, (c) L = 3, (d) L = 4, (e) L = 5, and (f) L = 6.

Fig. 55. $M(K^+\pi^-)$ vs $\langle Y_L^0\rangle$ and Re $\langle Y_L^1\rangle$ for the $K^+\pi^-$ system in the $K^+\pi^-\Delta^{++}$ channel at 4.6 GeV/c with $|t'| < 0.3$ $(GeV/c)^2$ and with (a) L = 1, (b) L = 2, (c) L = 3, (d) L = 4, (e) L = 5, and (f) L = 6.

Fig. 56. The $K^+\pi^-$ mass distributions for the $K^+\pi^-\Delta^{++}$ channel at 9 GeV/c with $|t'| < 0.1$ $(GeV/c)^2$ and (a) $\cos\theta(K^+\pi^-) \geqq 0.85$, (b) $0 \leqq \cos\theta(K^+\pi^-) < 0.85$, and (c) $\cos\theta(K^+\pi^-) \geqq 0$.

Fig. 57. The $K^+\pi^-$ mass distributions for the $K^+\pi^-\Delta^{++}$ channel at 4.6 GeV/c with $|t'| < 0.07$ $(GeV/c)^2$ and (a) $\cos\theta(K^+\pi^-) \geqq 0.85$, (b) $0 \leqq \cos\theta(K^+\pi^-) < 0.85$, and (c) $\cos\theta(K^+\pi^-) \geqq 0$.

Fig. 58. Superpositions of the corresponding $K^+\pi^-$ mass distributions of Figs. 56 and 57, namely, (a) Figs. 56a and 57a, (b) Figs. 56b and 57b, and (c) Figs. 56c and 57c.

Fig. 59. The $K^+\pi^-$ mass distributions for the events in the $K^+\pi^-\Delta^{++}$ channel at 9 GeV/c with the cuts (a) no $|t'|$ cut, (b) $|t'| < 0.1$ $(\text{GeV/c})^2$ and (c) $|t'| \geqq 0.1$ $(\text{GeV/c})^2$. The shaded portion of the histogram corresponds to the events in the $|t'|$ region with $\cos\theta(K^+\pi^-) < 0.5$.

Fig. 60. The $K^+\pi^-$ mass distribution for the events in the $K^+\pi^-\Delta^{++}$ channel at 9 GeV/c with $|t'| \geqq 0.05$ $(\text{GeV/c})^2$ and $\cos\theta(K^+\pi^-) < 0$.

Fig. 61. The $K^+\pi^-$ mass distributions for the events in the $K^+\pi^-\Delta^{++}$ channel at 4.6 GeV/c with the cuts (a) no $|t'|$ cut, (b) $|t'| < 0.07$ $(\text{GeV/c})^2$, and (c) $|t'| \geqq 0.07$ $(\text{GeV/c})^2$.

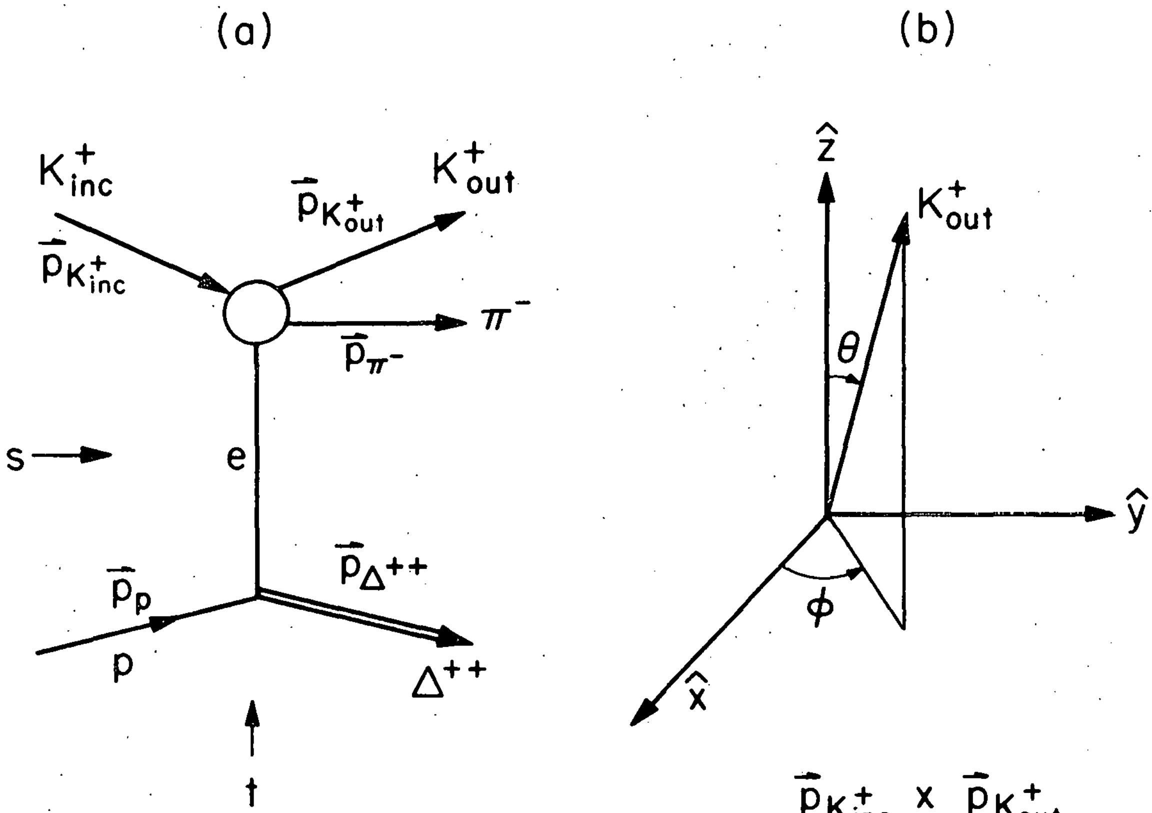

$$\hat{y} = \hat{n}_{prod} = \frac{\vec{p}_{K^+_{inc}} \times \vec{p}_{K^+_{out}}}{\left|\vec{p}_{K^+_{inc}} \times \vec{p}_{K^+_{out}}\right|}$$

$$\hat{z} = \hat{p}_{K^+_{inc}}$$

$$\hat{x} = \hat{y} \times \hat{z}$$

XBL708-3570

Fig. 1

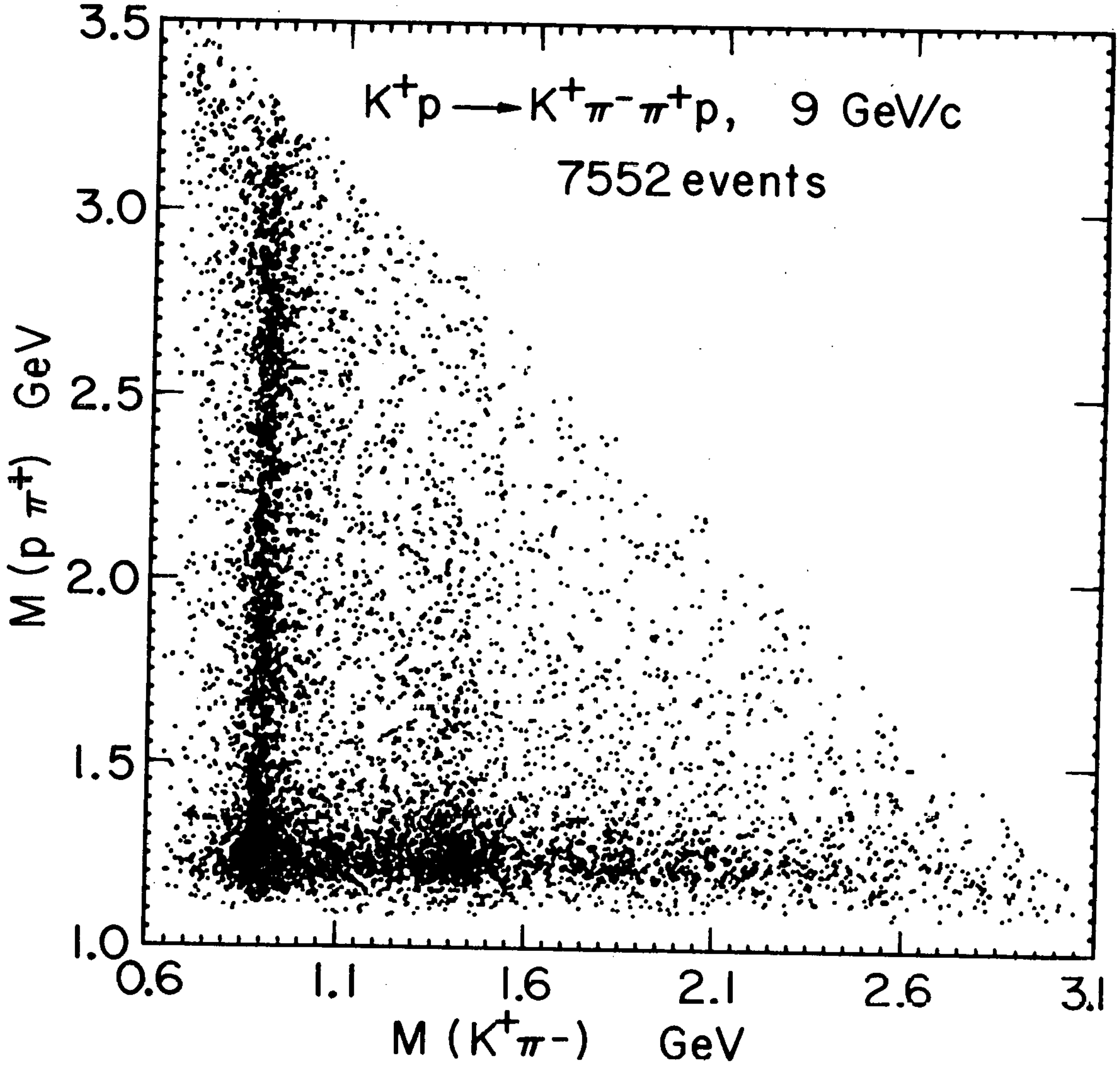

XBL696-3049

Fig. 2

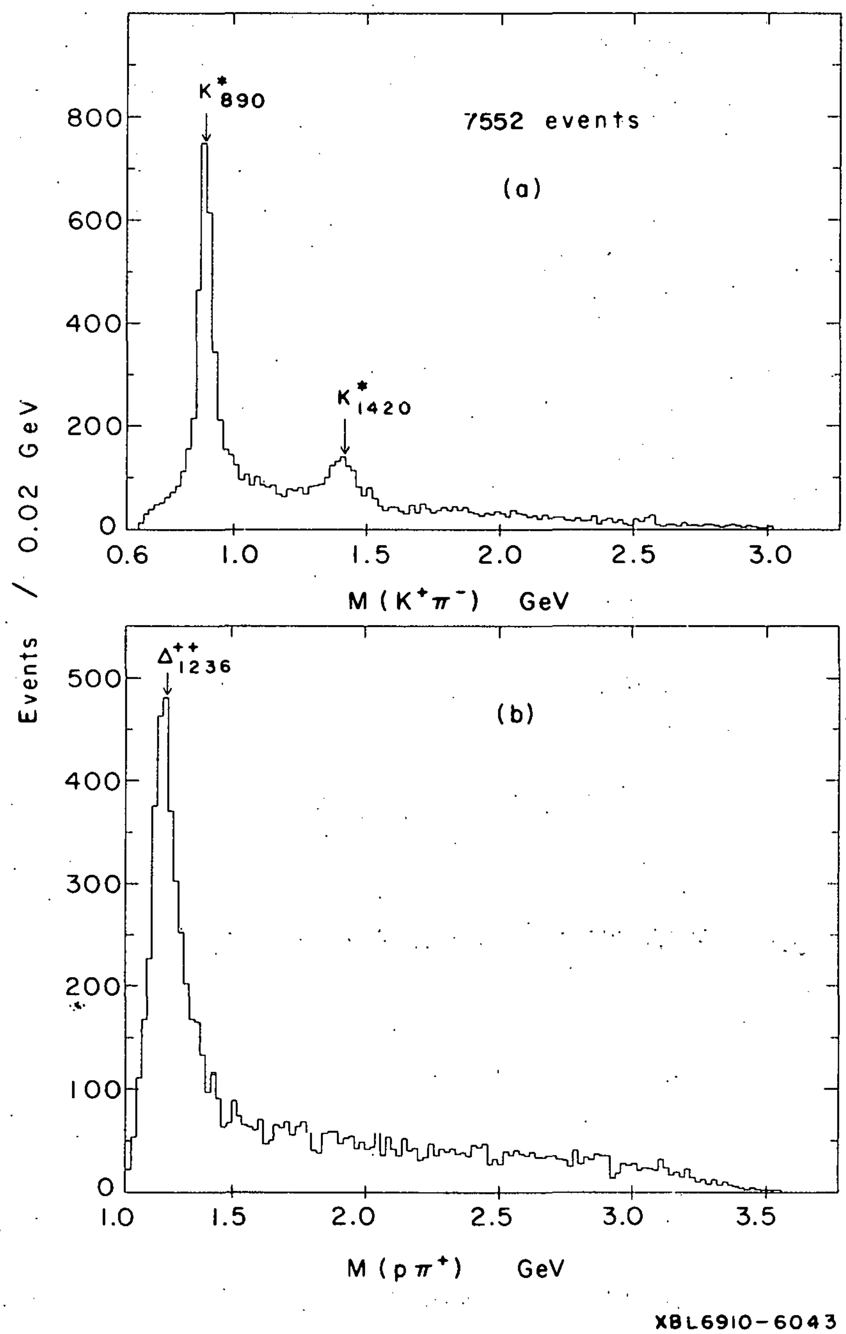

K^*_{890}
7552 events
(a)
K^*_{1420}
800
600
400
200
0
0.6
1.0
1.5
2.0
2.5
3.0
M ($K^+\pi^-$) GeV
Events / 0.02 GeV
Δ^{++}_{1236}
(b)
500
400
300
200
100
0
1.0
1.5
2.0
2.5
3.0
3.5
M ($p\pi^+$) GeV
XBL6910-6043

Fig. 3

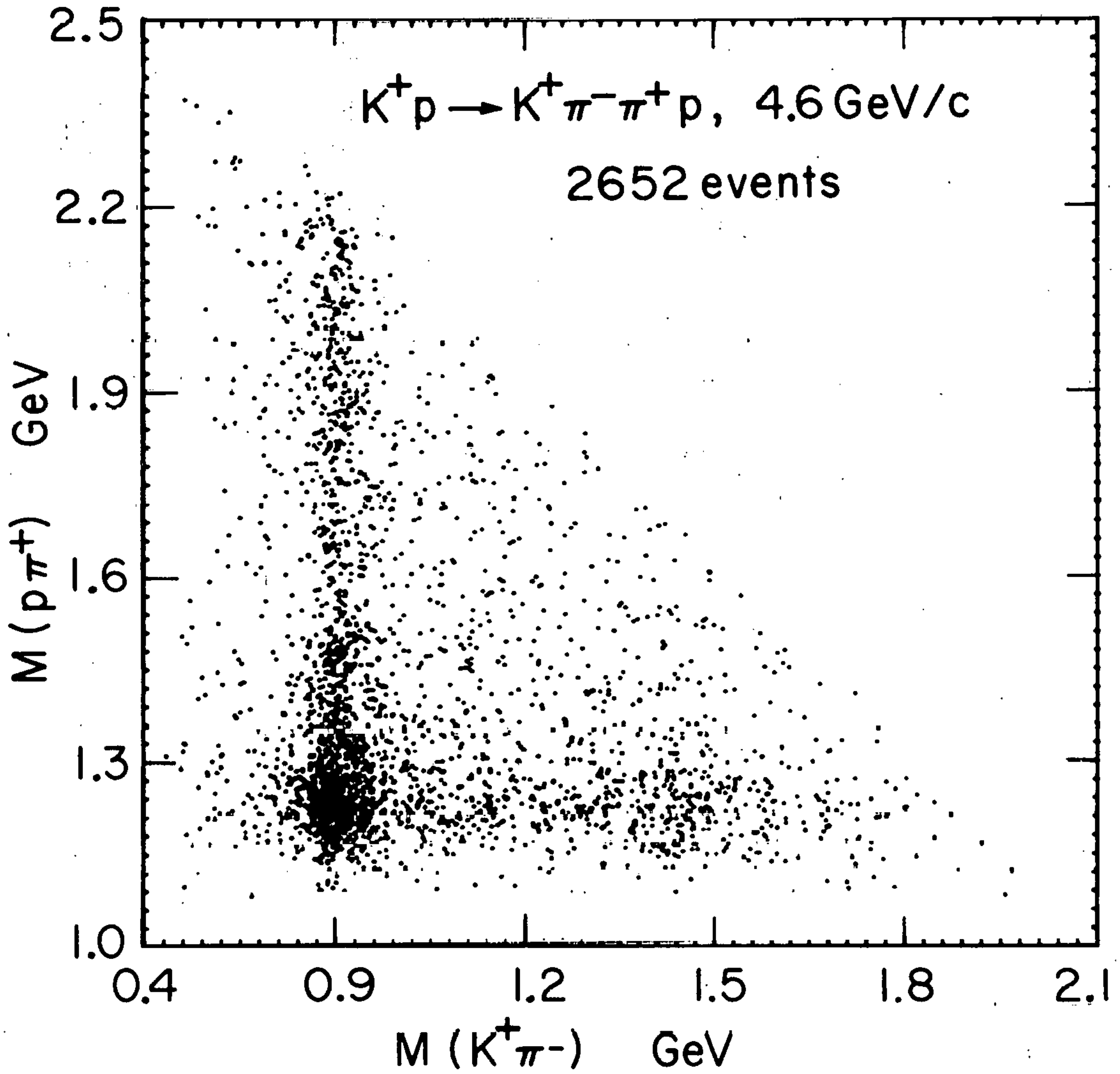

XBL696-3048

Fig. 4

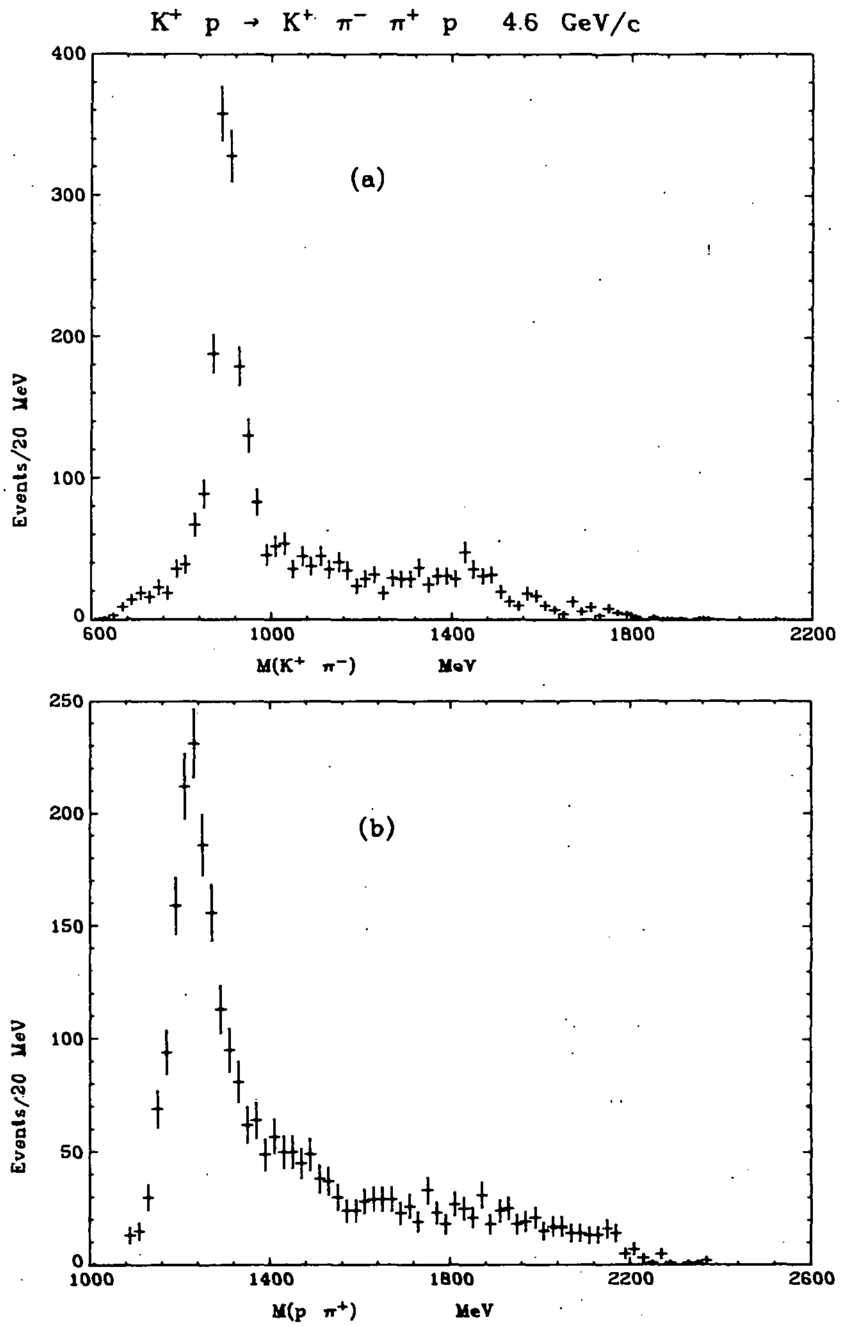

XBL705-2928

Fig. 5

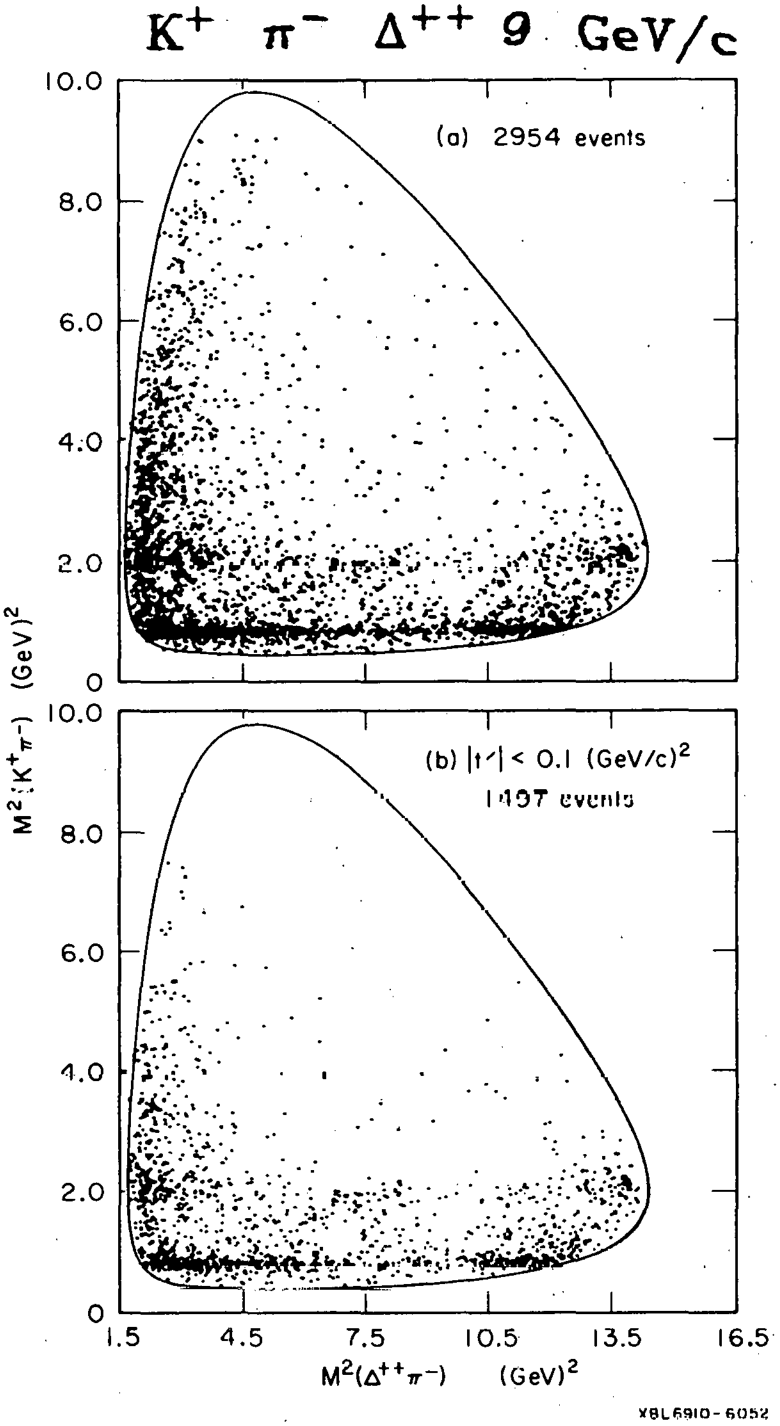

K+ π− Δ++ 9 GeV/c
(a) 2954 events
(b) |t′| < 0.1 (GeV/c)2
1497 events
M2(K+π−) (GeV)2
M2(Δ++π−) (GeV)2
10.0
8.0
6.0
4.0
2.0
0
1.5
4.5
7.5
10.5
13.5
16.5
XBL6910-6052

Fig. 6

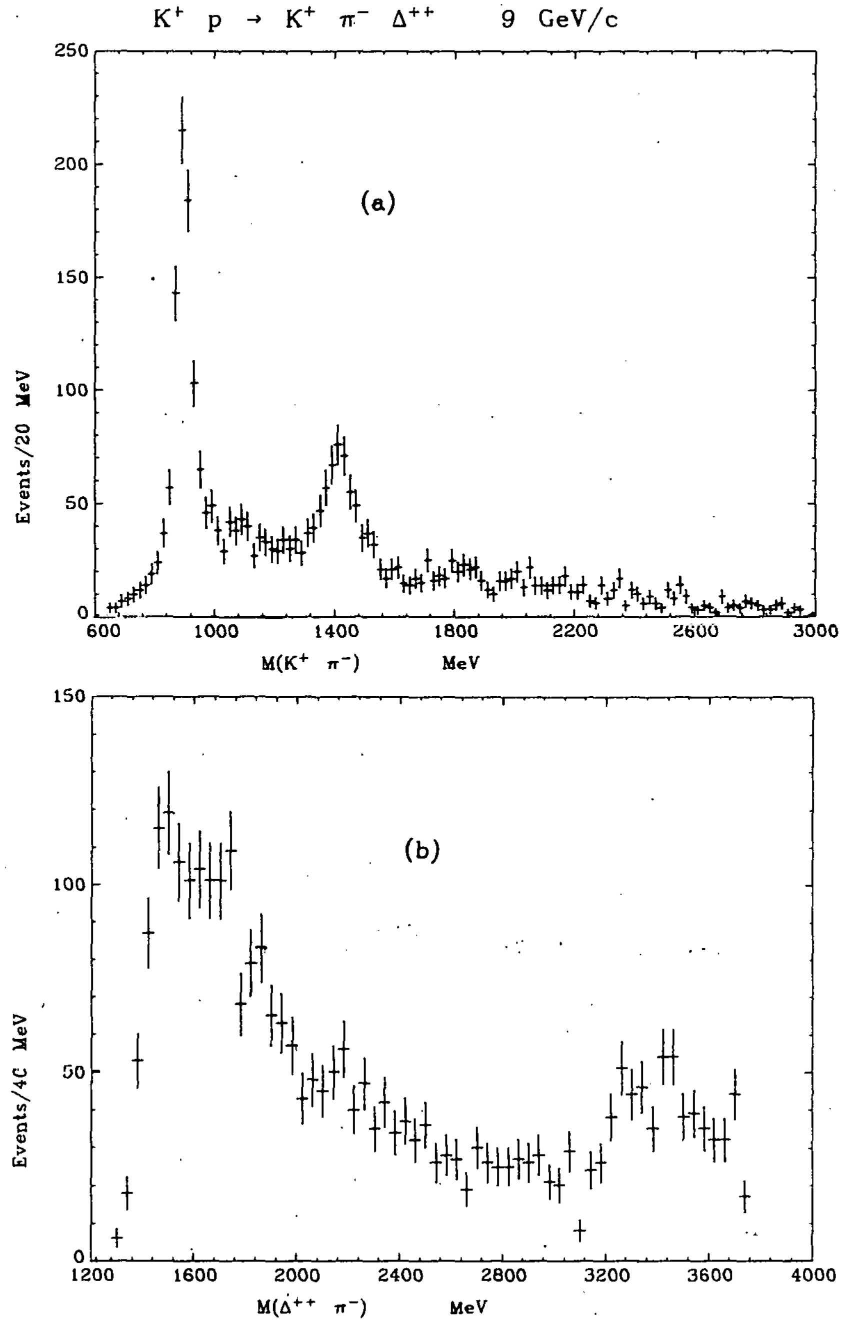

XBL706-3115

Fig. 7

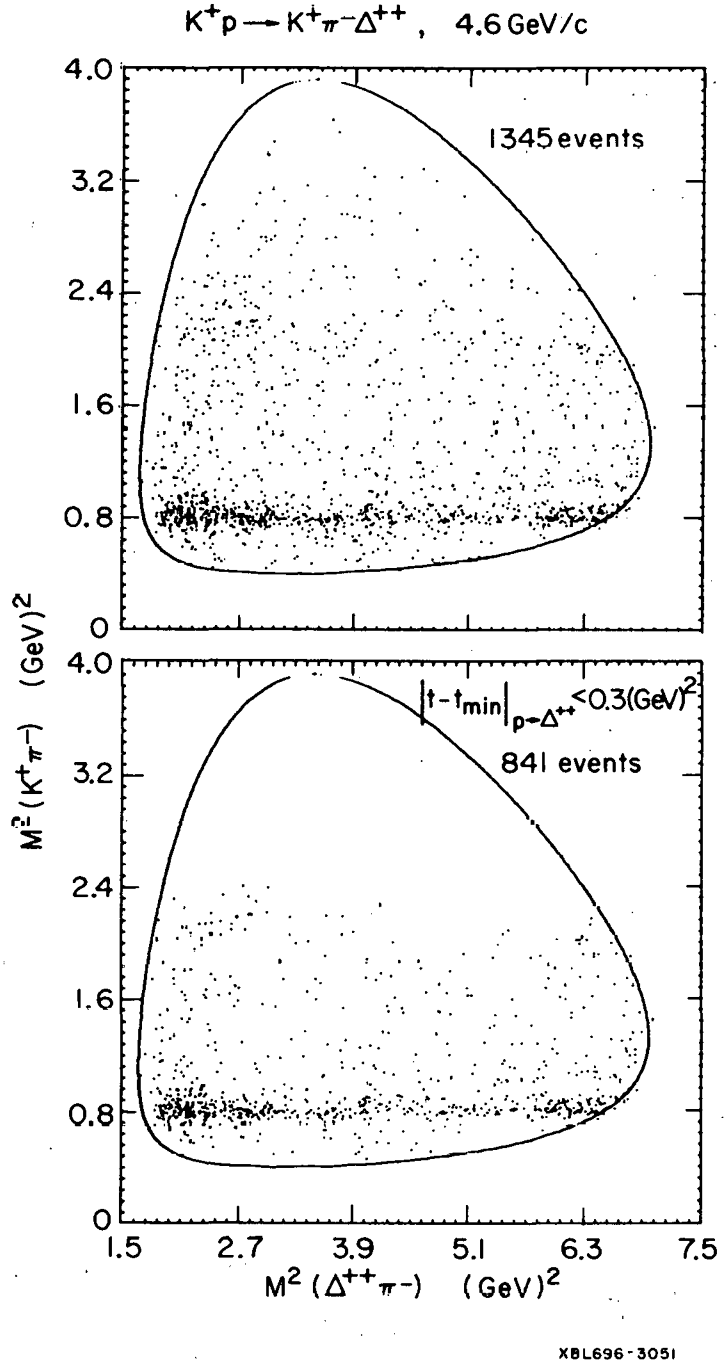
K+p → K+π−Δ++ , 4.6 GeV/c
1345 events
|t - tmin|p-Δ++ <0.3(GeV)2
841 events
M2 (K+π−) (GeV)2
M2 (Δ++π−) (GeV)2
4.0
3.2
2.4
1.6
0.8
0
1.5
2.7
3.9
5.1
6.3
7.5
XBL696-3051

Fig. 8

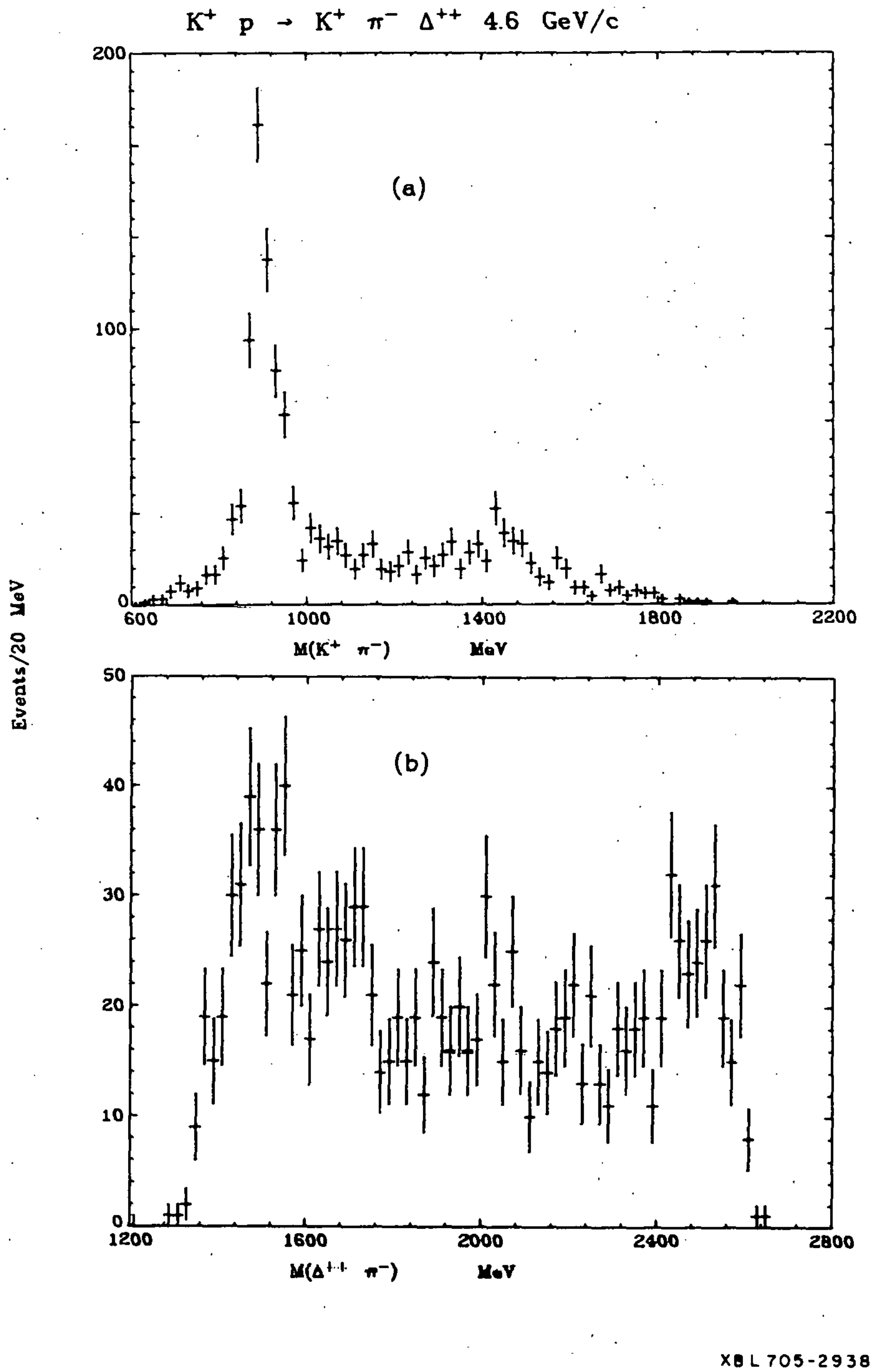

$K^+ p \to K^+ \pi^- \Delta^{++}$ 4.6 GeV/c
(a)
200
100
0
600
1000
1400
1800
2200
$M(K^+ \pi^-)$ MeV
Events/20 MeV
(b)
50
40
30
20
10
0
1200
1600
2000
2400
2800
$M(\Delta^{++} \pi^-)$ MeV
XBL 705-2938

Fig. 9

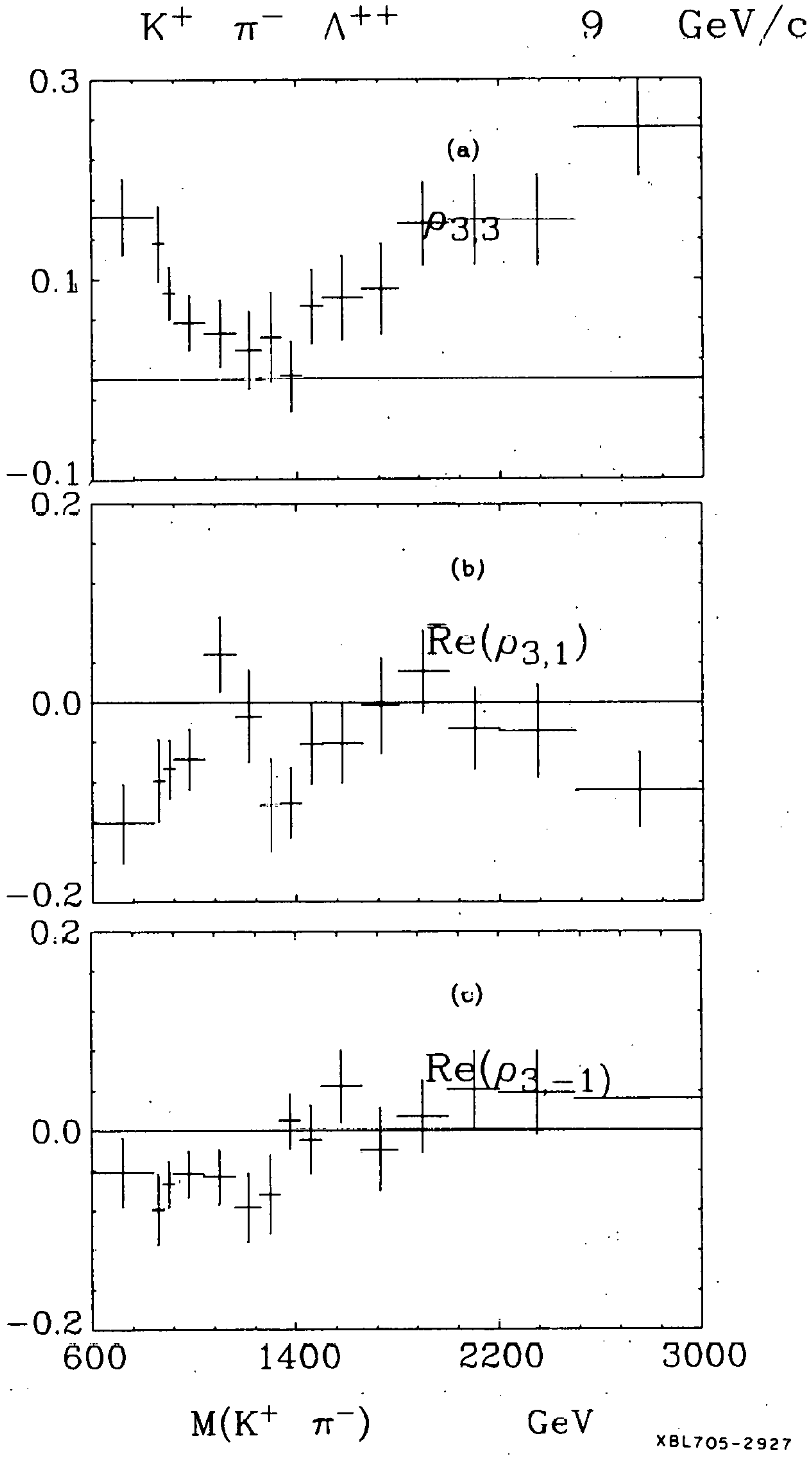
K^+ π^- Δ^{++} 9 GeV/c
0.3
0.1
−0.1
(a)
$\rho_{3,3}$
0.2
0.0
−0.2
(b)
$\mathrm{Re}(\rho_{3,1})$
0.2
0.0
−0.2
(c)
$\mathrm{Re}(\rho_{3,-1})$
600
1400
2200
3000
$M(K^+ \pi^-)$ GeV
XBL705-2927

Fig. 10

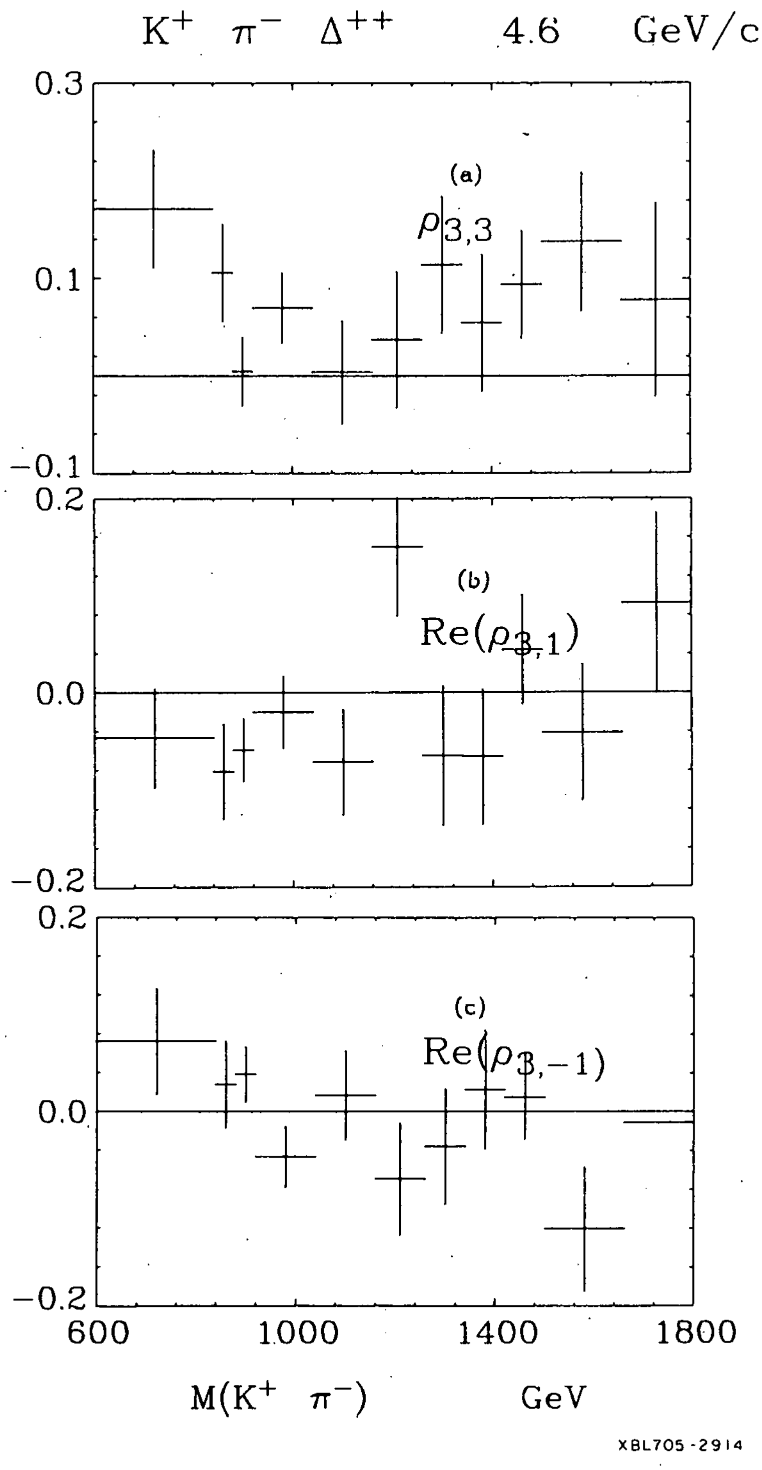
K+ π− Δ++ 4.6 GeV/c
0.3
0.1
−0.1
(a)
ρ3,3
0.2
0.0
−0.2
(b)
Re(ρ3,1)
0.2
0.0
−0.2
(c)
Re(ρ3,−1)
600
1000
1400
1800
M(K+ π−) GeV
XBL705-2914

Fig. 11

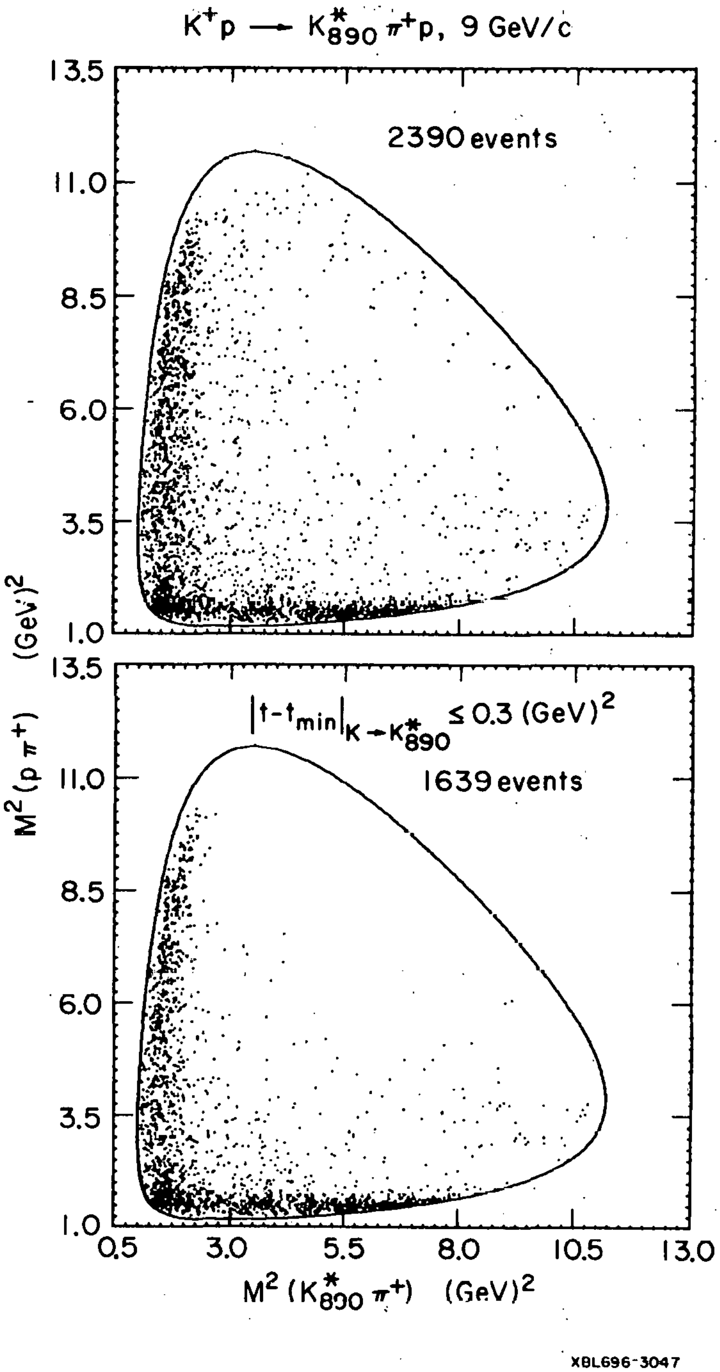

$K^+p \longrightarrow K^*_{890}\pi^+p$, 9 GeV/c
2390 events
$|t-t_{min}|_{K\to K^*_{890}} \leq 0.3\ (GeV)^2$
1639 events
$M^2(p\pi^+)$ $(GeV)^2$
$M^2(K^*_{890}\pi^+)$ $(GeV)^2$
13.5
11.0
8.5
6.0
3.5
1.0
0.5
3.0
5.5
8.0
10.5
13.0
XBL696-3047

Fig. 12

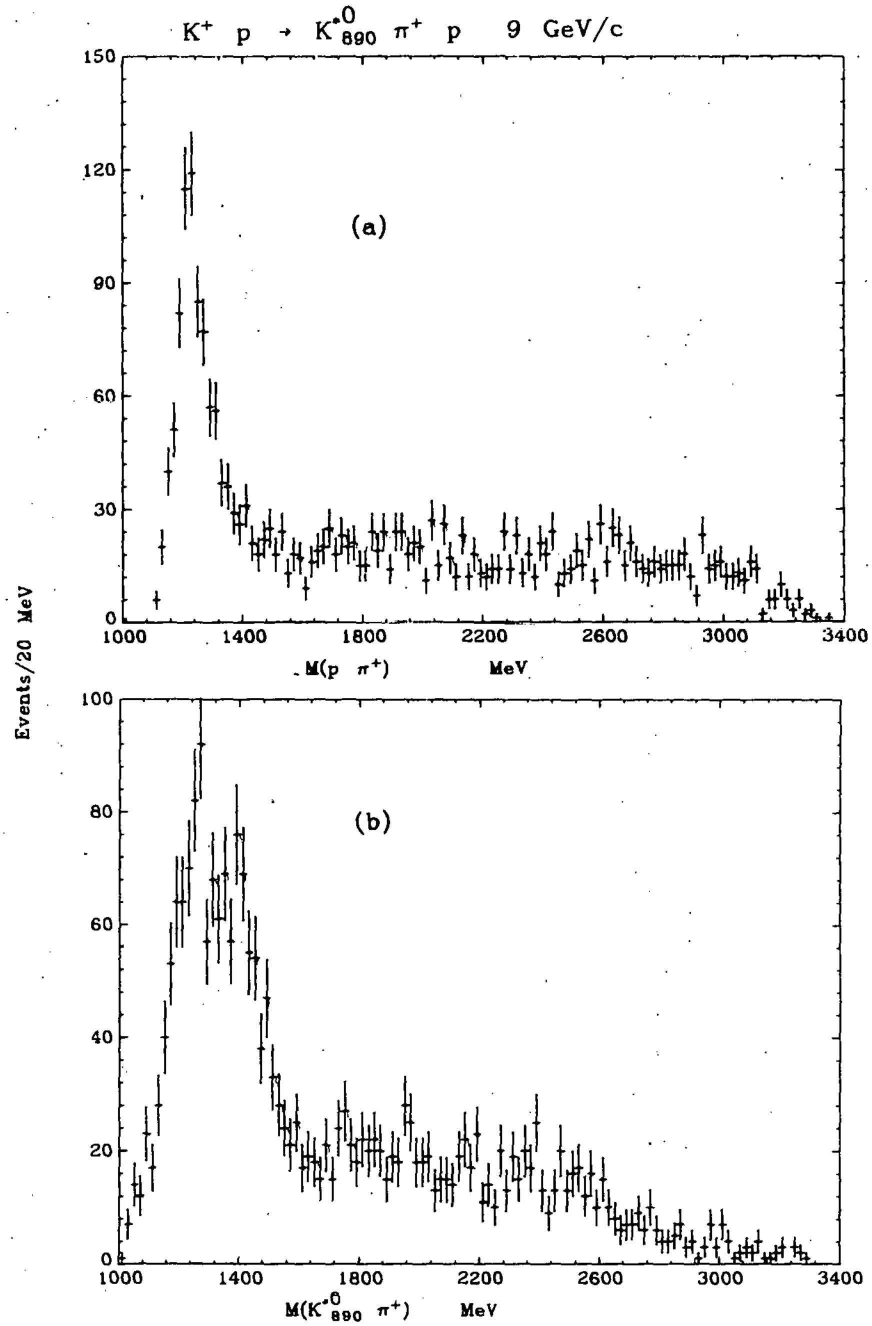

XBL705-2937

Fig. 13

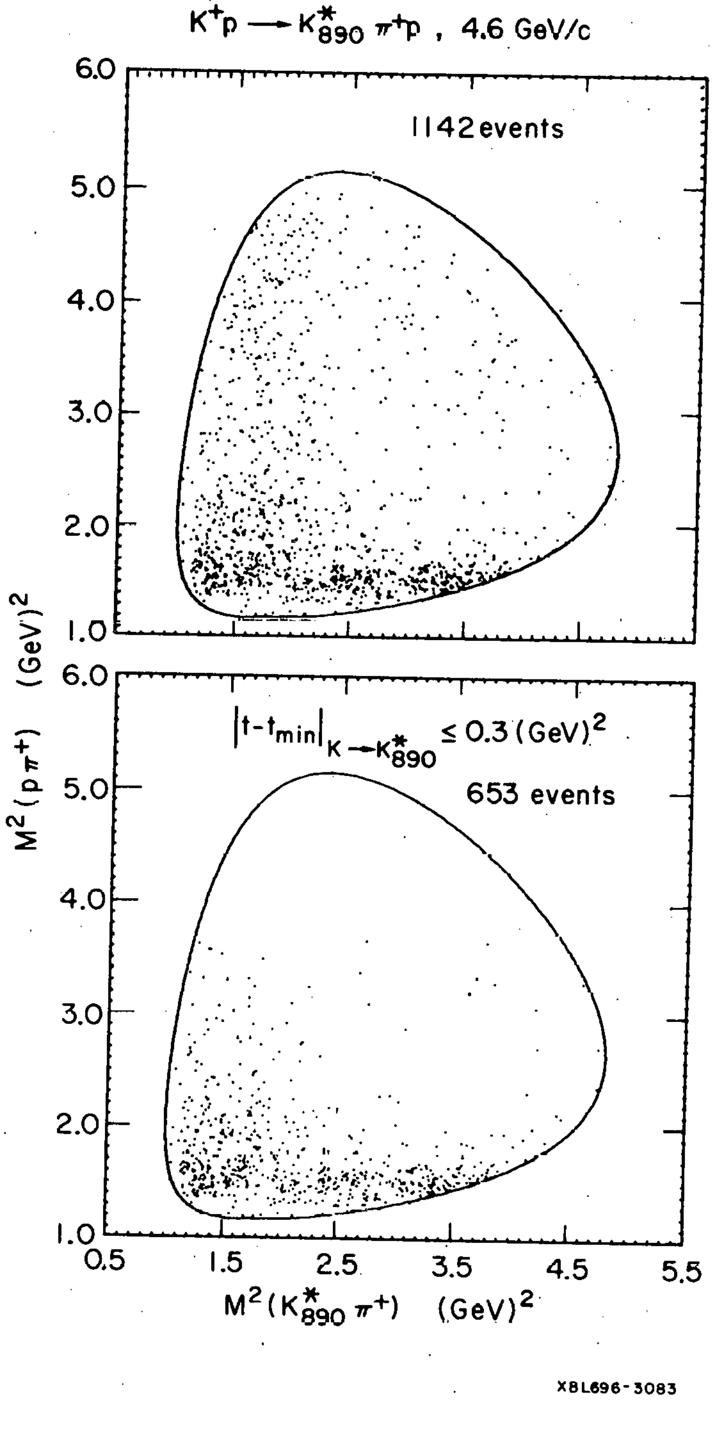

K+p → K*890 π+p , 4.6 GeV/c
1142 events
|t-tmin|K→K*890 ≤ 0.3 (GeV)2
653 events
6.0
5.0
4.0
3.0
2.0
1.0
M2(pπ+) (GeV)2
0.5
1.5
2.5
3.5
4.5
5.5
M2(K*890 π+) (GeV)2
XBL696-3083

Fig. 14

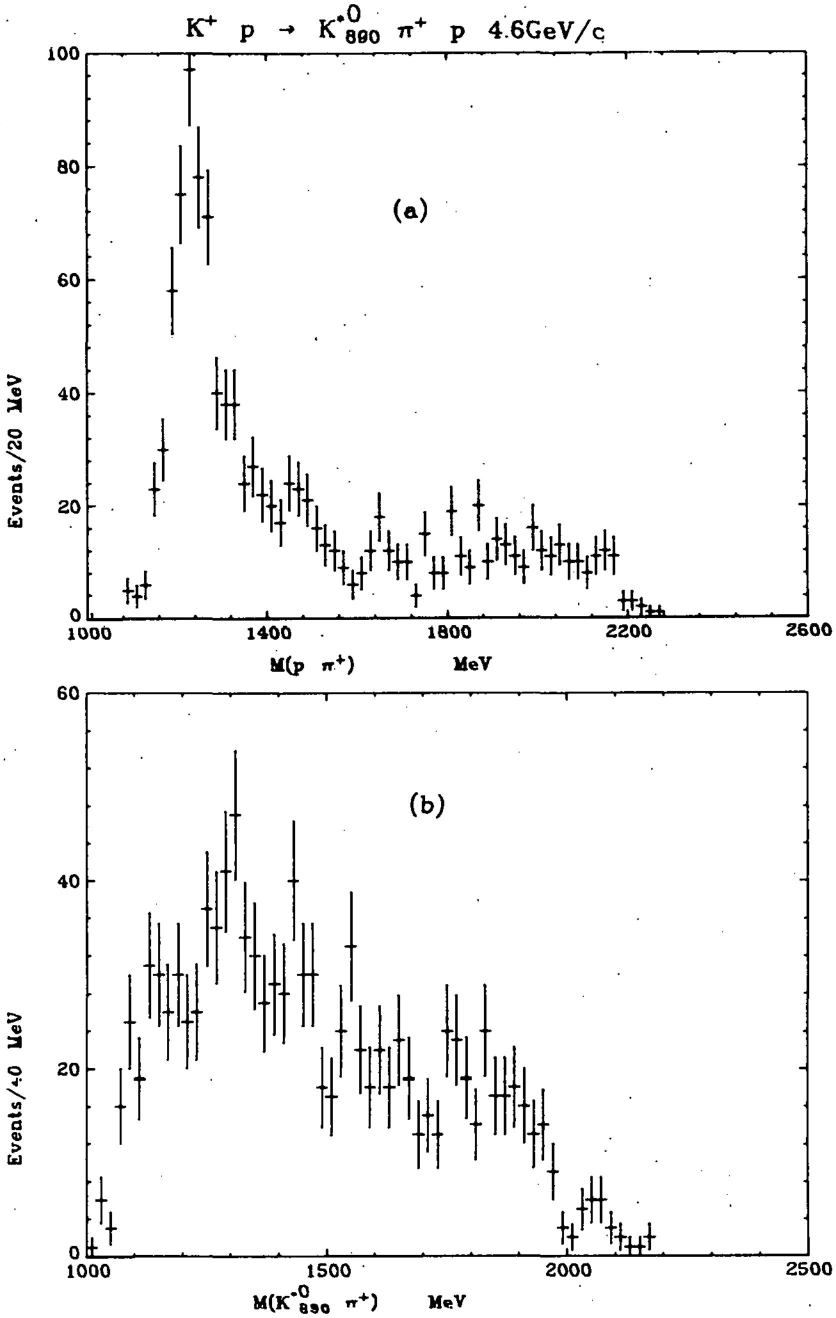

$K^+ p \rightarrow K^{*0}_{890} \pi^+ p$ 4.6GeV/c
(a)
Events/20 MeV
M(p π^+) MeV
(b)
Events/40 MeV
M(K^{*0}_{890} π^+) MeV
XBL 705-2940

Fig. 15

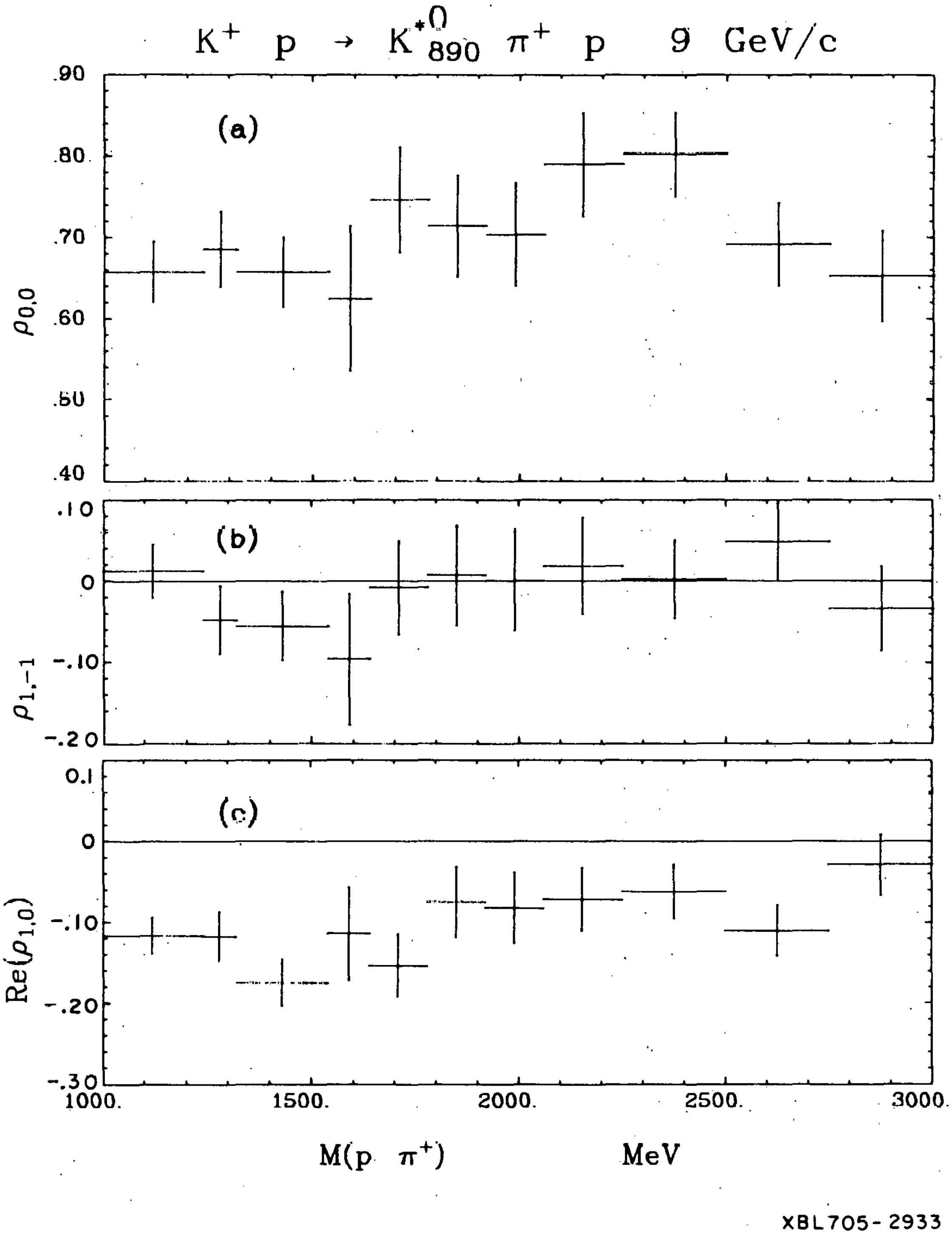

$K^+ \ p \rightarrow K^{*0}_{890} \ \pi^+ \ p \quad 9 \ GeV/c$
(a)
(b)
(c)
$\rho_{0,0}$
$\rho_{1,-1}$
$Re(\rho_{1,0})$
.90
.80
.70
.60
.50
.40
.10
0
-.10
-.20
0.1
-.30
1000.
1500.
2000.
2500.
3000.
$M(p \ \pi^+)$ MeV
XBL705-2933

Fig. 16

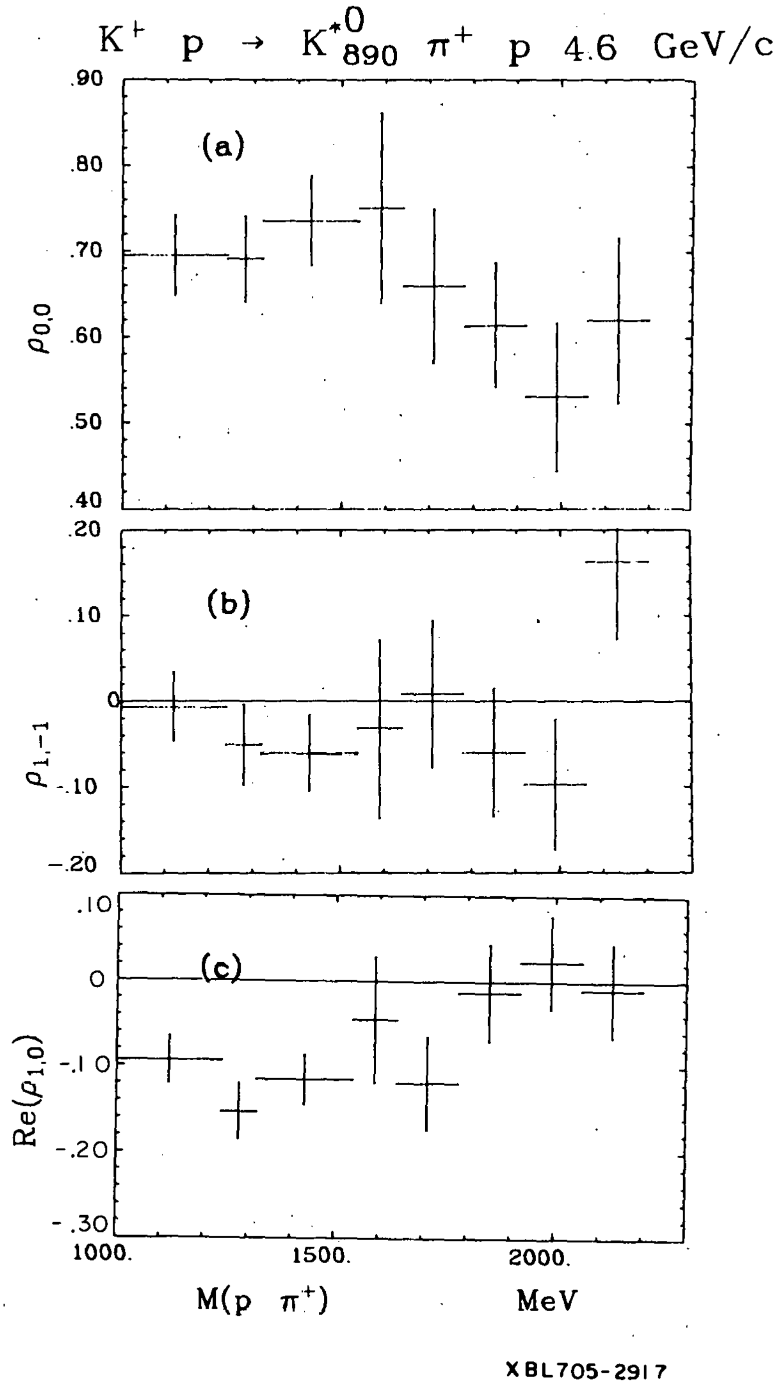

$K^+ p \rightarrow K^{*0}_{890} \pi^+ p$ 4.6 GeV/c
(a)
(b)
(c)
$\rho_{0,0}$
$\rho_{1,-1}$
$Re(\rho_{1,0})$
.90
.80
.70
.60
.50
.40
.20
.10
0
-.10
-.20
.10
0
-.10
-.20
-.30
1000.
1500.
2000.
$M(p\ \pi^+)$ MeV
XBL705-2917

Fig. 17

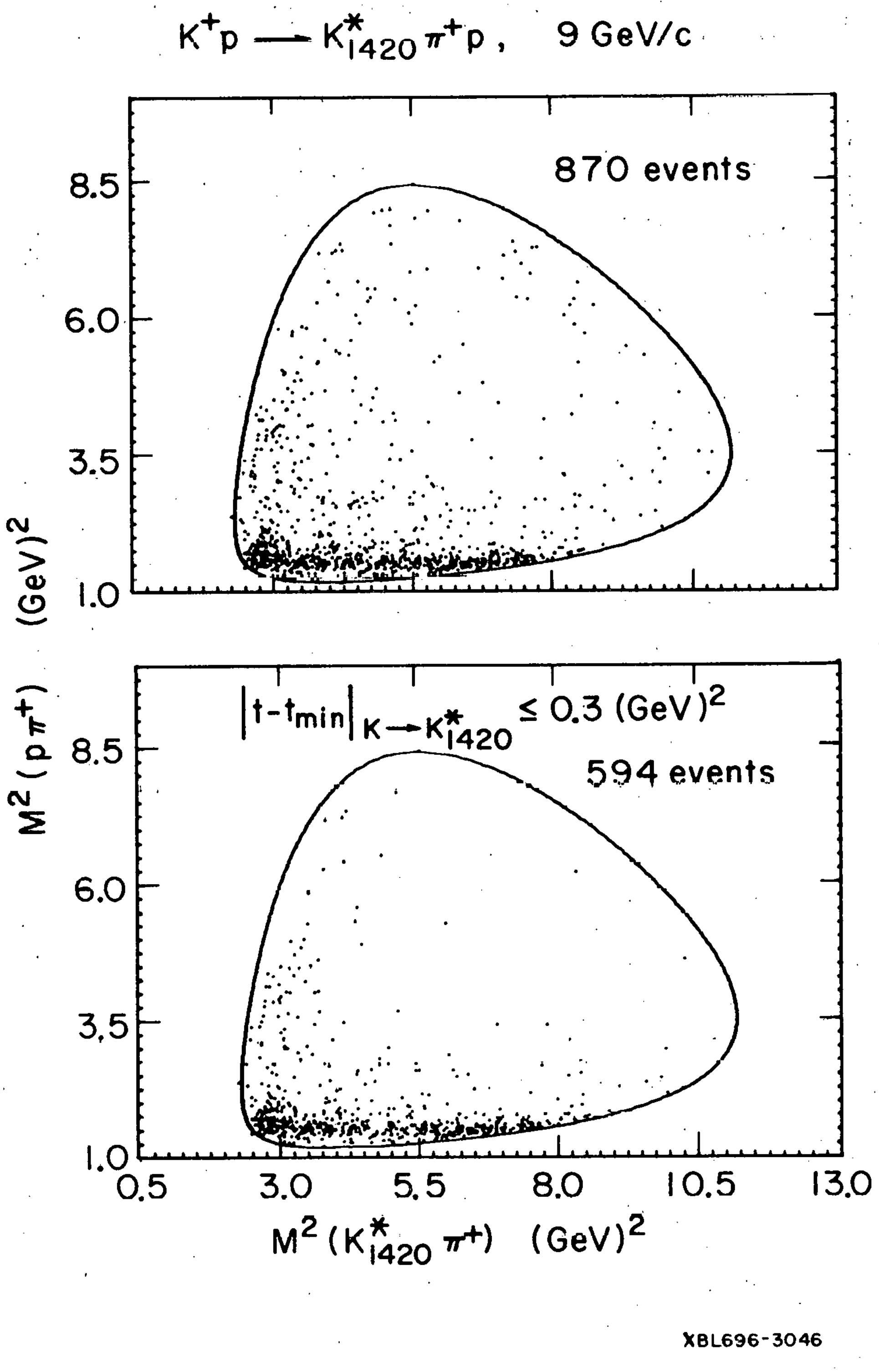
$K^+p \longrightarrow K^*_{1420}\pi^+p$, 9 GeV/c
870 events
$|t-t_{min}|_{K\rightarrow K^*_{1420}} \leq 0.3\ (GeV)^2$
594 events
8.5
6.0
3.5
1.0
0.5
3.0
5.5
8.0
10.5
13.0
$M^2(p\pi^+)\ (GeV)^2$
$M^2(K^*_{1420}\pi^+)\ (GeV)^2$
XBL696-3046

Fig. 18

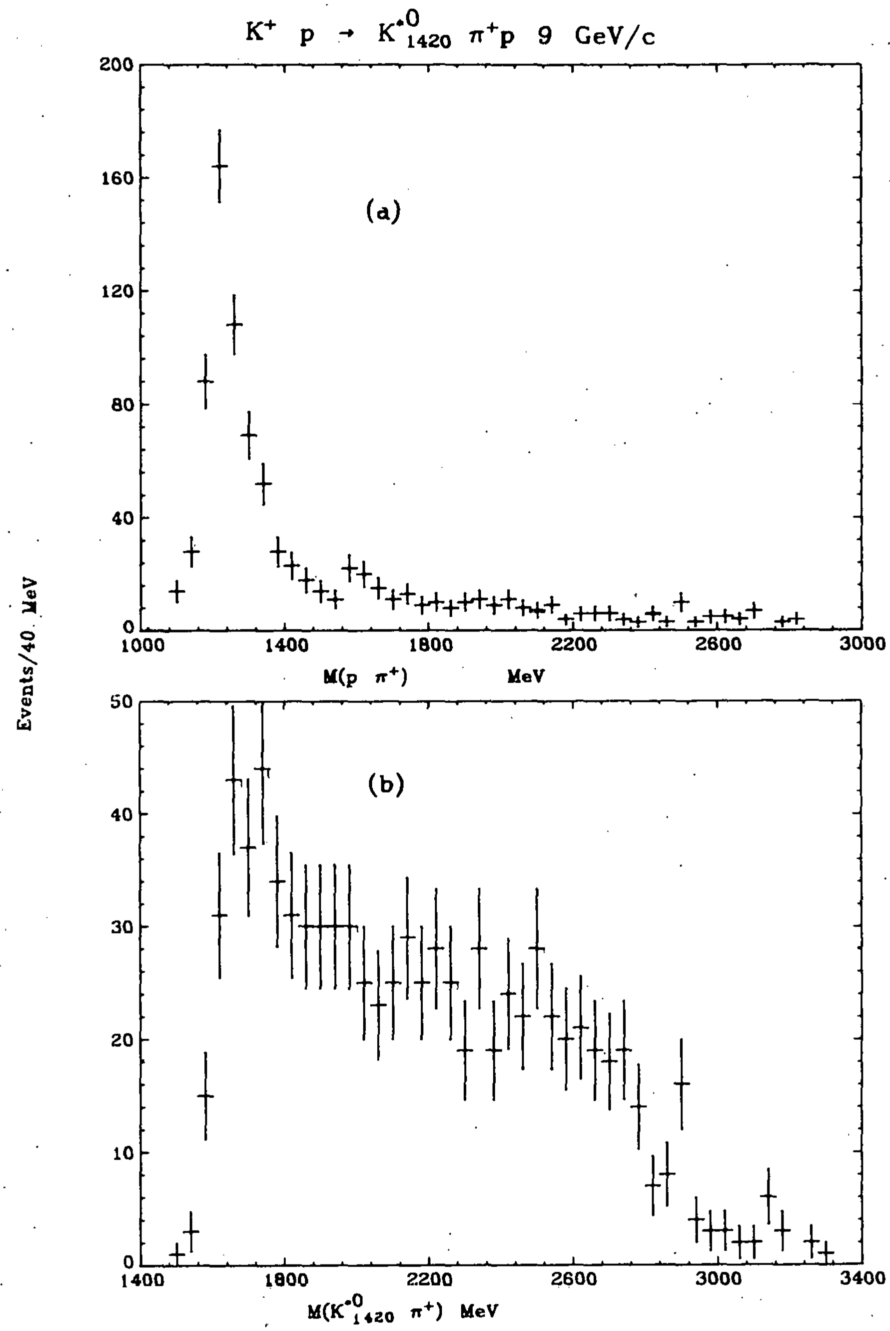

XBL 705-2936

Fig. 19

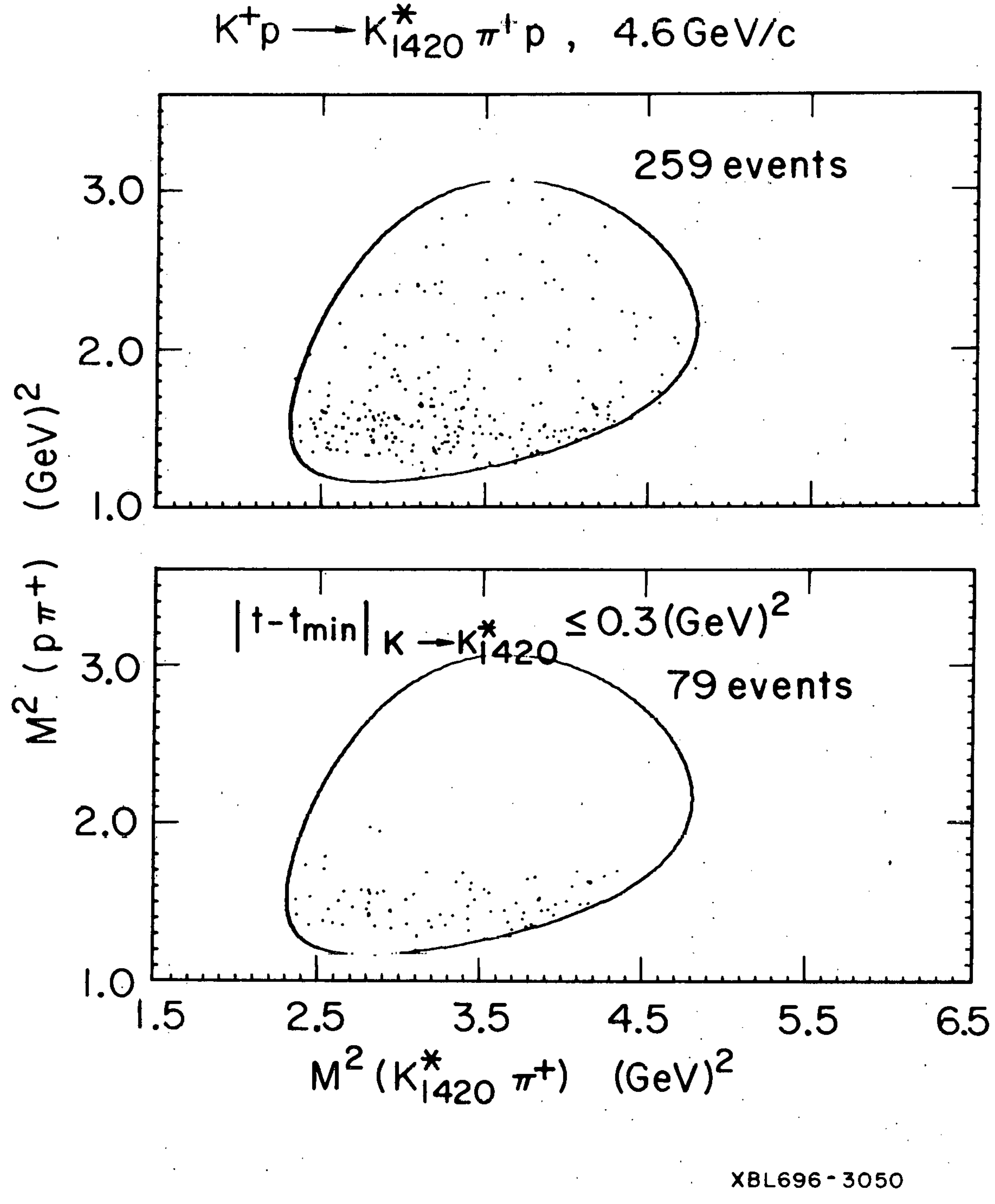

$K^+p \longrightarrow K^*_{1420}\pi^+p$, 4.6 GeV/c
259 events
$|t-t_{min}|_{K\to K^*_{1420}} \leq 0.3 (GeV)^2$
79 events
$M^2(p\pi^+)$ $(GeV)^2$
$M^2(K^*_{1420}\pi^+)$ $(GeV)^2$
1.0
2.0
3.0
1.5
2.5
3.5
4.5
5.5
6.5
XBL696-3050

Fig. 20

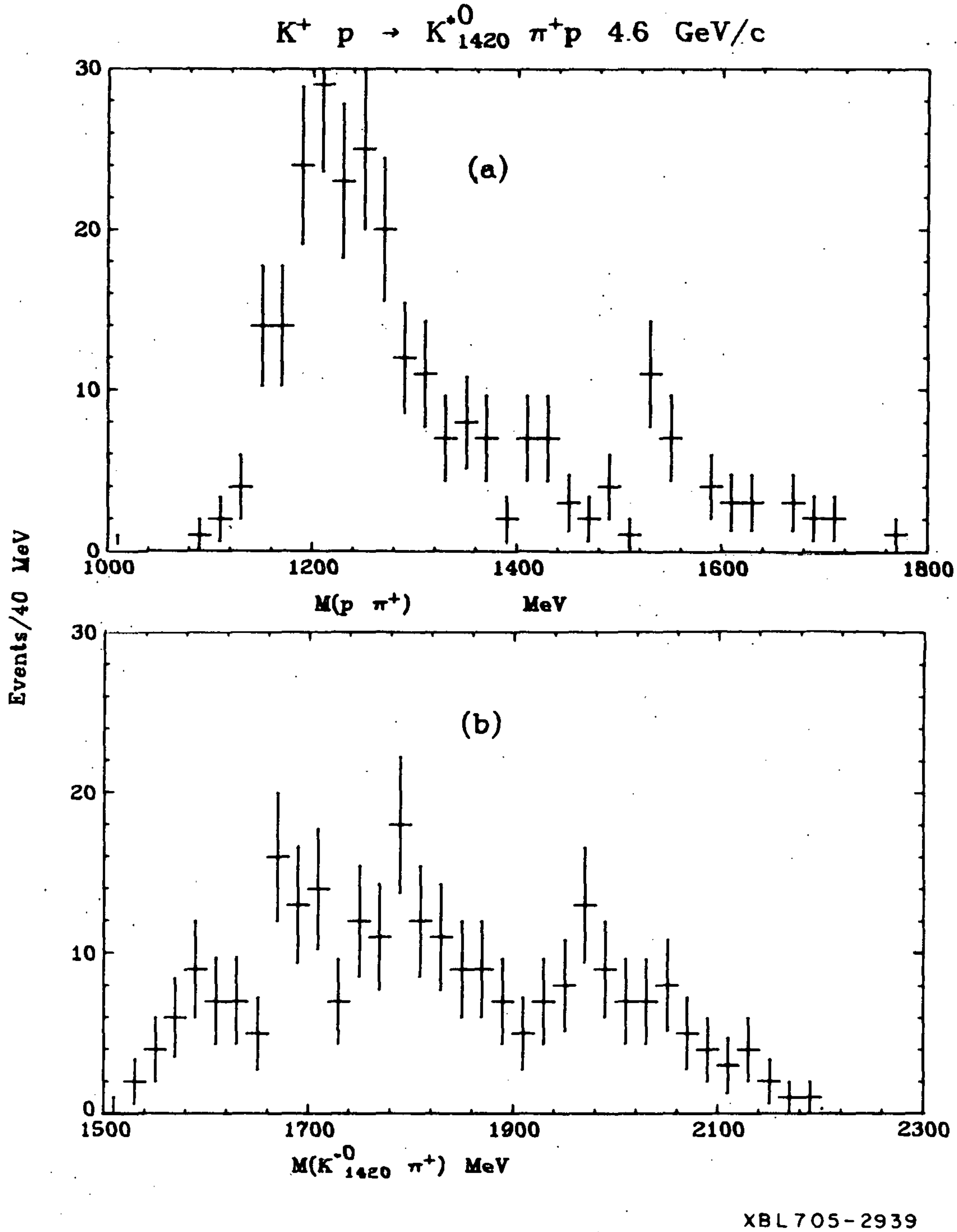
$K^+ p \rightarrow K^{*0}_{1420} \pi^+ p$ 4.6 GeV/c
(a)
(b)
Events/40 MeV
M(p π+) MeV
M(K*0 1420 π+) MeV
XBL705-2939

Fig. 21

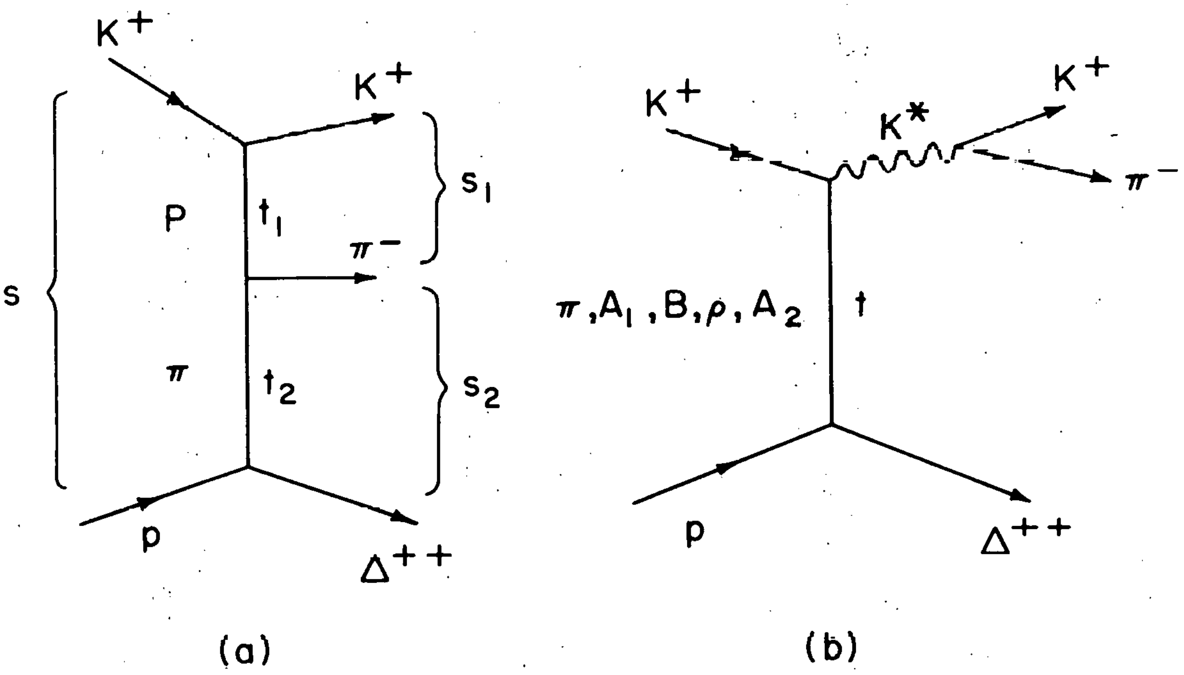

XBL 6910-3958

Fig. 22

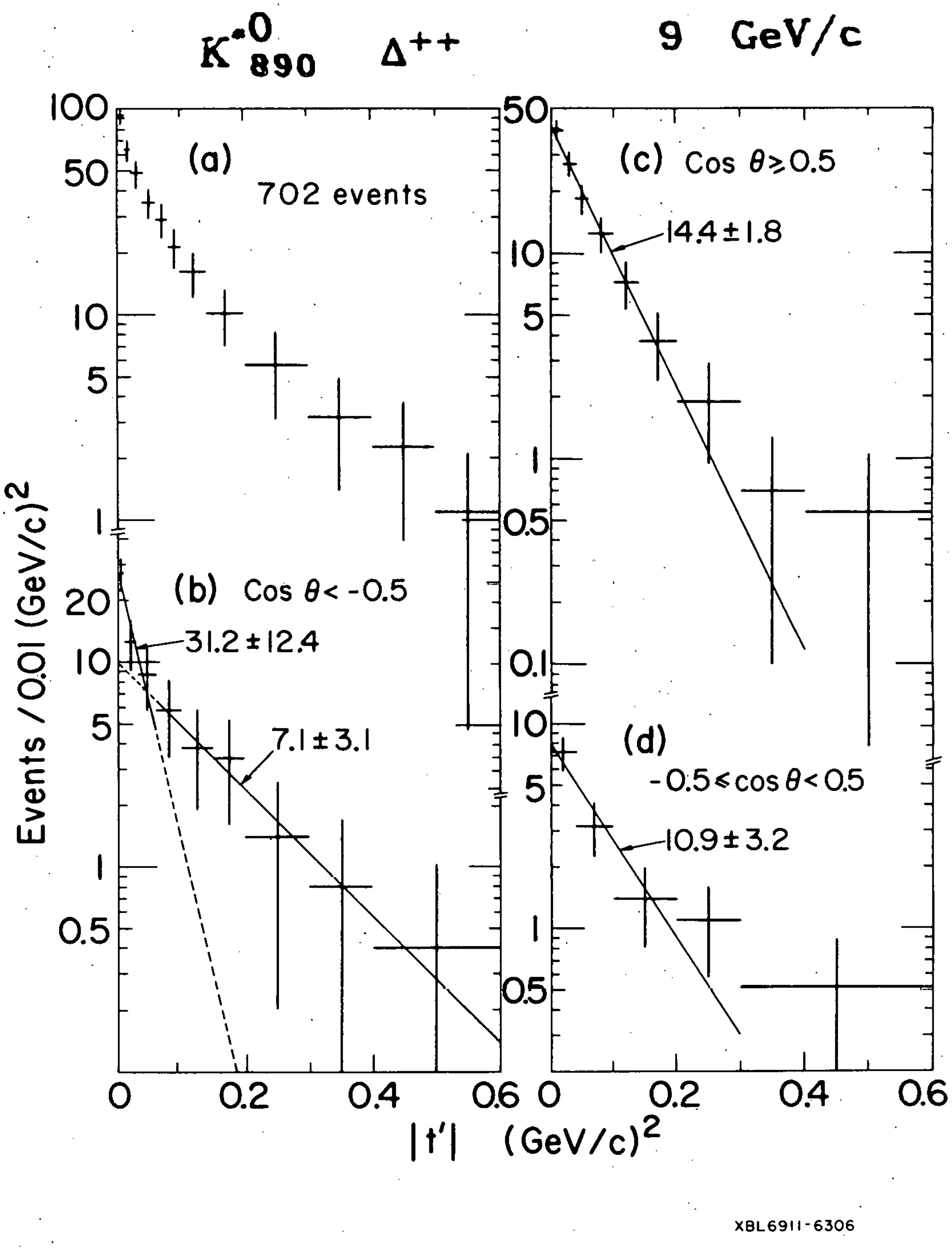

XBL6911-6306

Fig. 23

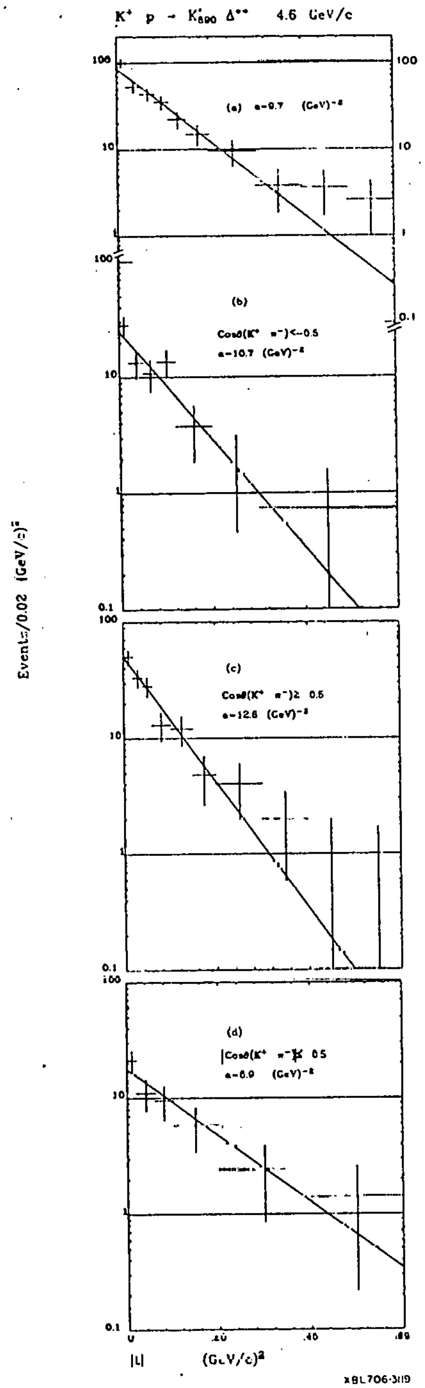
K⁺ p → K*890 Δ⁺⁺ 4.6 GeV/c
(a) a=9.7 (GeV)⁻²
(b)
Cosθ(K⁺ π⁻)<-0.5
a=10.7 (GeV)⁻²
(c)
Cosθ(K⁺ π⁻)≥ 0.5
a=12.6 (GeV)⁻²
(d)
|Cosθ(K⁺ π⁻)|< 0.5
a=6.9 (GeV)⁻²
Events/0.02 (GeV/c)²
|t| (GeV/c)²
XBL706-3119

Fig. 24

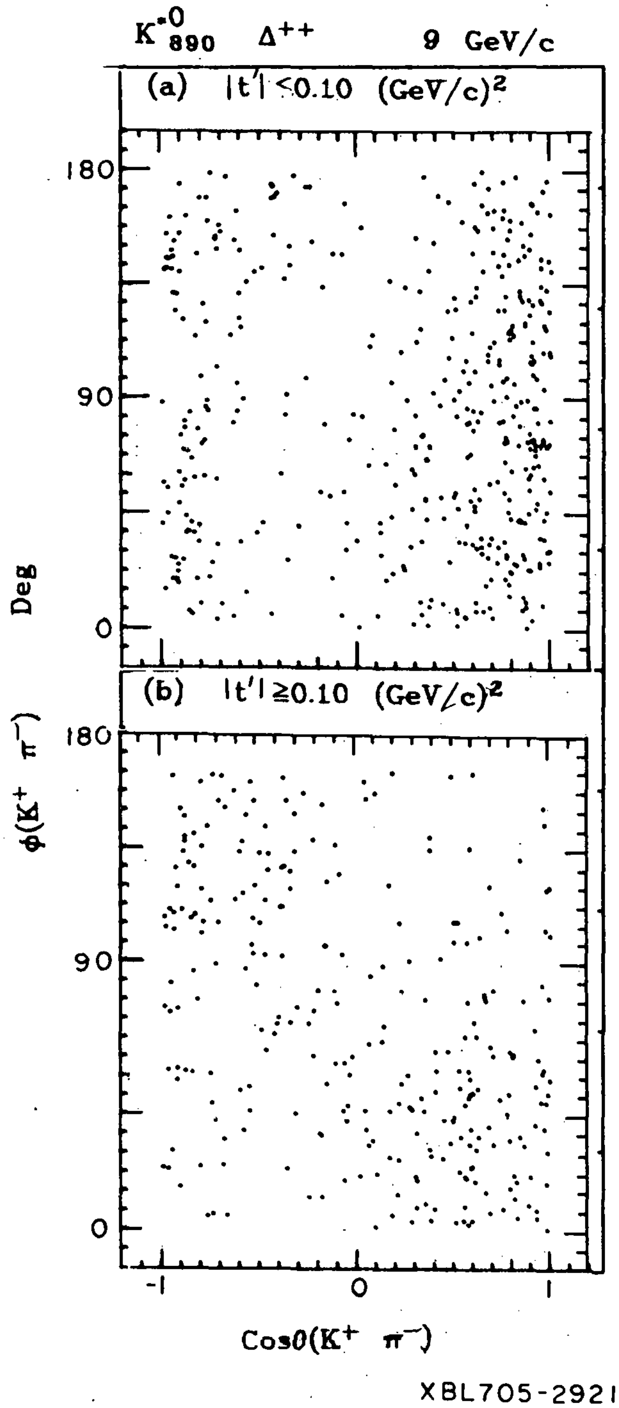

K^{*0}_{890} Δ^{++} 9 GeV/c
(a) |t'| <0.10 (GeV/c)²
(b) |t'| ≥0.10 (GeV/c)²
180
90
0
φ(K⁺ π⁻) Deg
-1
0
1
Cosθ(K⁺ π⁻)
XBL705-2921

Fig. 25

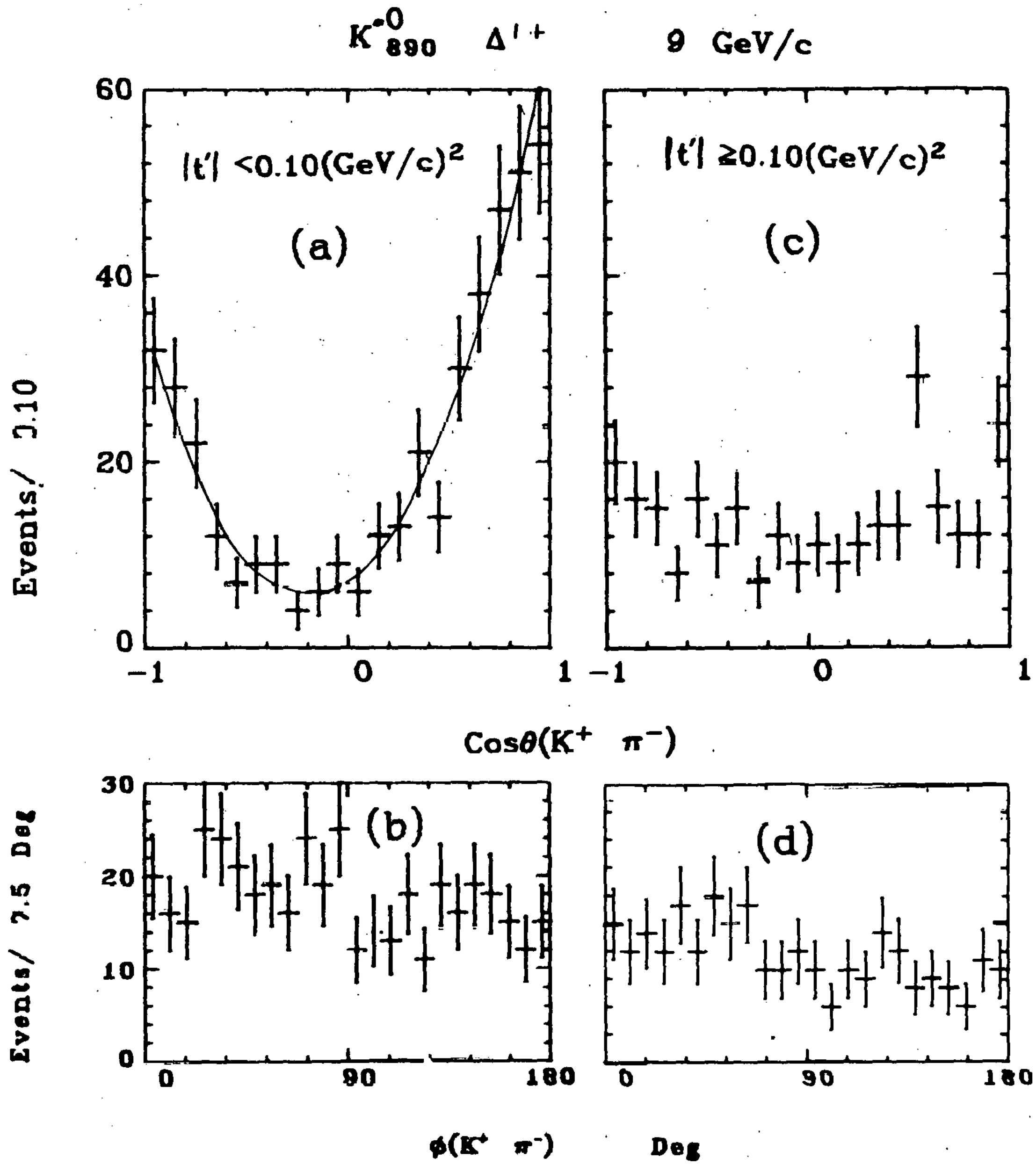

XBL705-2910

Fig. 26

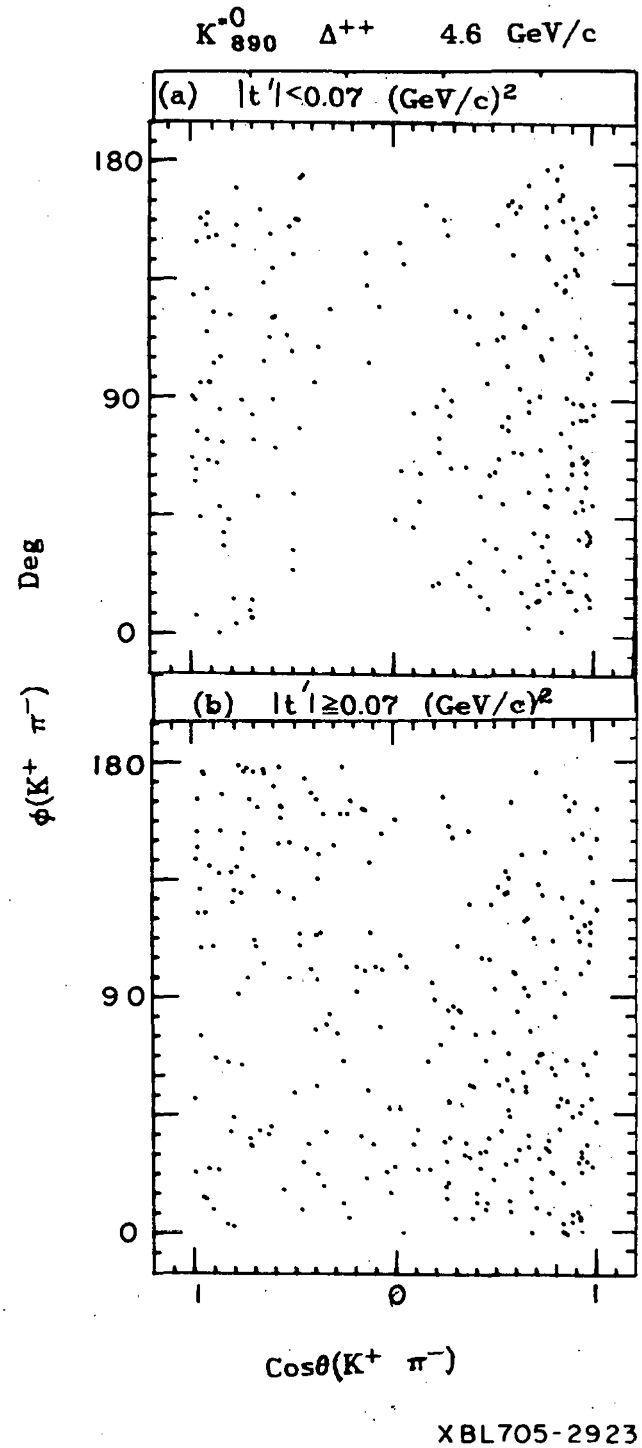

K*0 890 Δ++ 4.6 GeV/c
(a) |t'|<0.07 (GeV/c)²
(b) |t'|≧0.07 (GeV/c)²
180
90
0
φ(K+ π−) Deg
1
0
1
Cosθ(K+ π−)
XBL705-2923

Fig. 27

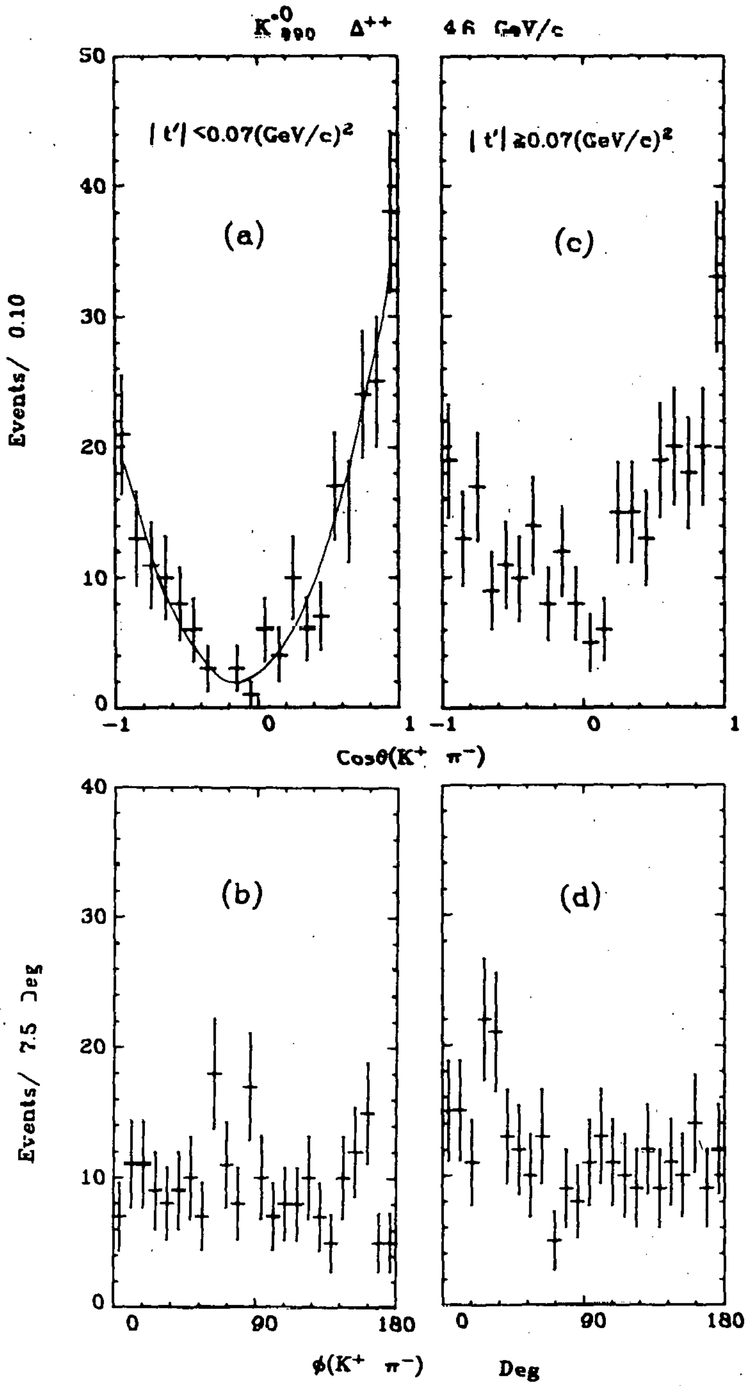

XBL 705-2909

Fig. 28

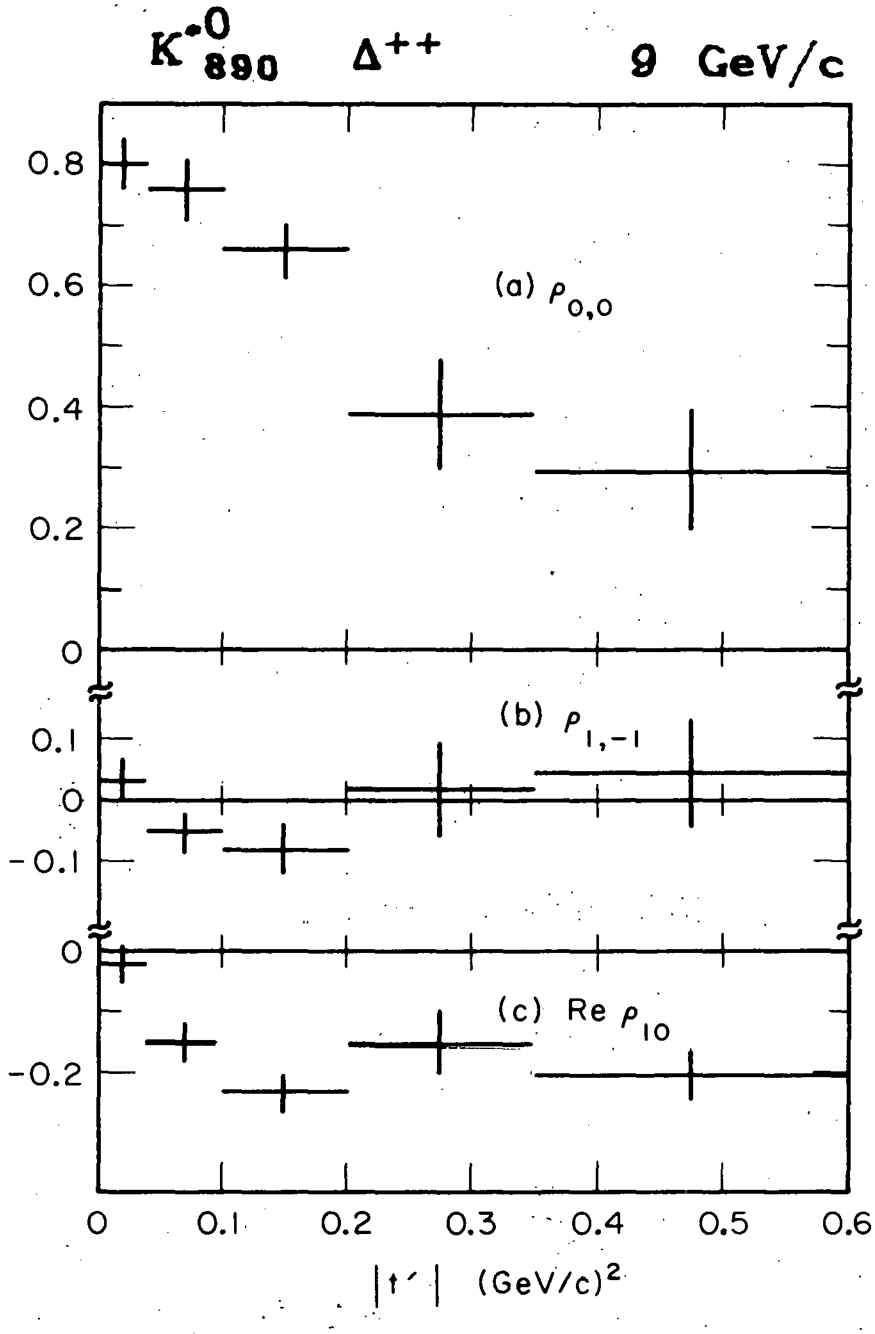

XBL6910-3957

Fig. 29

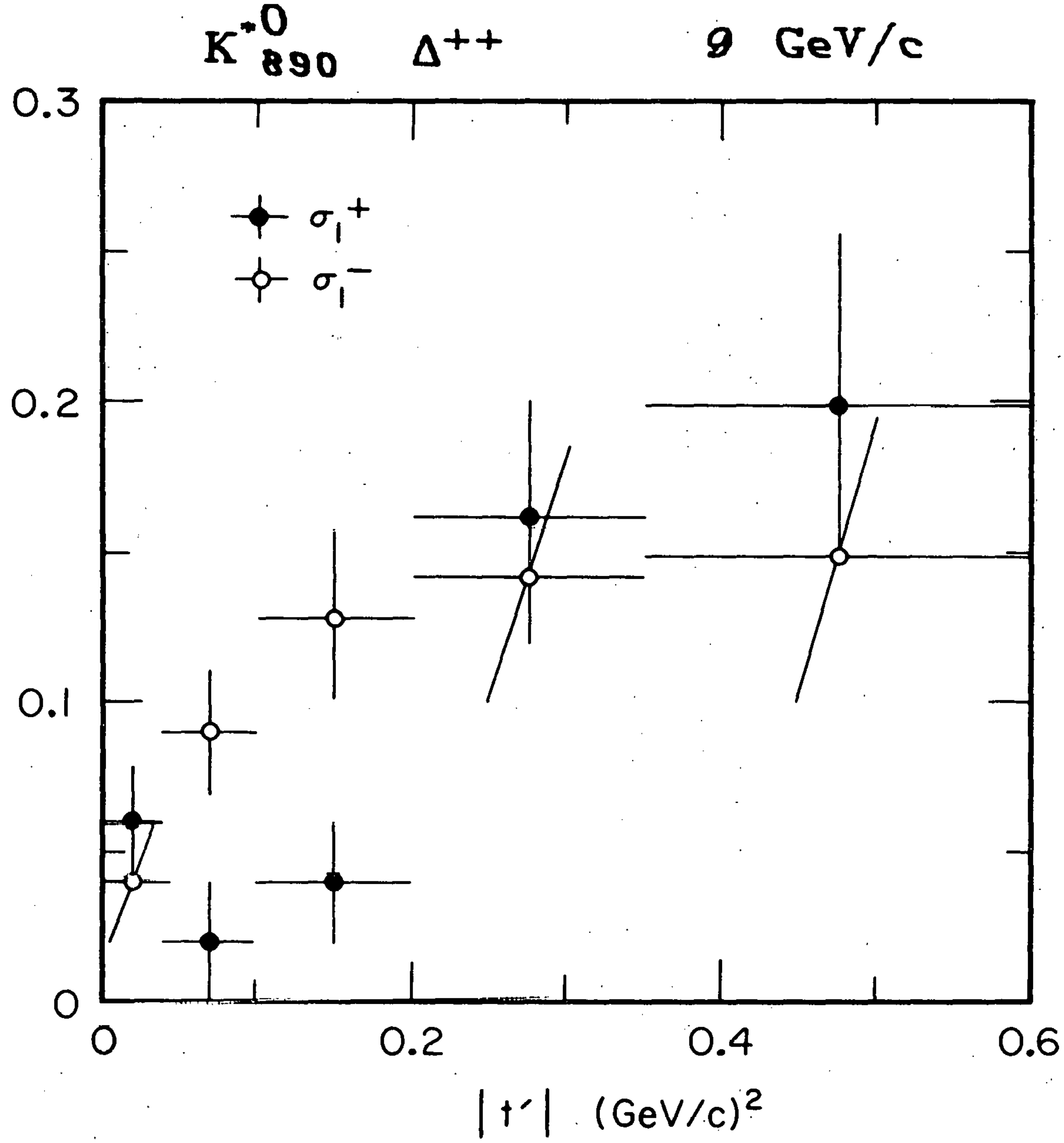

XBL 6910-6041

Fig. 30

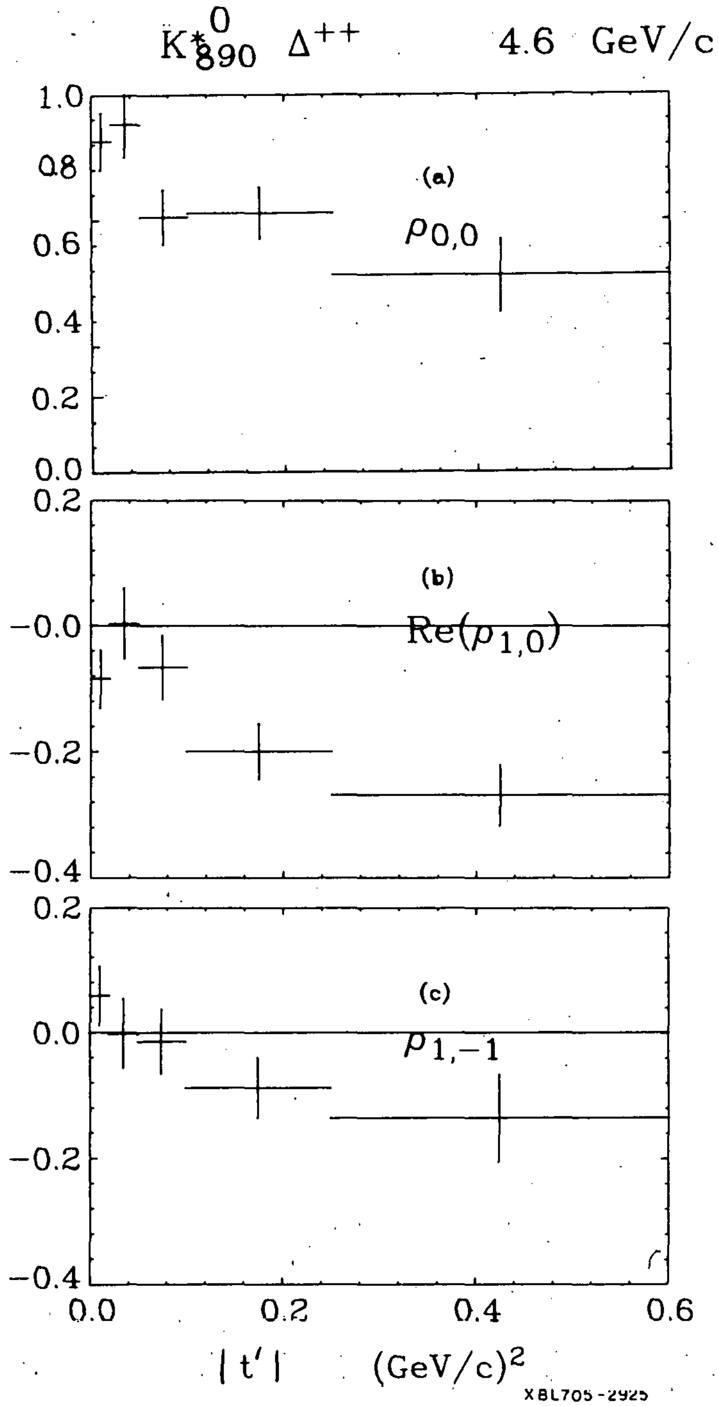
K^{*0}_{890} Δ^{++} 4.6 GeV/c
1.0
0.8
0.6
0.4
0.2
0.0
(a)
$\rho_{0,0}$
0.2
-0.0
-0.2
-0.4
(b)
$\mathrm{Re}(\rho_{1,0})$
0.2
0.0
-0.2
-0.4
(c)
$\rho_{1,-1}$
0.0
0.2
0.4
0.6
$|t'|$ $(\mathrm{GeV/c})^2$
XBL705-2925

Fig. 31

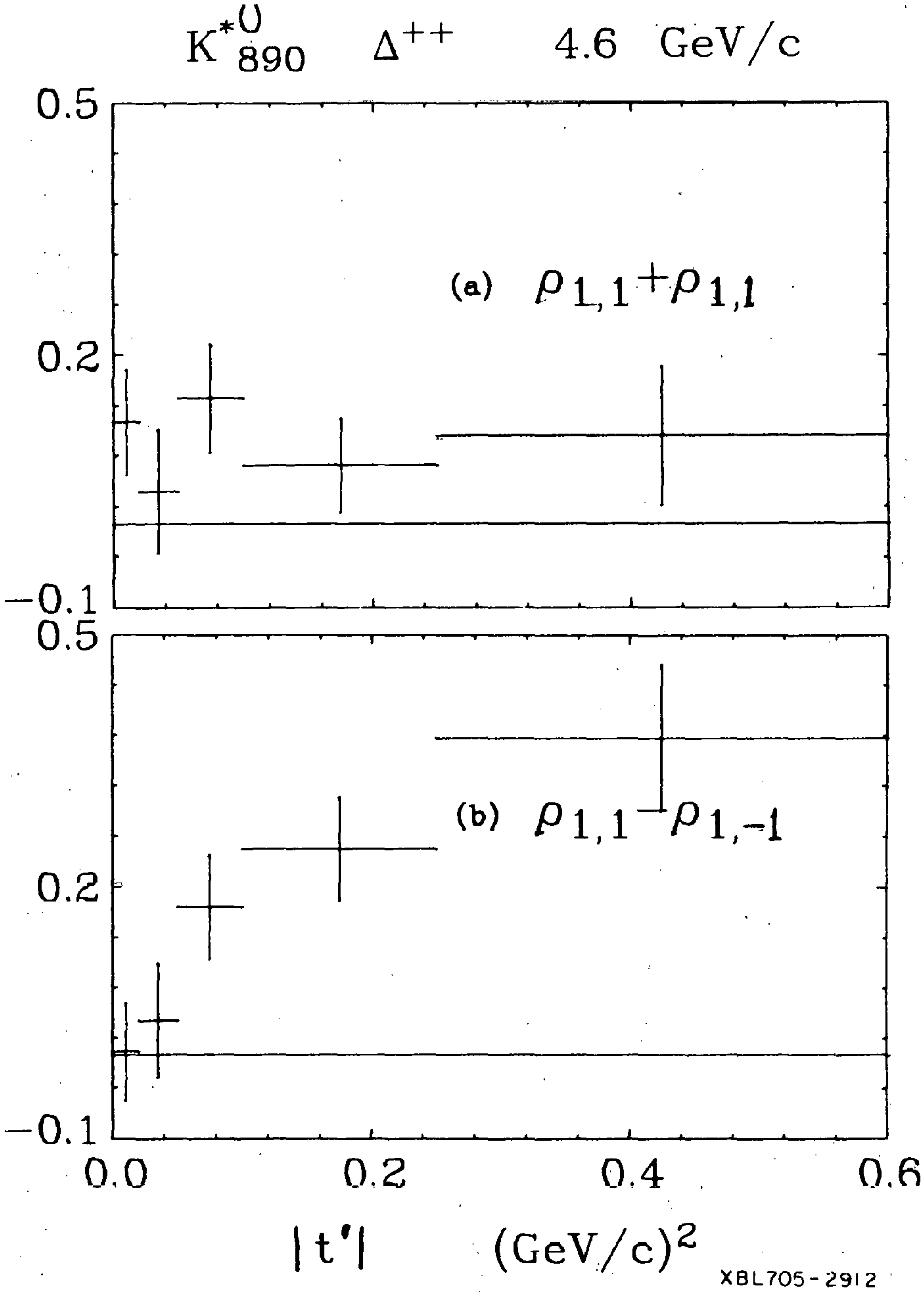

K^{*0}_{890} Δ^{++} 4.6 GeV/c
0.5
0.2
−0.1
(a) $\rho_{1,1}+\rho_{1,1}$
0.5
0.2
−0.1
(b) $\rho_{1,1}-\rho_{1,-1}$
0.0
0.2
0.4
0.6
$|t'|$ $(\mathrm{GeV}/c)^2$
XBL705-2912

Fig. 32

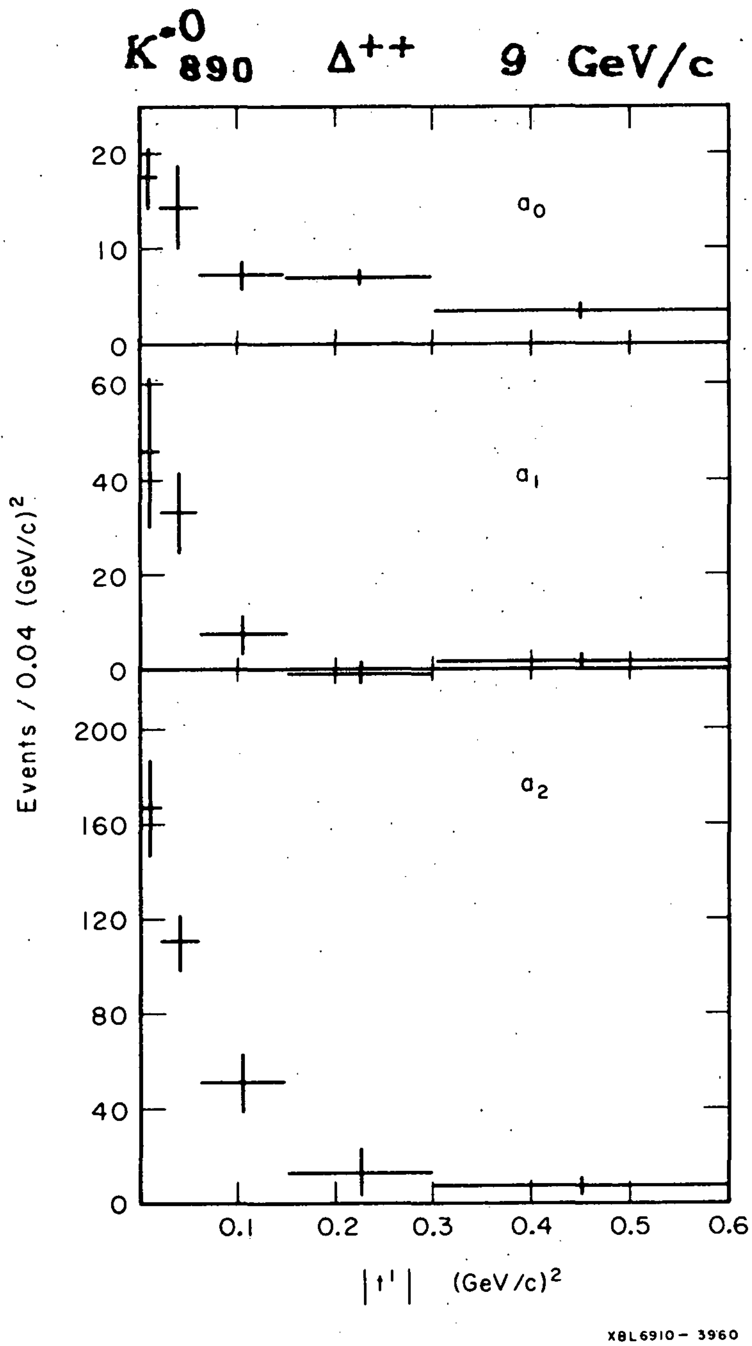

K^{*0}_{890} Δ^{++} 9 GeV/c
a_0
a_1
a_2
Events / 0.04 (GeV/c)^2
|t'| (GeV/c)^2
0.1
0.2
0.3
0.4
0.5
0.6
XBL6910-3960

Fig. 33

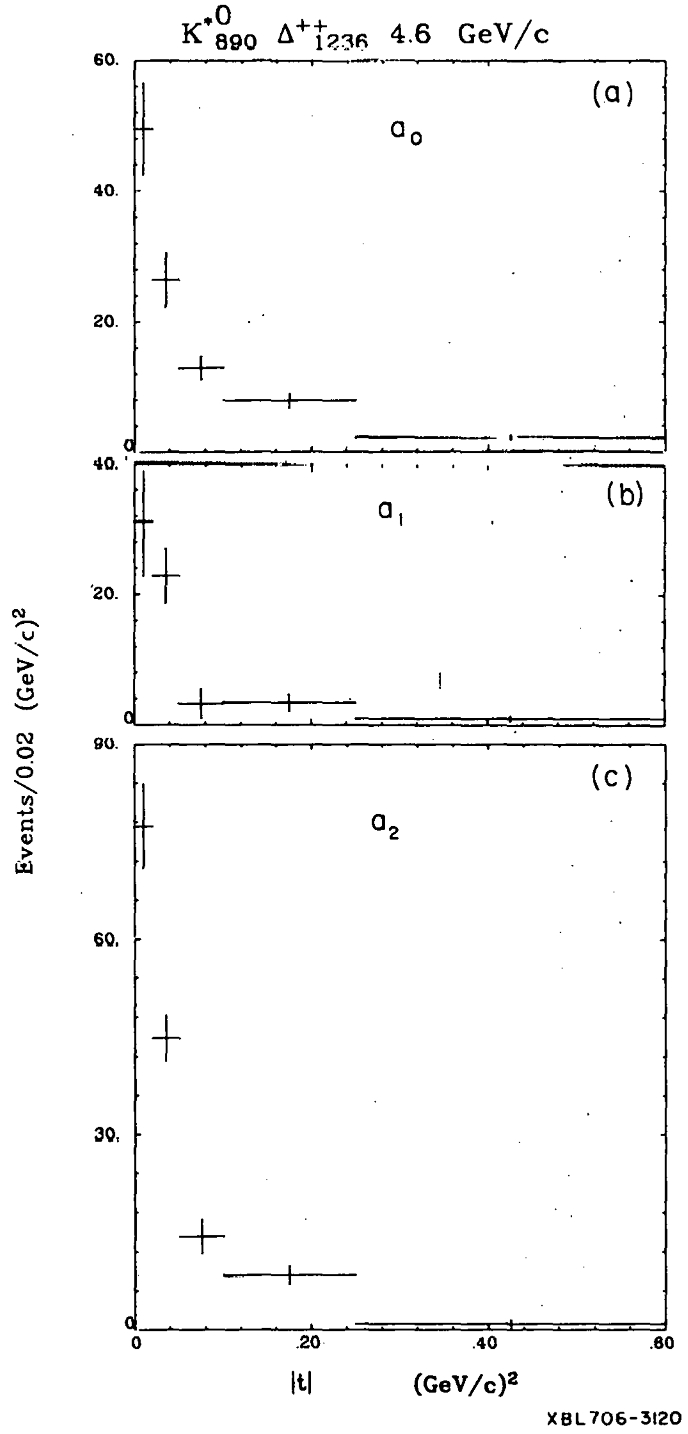

K^{*0}_{890} Δ^{++}_{1236} 4.6 GeV/c
(a)
a_0
(b)
a_1
(c)
a_2
60.
40.
20.
0
40.
20.
0
90.
60.
30.
0
0
.20
.40
.60
Events/0.02 (GeV/c)²
|t| (GeV/c)²
XBL 706-3120

Fig. 34

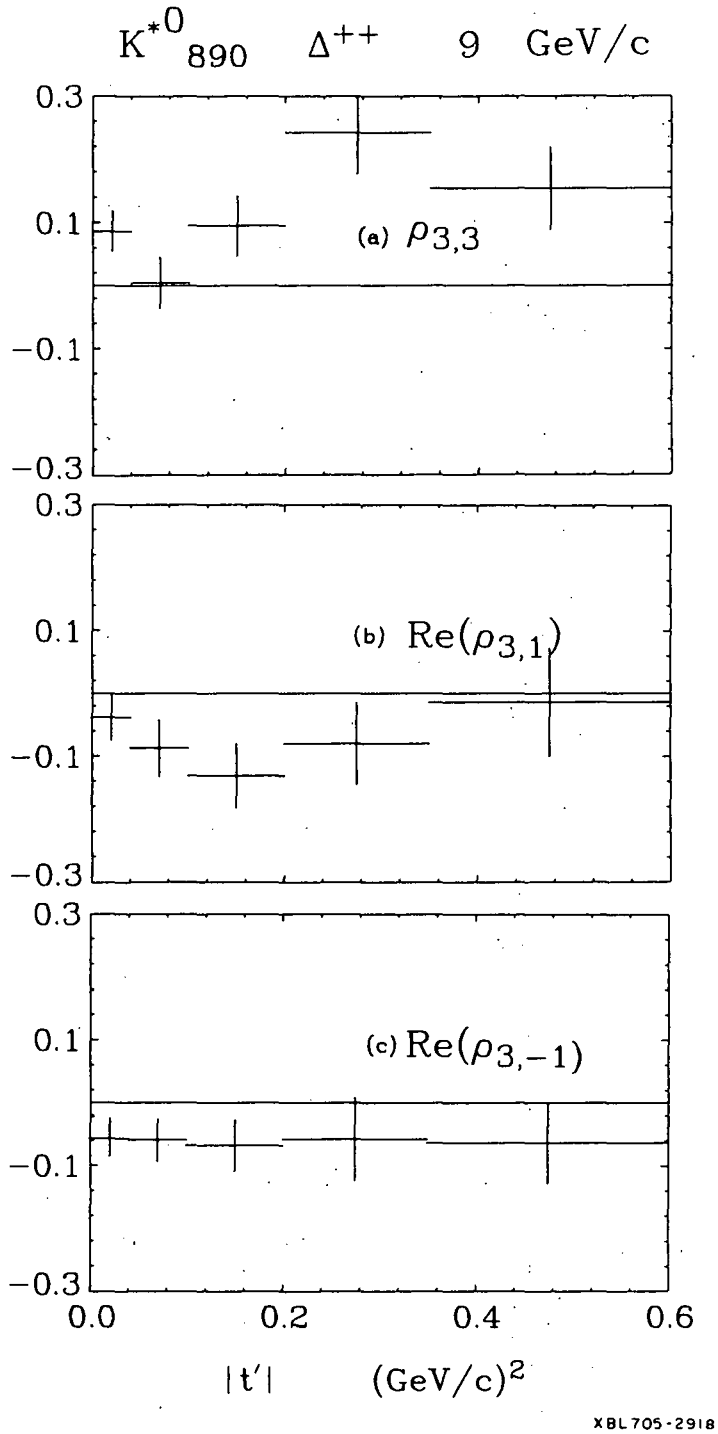

K^{*0}_{890} Δ^{++} 9 GeV/c
0.3
0.1
−0.1
−0.3
(a) $\rho_{3,3}$
(b) $Re(\rho_{3,1})$
(c) $Re(\rho_{3,-1})$
0.0
0.2
0.4
0.6
|t'| (GeV/c)^2
XBL 705-2918

Fig. 35

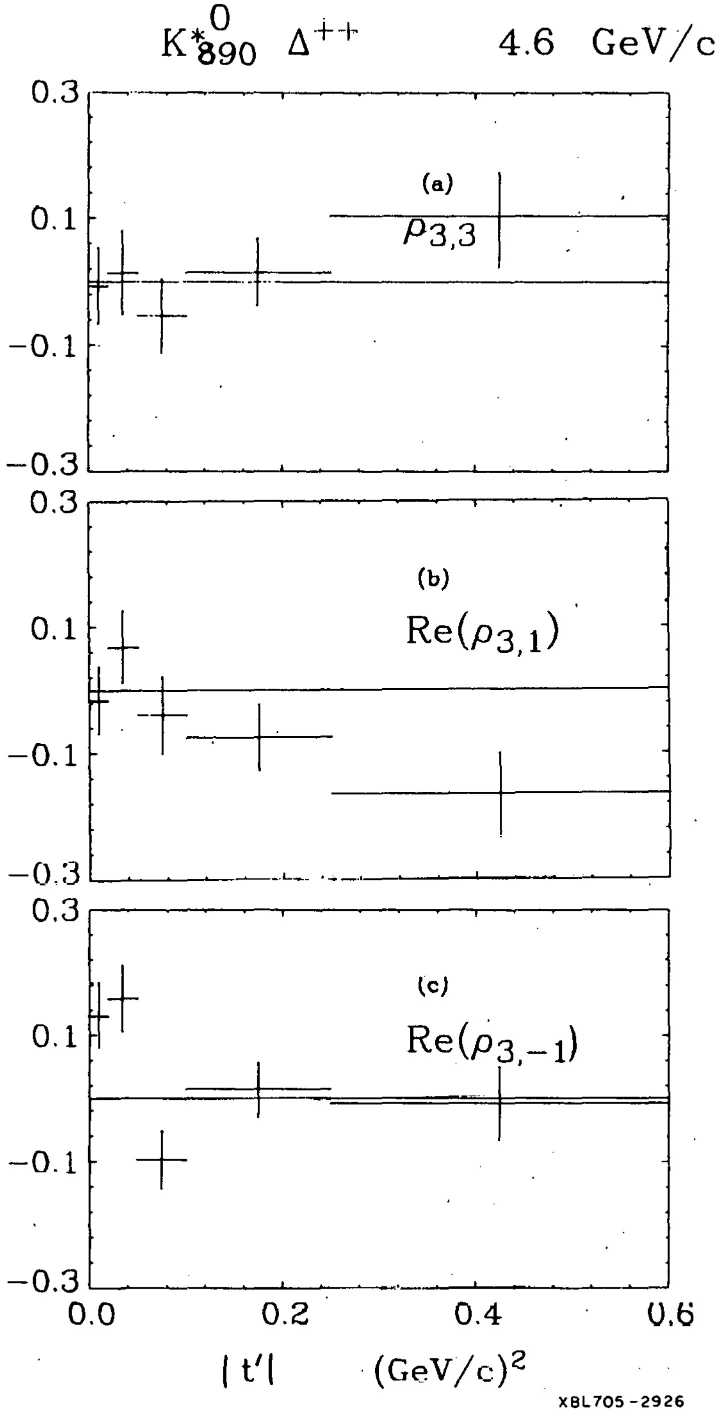

K^{*0}_{890} Δ^{++} 4.6 GeV/c
0.3
0.1
−0.1
−0.3
(a)
$\rho_{3,3}$
(b)
$\mathrm{Re}(\rho_{3,1})$
(c)
$\mathrm{Re}(\rho_{3,-1})$
0.0
0.2
0.4
0.6
$|t'|$ $(\mathrm{GeV}/c)^2$
XBL705-2926

Fig. 36

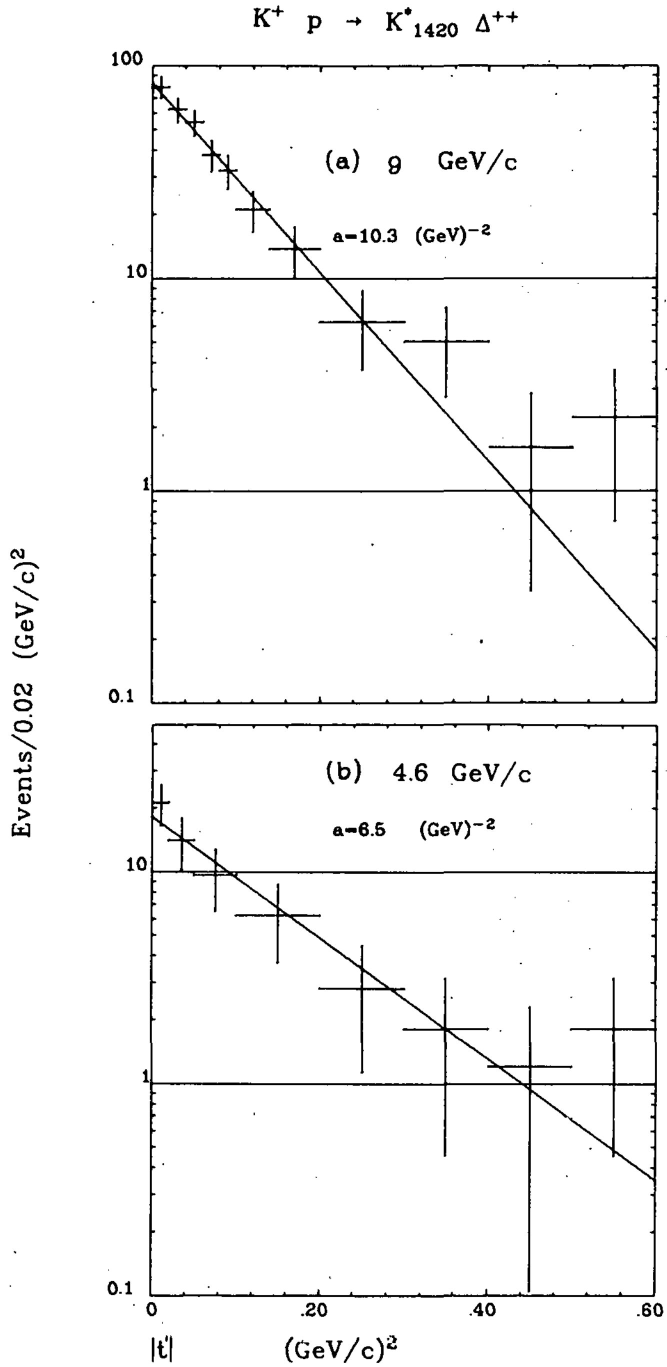

XBL706-3116

Fig. 37

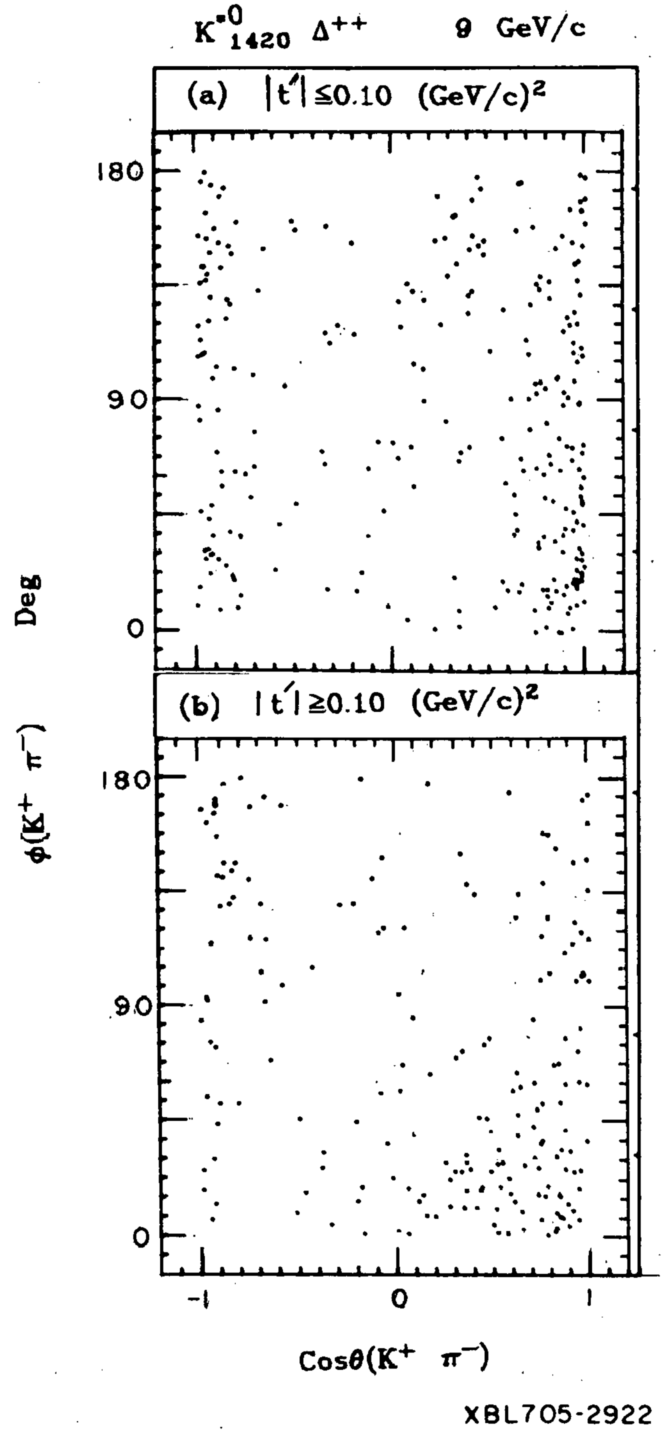
K*0 1420 Δ++ 9 GeV/c
(a) |t′| ≤0.10 (GeV/c)²
(b) |t′| ≥0.10 (GeV/c)²
180
90
0
φ(K+ π−) Deg
-1
0
1
Cosθ(K+ π−)
XBL705-2922

Fig. 38

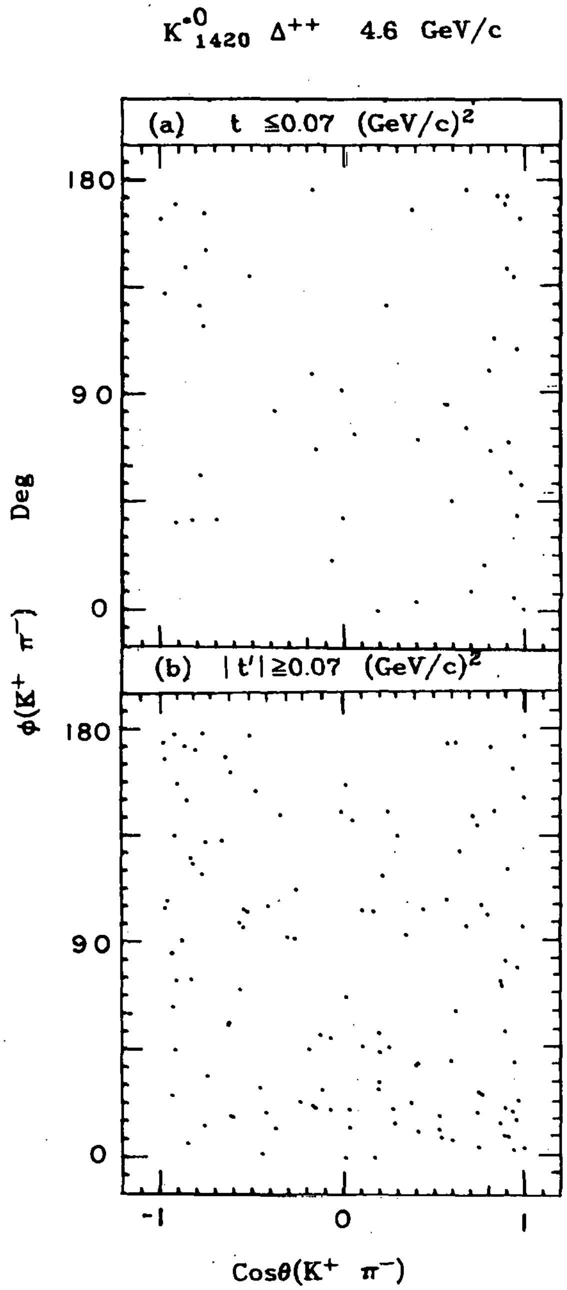

XBL705-2920

Fig. 39

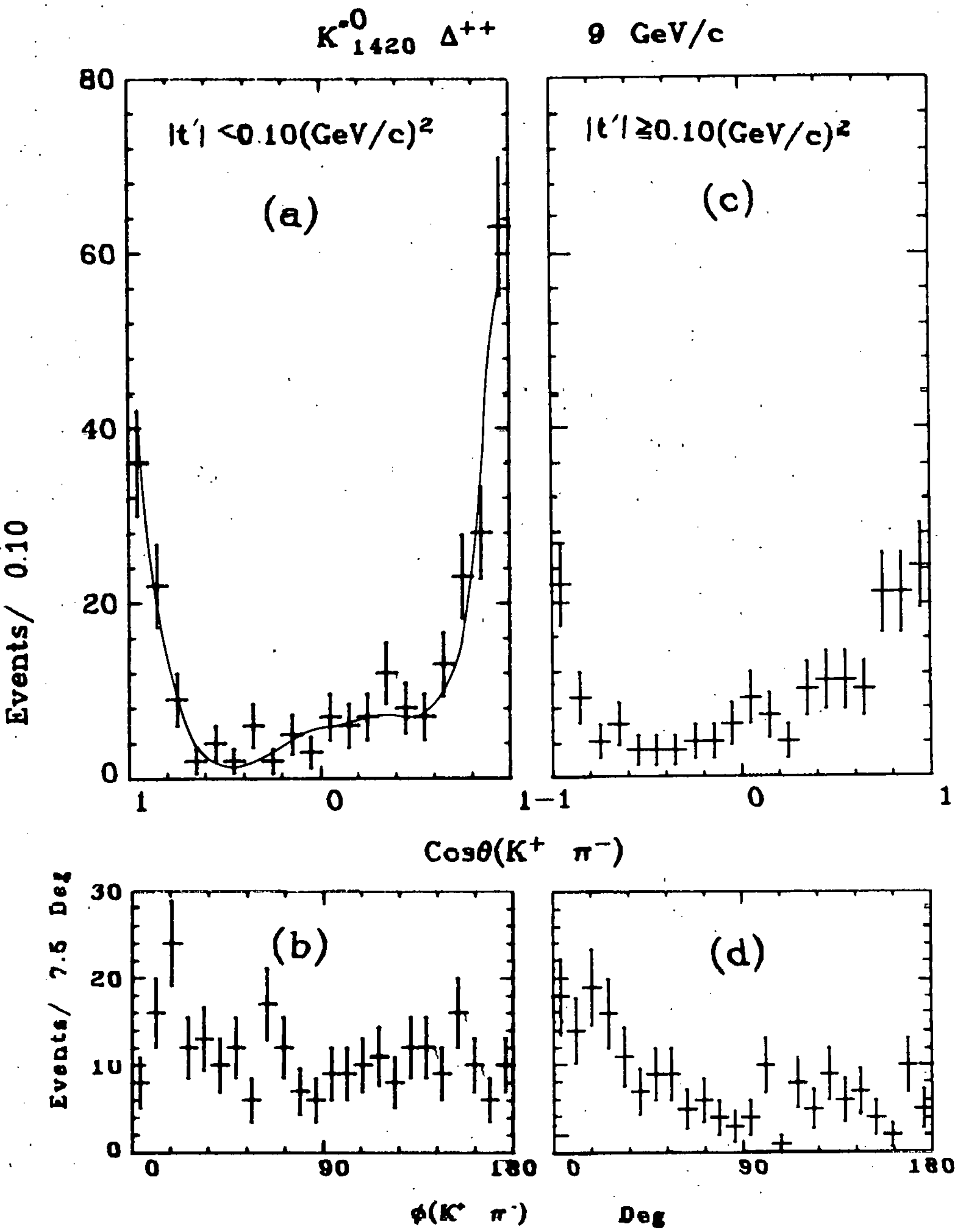

XBL 705-2915

Fig. 40

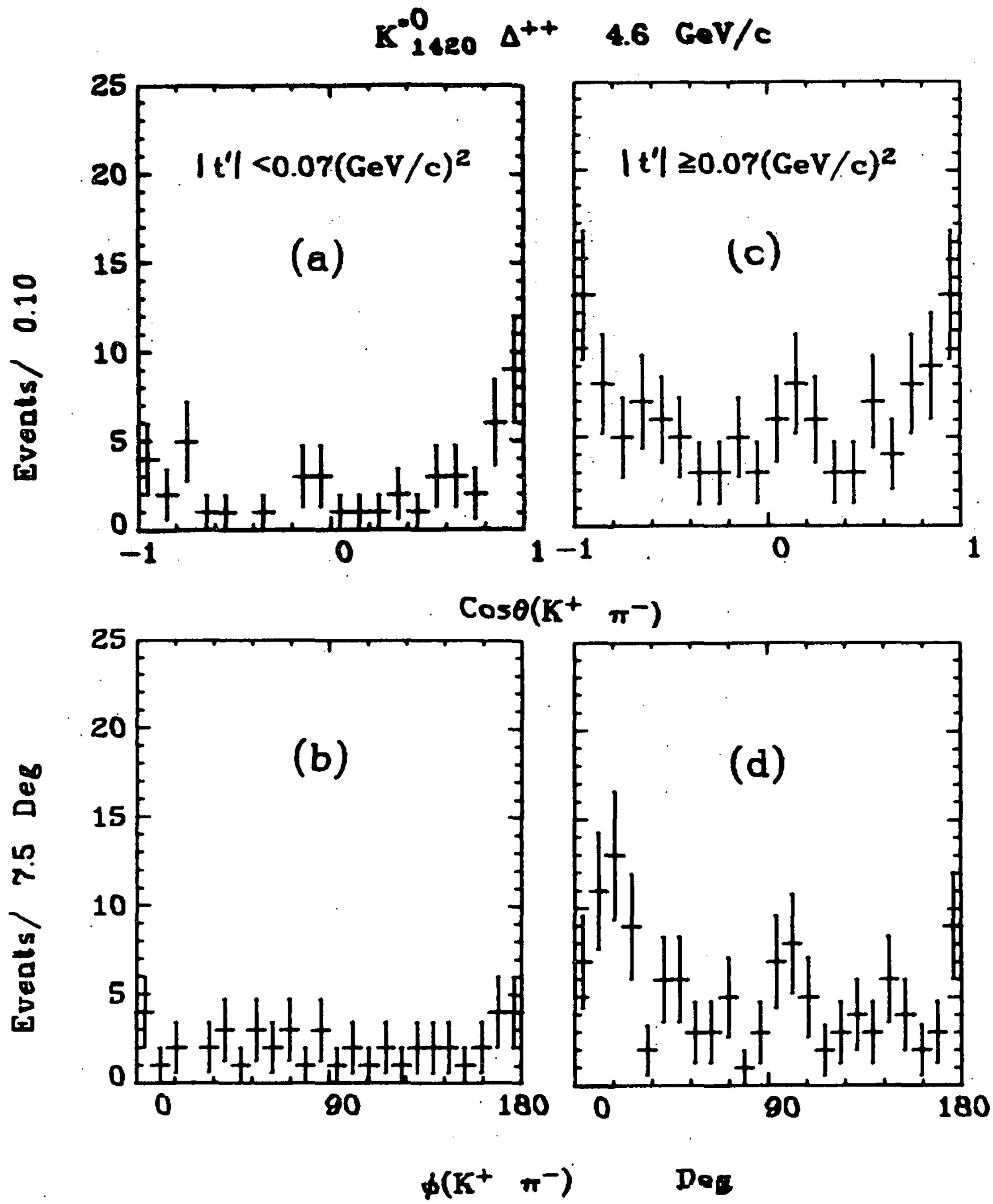

XBL705-2911

Fig. 41

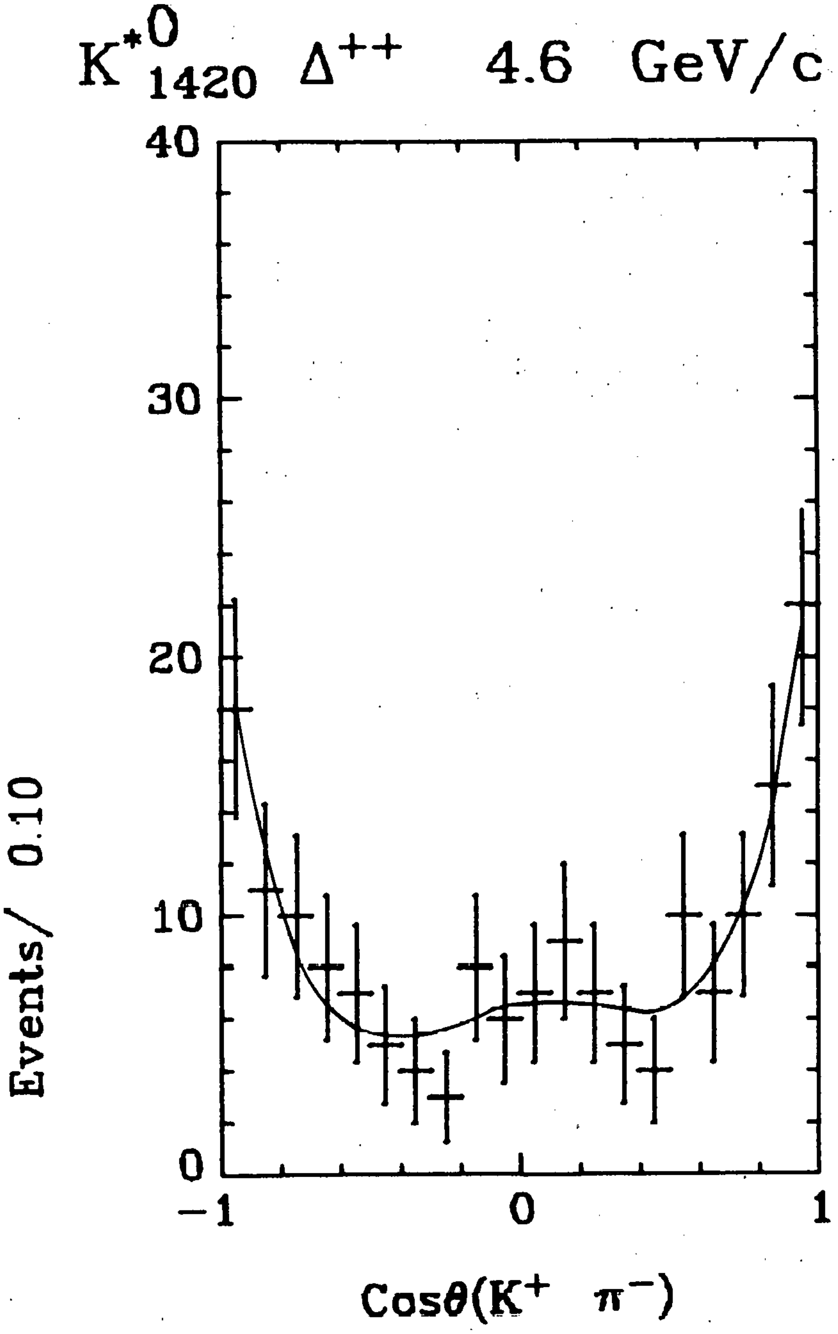

XBL706-3187

Fig. 42

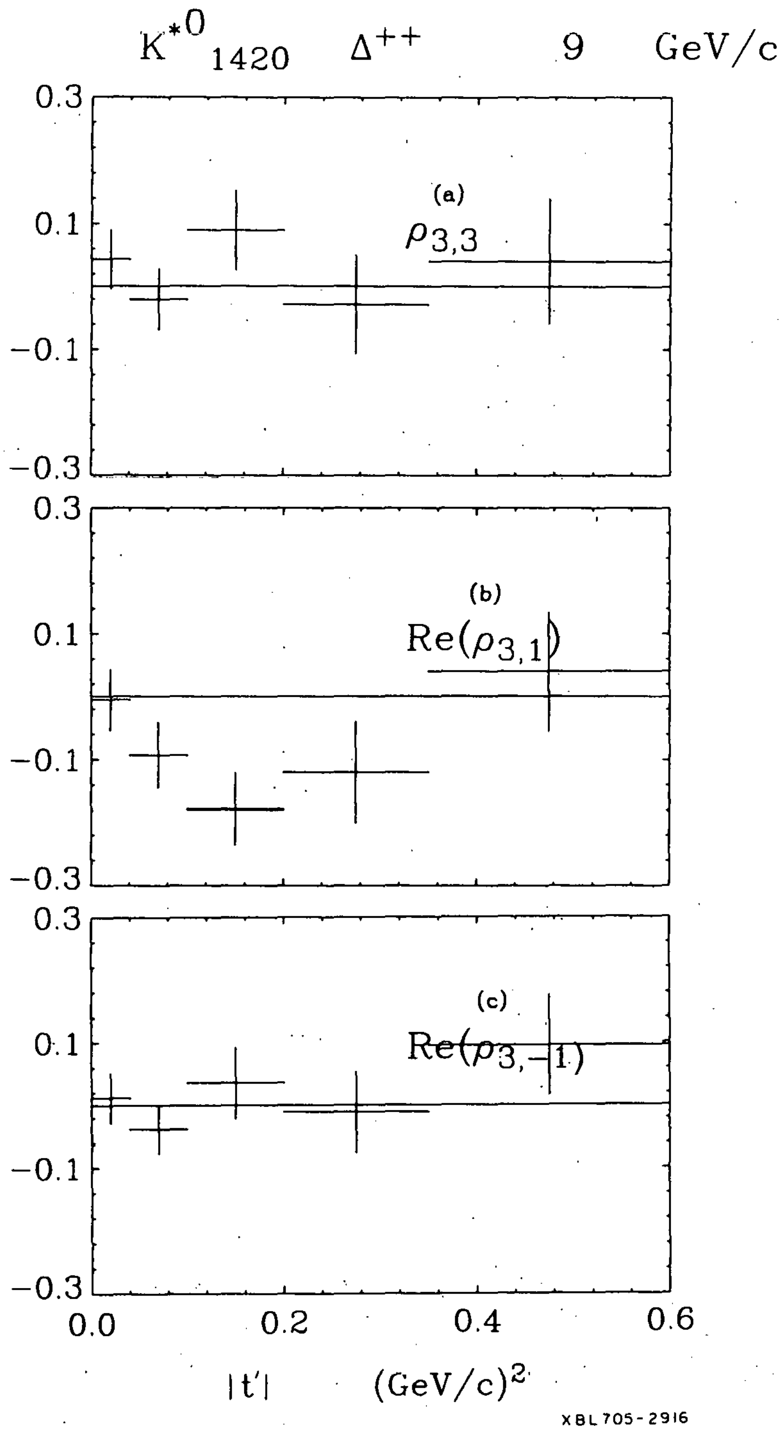
K*0 1420 Δ++ 9 GeV/c
0.3
0.1
−0.1
−0.3
(a)
ρ3,3
(b)
Re(ρ3,1)
(c)
Re(ρ3,−1)
0.0
0.2
0.4
0.6
|t'| (GeV/c)2
XBL 705-2916

Fig. 43

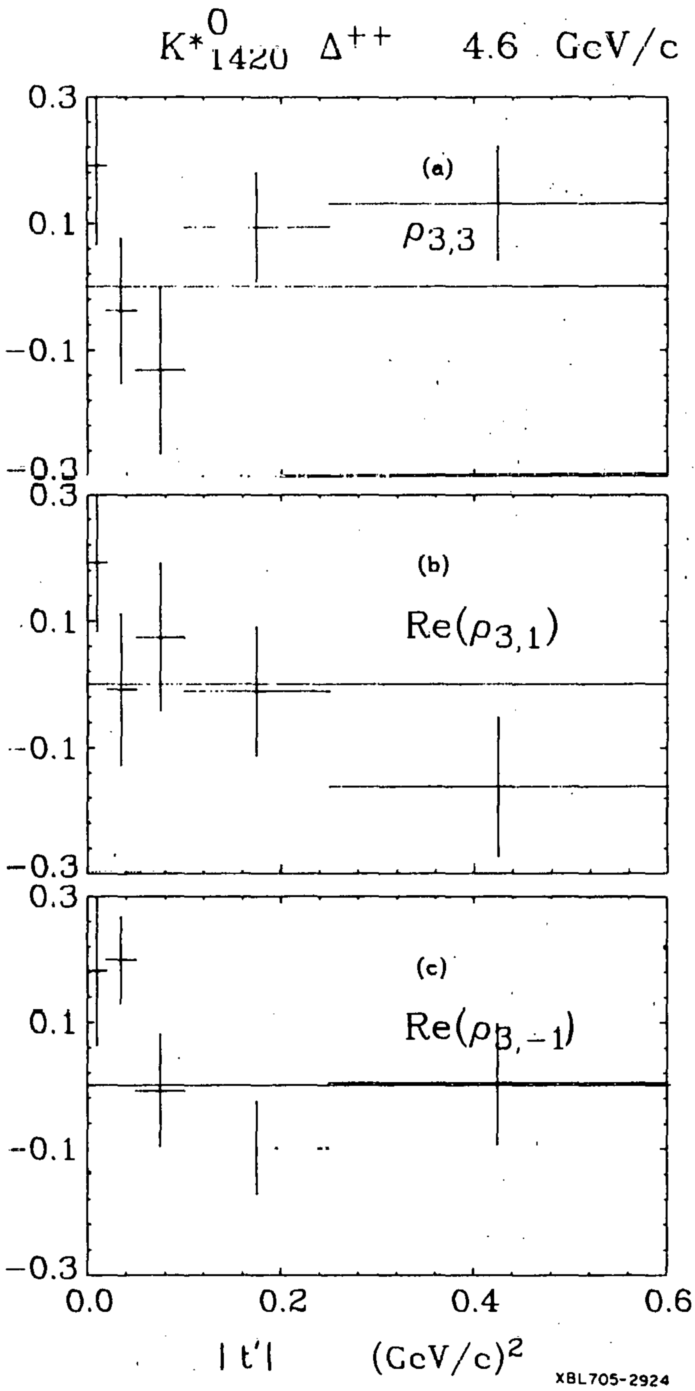

K^{*0}_{1420} Δ^{++} 4.6 GeV/c
(a)
$\rho_{3,3}$
(b)
$Re(\rho_{3,1})$
(c)
$Re(\rho_{3,-1})$
0.3
0.1
−0.1
−0.3
0.0
0.2
0.4
0.6
|t'| (GeV/c)^2
XBL705-2924

Fig. 44

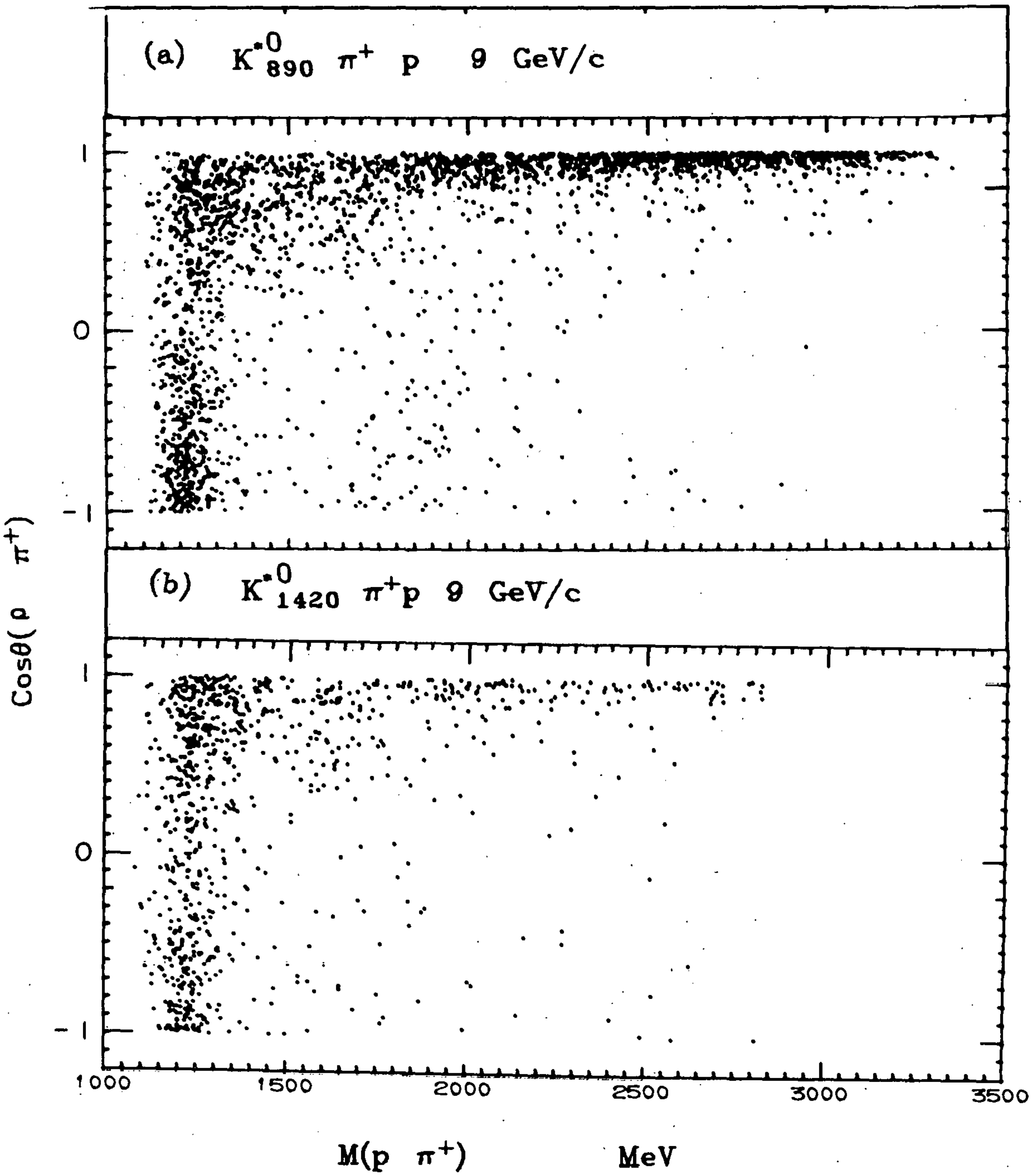

XBL705-2935

Fig. 45

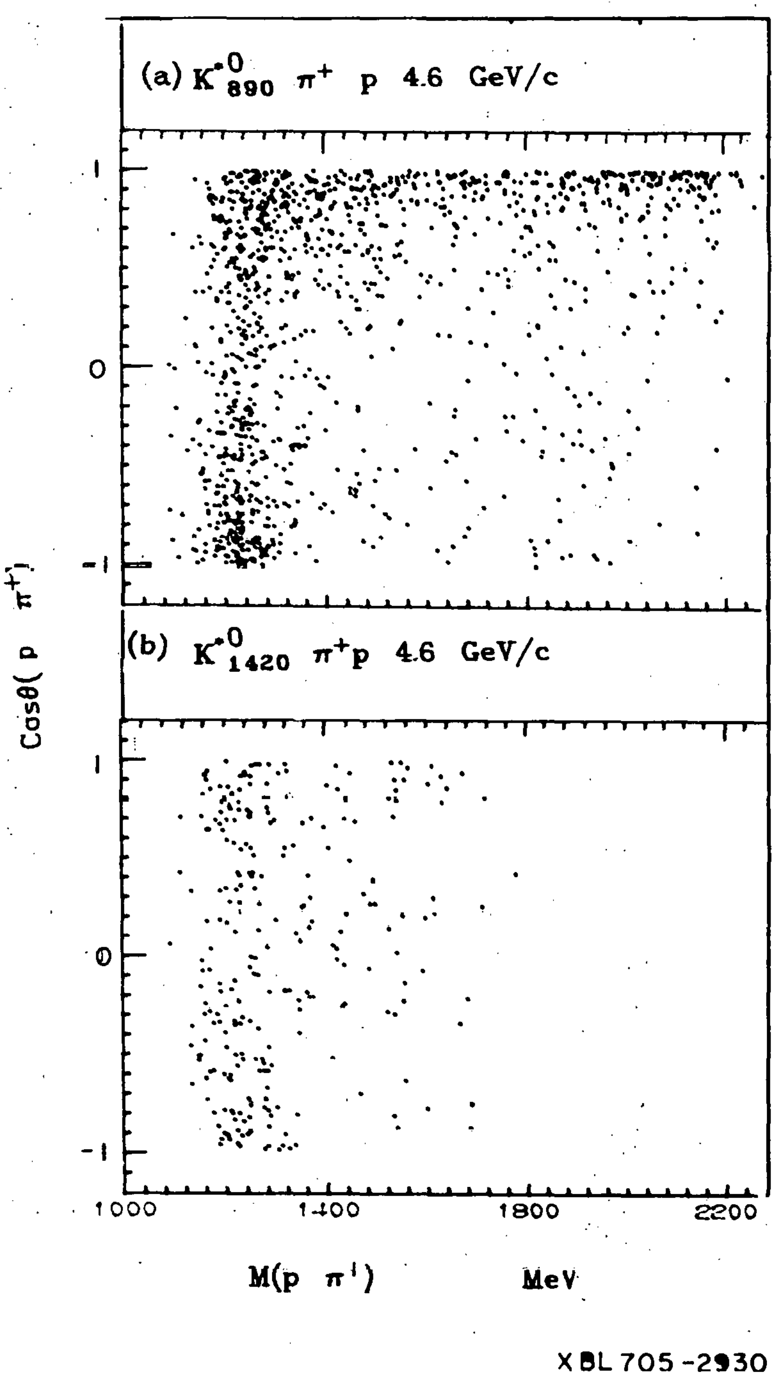

(a) K^{*0}_{890} π^+ p 4.6 GeV/c
(b) K^{*0}_{1420} π^+p 4.6 GeV/c
Cosθ(p π+)
1
0
-1
1000
1400
1800
2200
M(p π+)
MeV
XBL 705-2930

Fig. 46

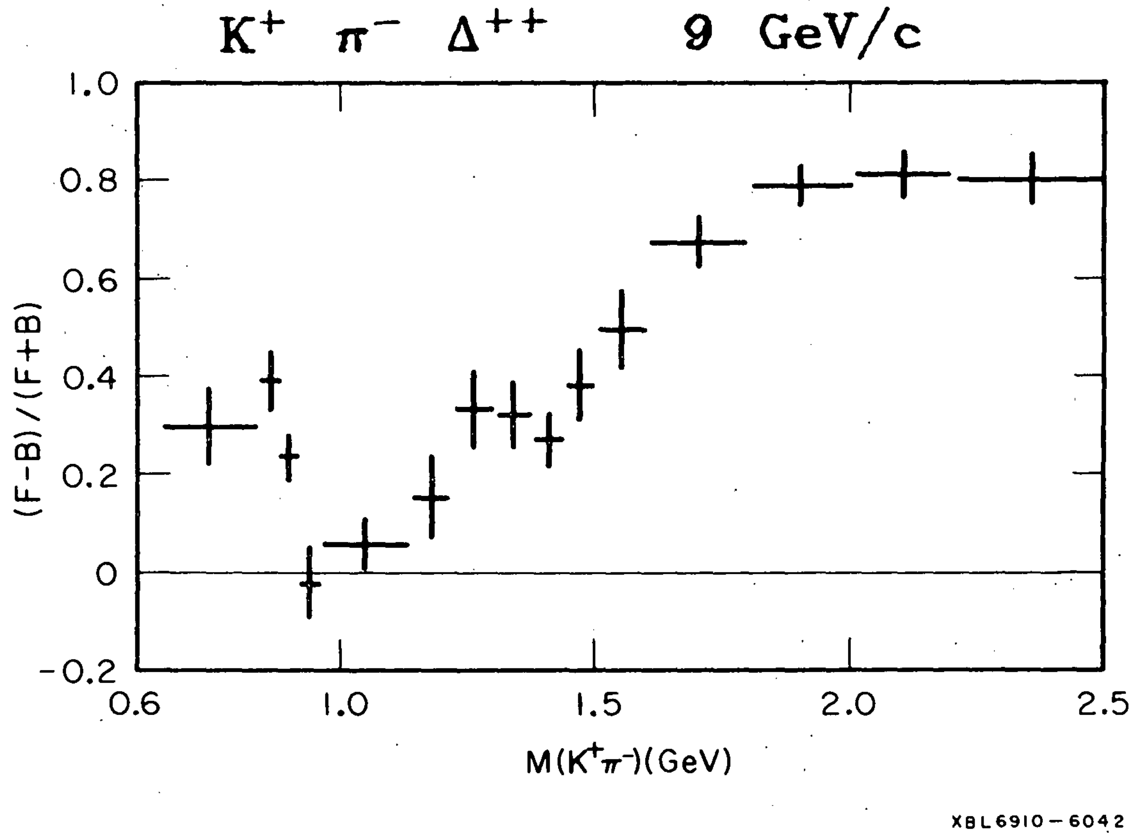

K+ π− Δ++ 9 GeV/c
1.0
0.8
0.6
0.4
0.2
0
-0.2
(F-B)/(F+B)
0.6
1.0
1.5
2.0
2.5
M(K+π−)(GeV)
XBL 6910-6042

Fig. 47

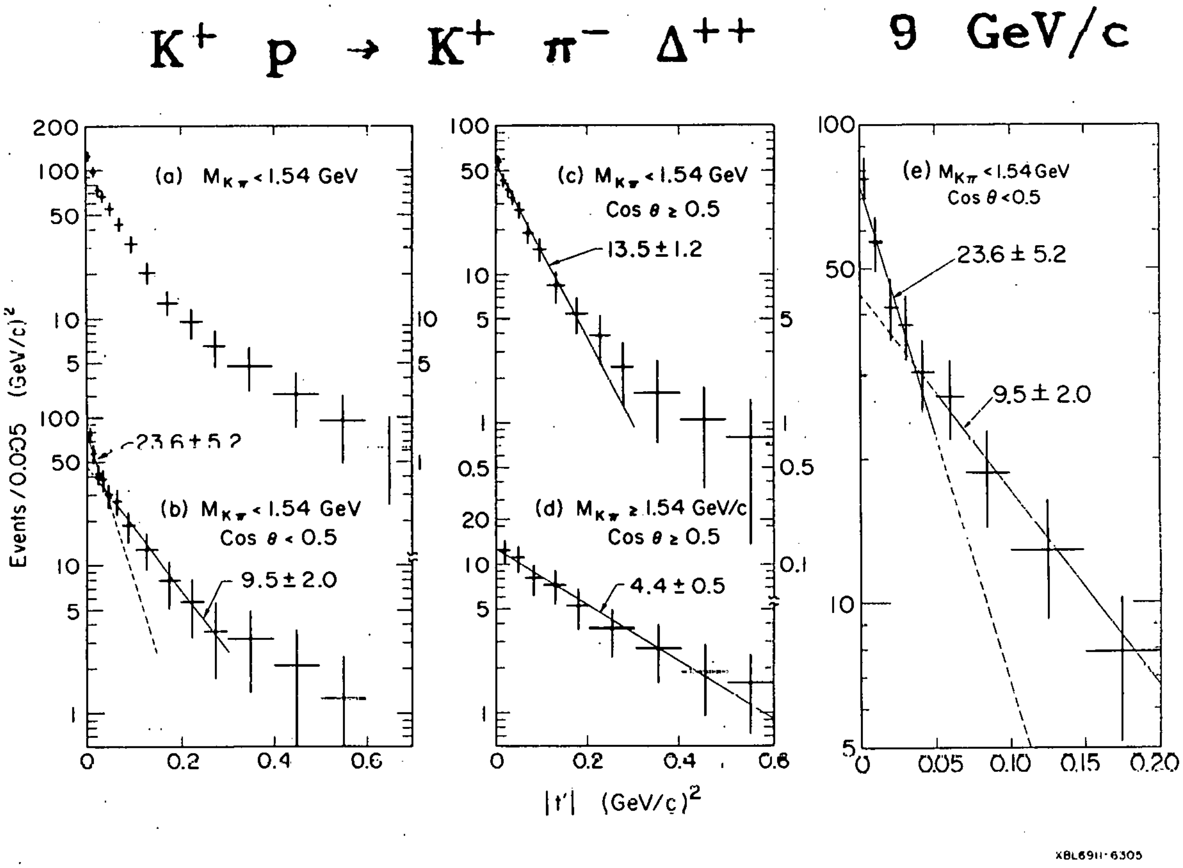
K+ p → K+ π− Δ++ 9 GeV/c
(a) MKπ < 1.54 GeV
(b) MKπ < 1.54 GeV
Cos θ < 0.5
23.6 ± 5.2
9.5 ± 2.0
(c) MKπ < 1.54 GeV
Cos θ ≥ 0.5
13.5 ± 1.2
(d) MKπ ≥ 1.54 GeV/c
Cos θ ≥ 0.5
4.4 ± 0.5
(e) MKπ < 1.54 GeV
Cos θ < 0.5
23.6 ± 5.2
9.5 ± 2.0
Events / 0.005 (GeV/c)²
|t'| (GeV/c)²
XBL6911-6305

Fig. 48

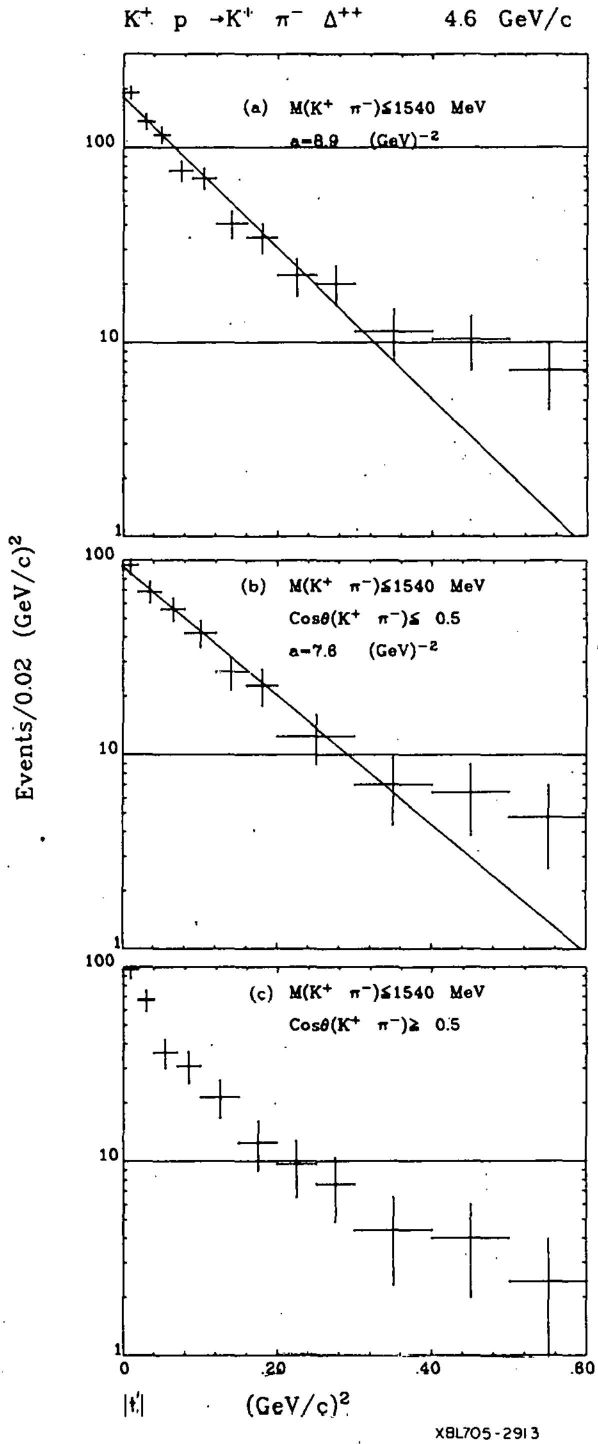
K+ p →K+ π− Δ++ 4.6 GeV/c
(a) M(K+ π−)≤1540 MeV
a=8.9 (GeV)−2
(b) M(K+ π−)≤1540 MeV
Cosθ(K+ π−)≤ 0.5
a=7.6 (GeV)−2
(c) M(K+ π−)≤1540 MeV
Cosθ(K+ π−)≥ 0.5
Events/0.02 (GeV/c)2
100
10
1
0
.20
.40
.80
|t'| (GeV/c)2
XBL705-2913

Fig. 49

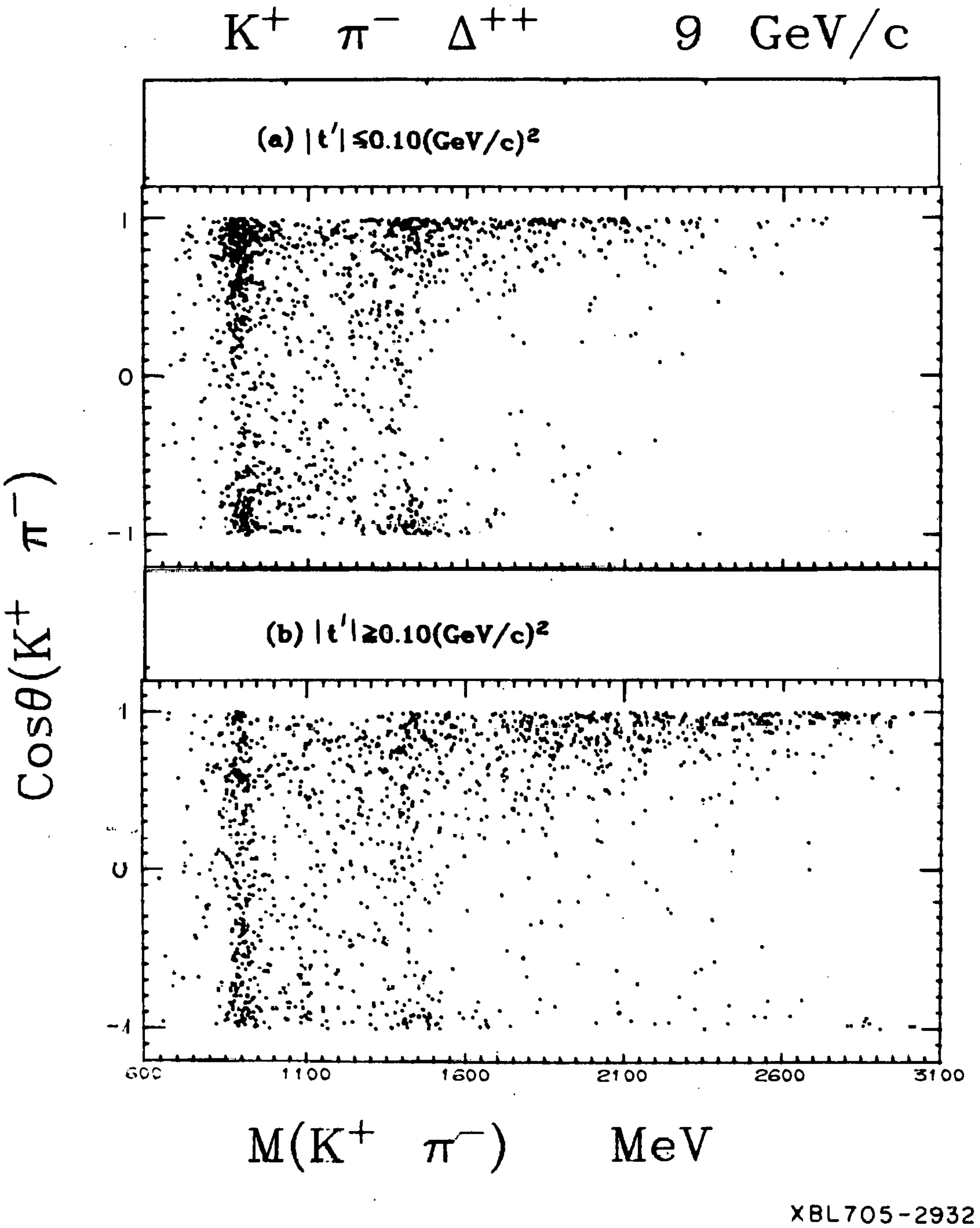

$K^+ \ \pi^- \ \Delta^{++}$ 9 GeV/c
(a) $|t'| \leq 0.10 (GeV/c)^2$
(b) $|t'| \geq 0.10 (GeV/c)^2$
$Cos\theta(K^+ \ \pi^-)$
1
0
-1
600
1100
1600
2100
2600
3100
$M(K^+ \ \pi^-)$ MeV
XBL705-2932

Fig. 50

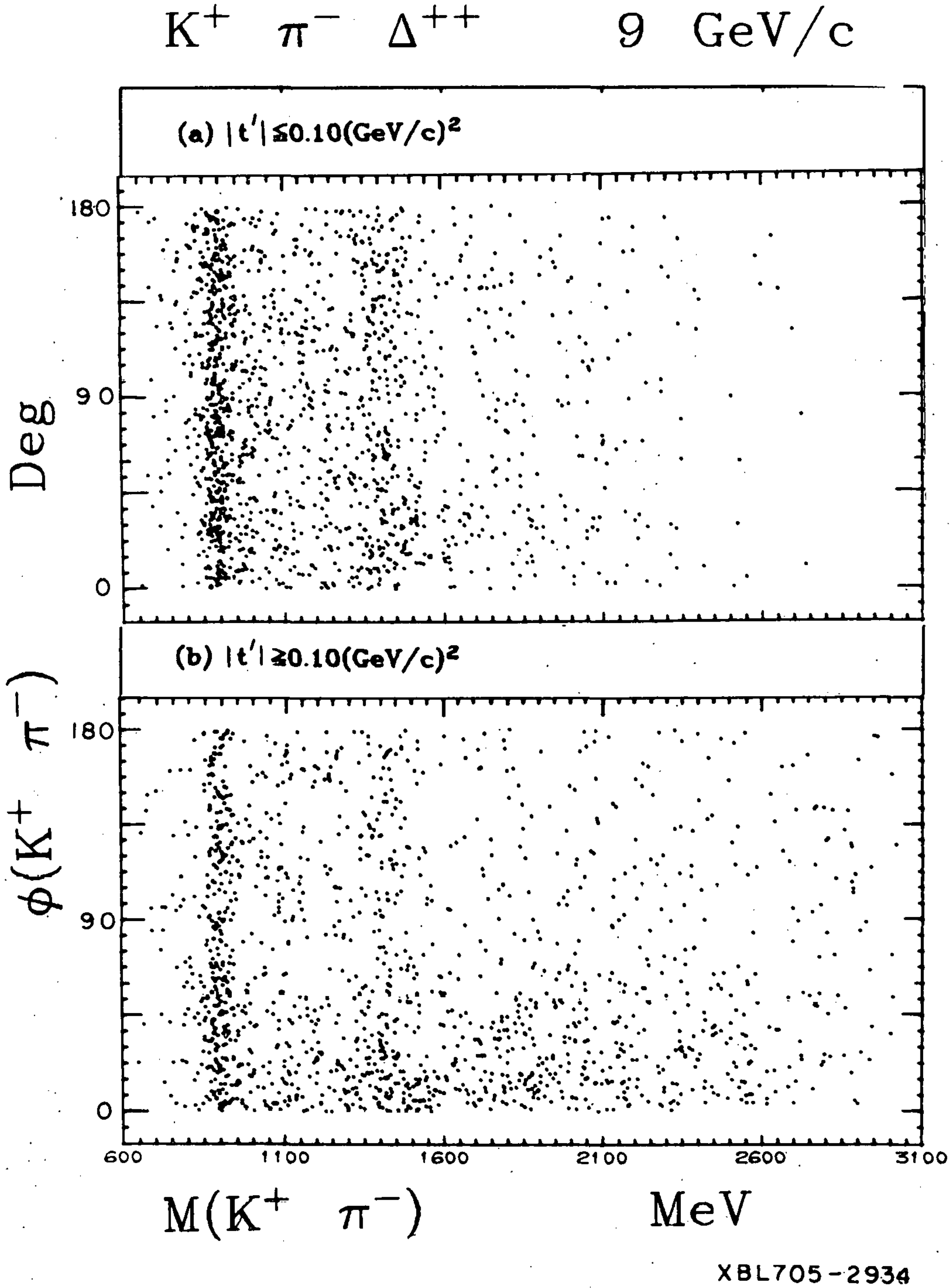

$K^+ \pi^- \Delta^{++}$ 9 GeV/c
(a) $|t'| \leq 0.10 (GeV/c)^2$
(b) $|t'| \geq 0.10 (GeV/c)^2$
180
90
0
$\phi(K^+ \pi^-)$ Deg
600
1100
1600
2100
2600
3100
$M(K^+ \pi^-)$ MeV
XBL705-2934

Fig. 51

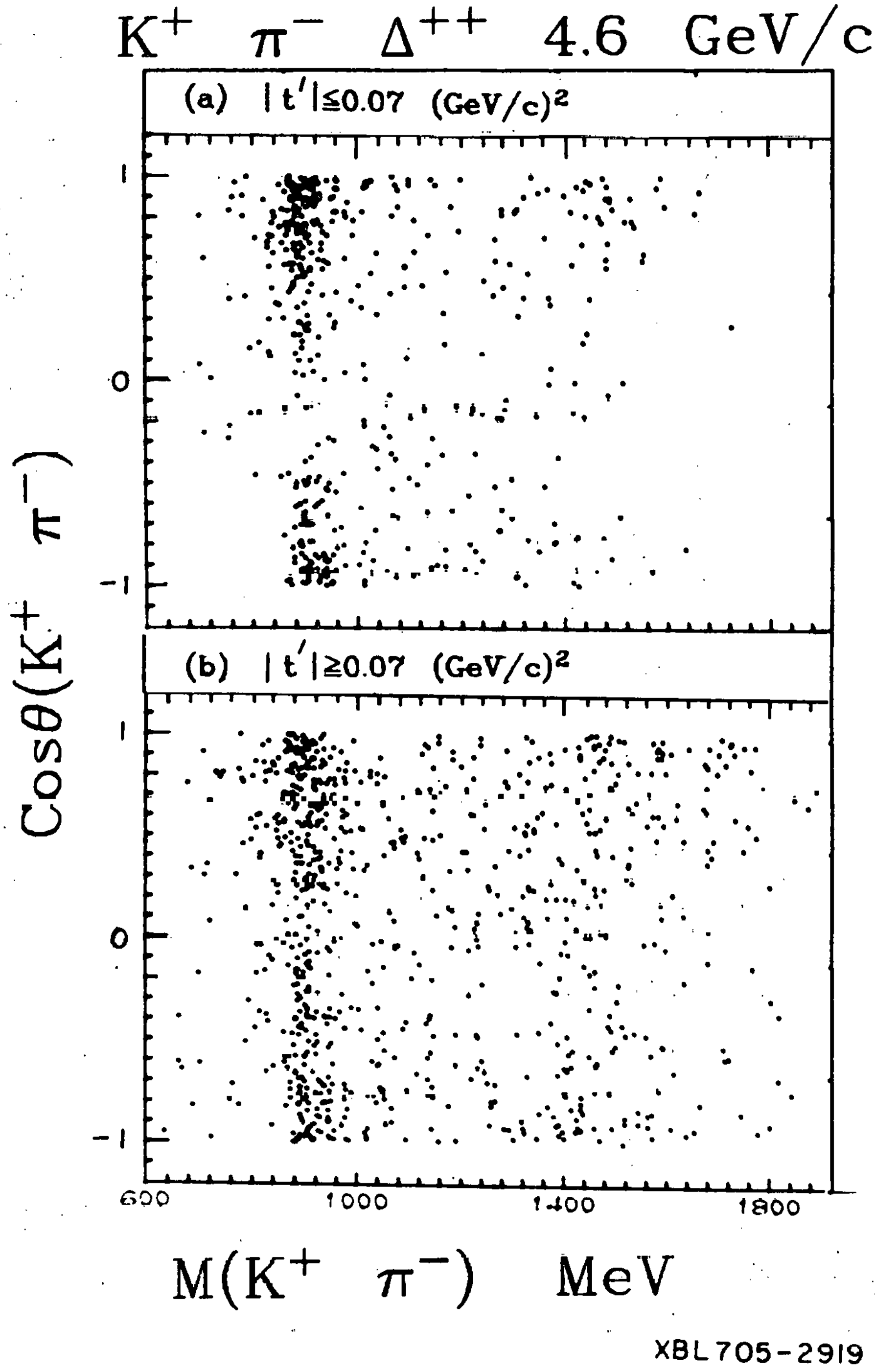

K+ π− Δ++ 4.6 GeV/c
(a) |t′|≦0.07 (GeV/c)²
(b) |t′|≧0.07 (GeV/c)²
Cosθ(K+ π−)
1
0
-1
600
1000
1400
1800
M(K+ π−) MeV
XBL 705-2919

Fig. 52

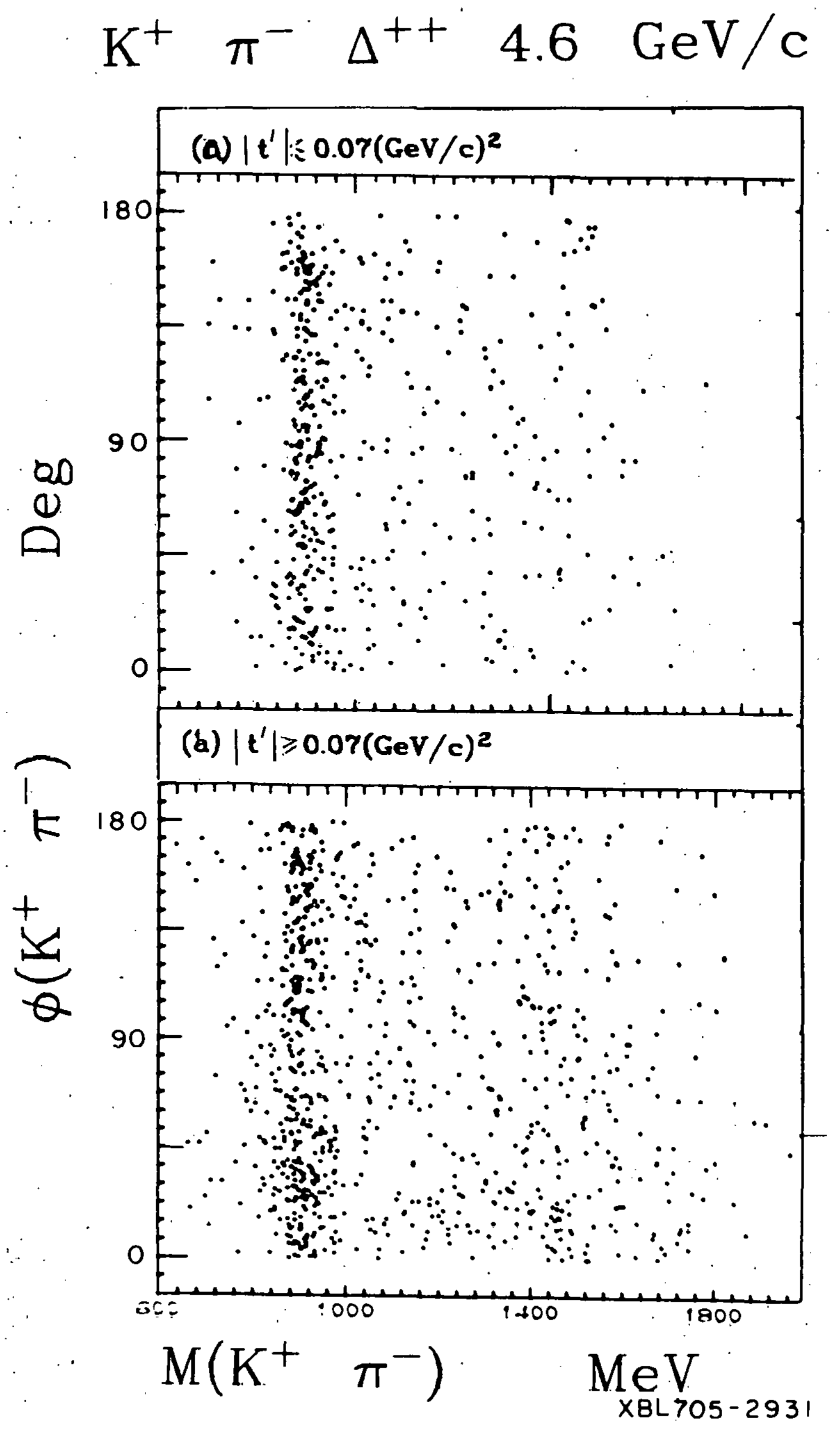

$K^+ \pi^- \Delta^{++}$ 4.6 GeV/c
(a) $|t'| \lesssim 0.07 (GeV/c)^2$
(b) $|t'| \geq 0.07 (GeV/c)^2$
180
90
0
Deg
$\phi(K^+ \pi^-)$
1000
1400
1800
$M(K^+ \pi^-)$ MeV
XBL705-2931

Fig. 53

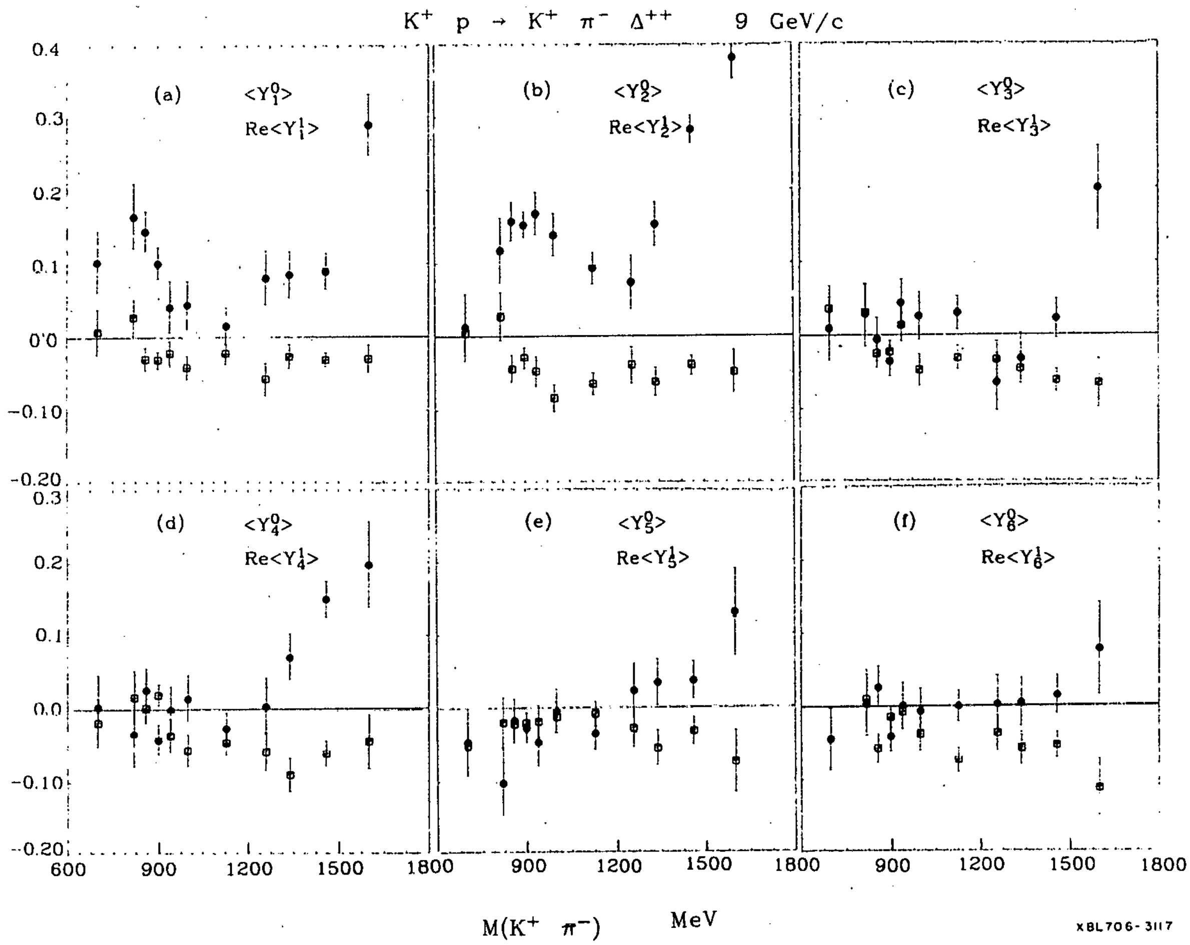

K+ p → K+ π− Δ++ 9 GeV/c
(a) <Y$_1^0$> Re<Y$_1^1$>
(b) <Y$_2^0$> Re<Y$_2^1$>
(c) <Y$_3^0$> Re<Y$_3^1$>
(d) <Y$_4^0$> Re<Y$_4^1$>
(e) <Y$_5^0$> Re<Y$_5^1$>
(f) <Y$_6^0$> Re<Y$_6^1$>
0.4
0.3
0.2
0.1
0.0
−0.10
−0.20
600 900 1200 1500 1800
M(K+ π−) MeV
XBL706-3117

Fig. 54

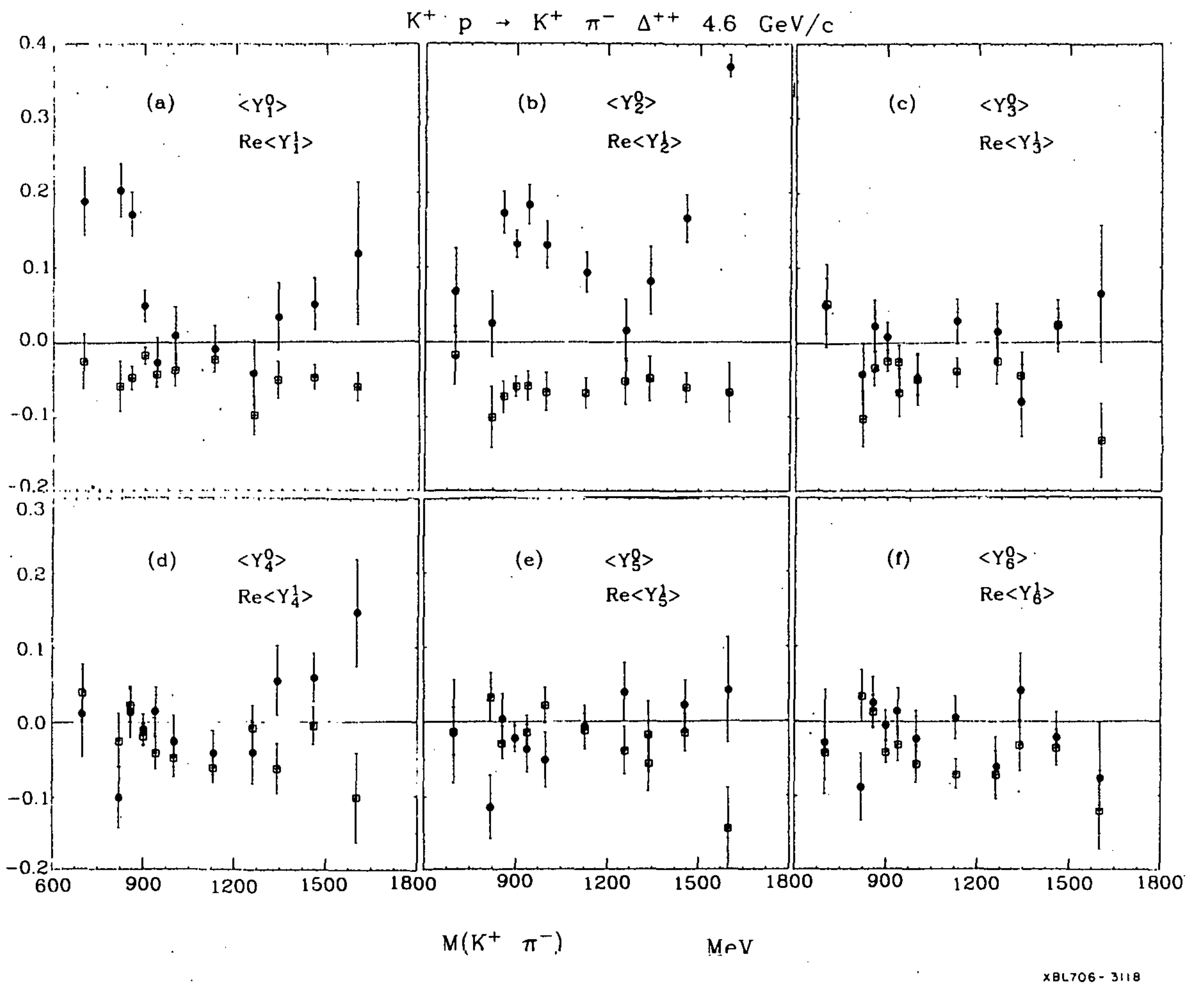

K+ p → K+ π− Δ++ 4.6 GeV/c
(a) <Y$_1^0$> Re<Y$_1^1$>
(b) <Y$_2^0$> Re<Y$_2^1$>
(c) <Y$_3^0$> Re<Y$_3^1$>
(d) <Y$_4^0$> Re<Y$_4^1$>
(e) <Y$_5^0$> Re<Y$_5^1$>
(f) <Y$_6^0$> Re<Y$_6^1$>
0.4
0.3
0.2
0.1
0.0
-0.1
-0.2
600
900
1200
1500
1800
M(K+ π−) MeV
XBL706-3118

Fig. 55

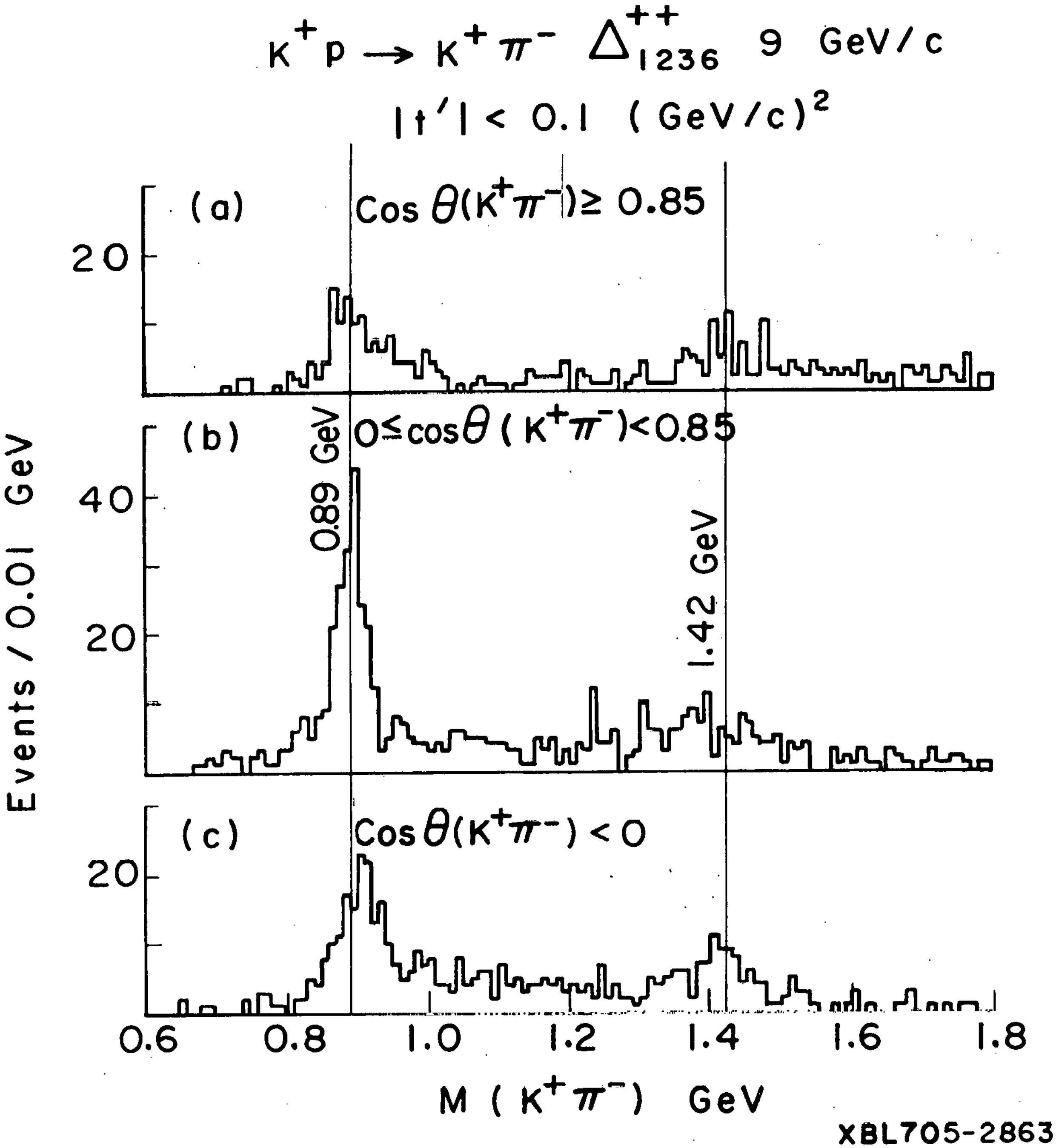

$K^+p \to K^+\pi^- \Delta^{++}_{1236}$ 9 GeV/c
$|t'| < 0.1$ $(GeV/c)^2$
(a)
$\cos\theta(K^+\pi^-) \geq 0.85$
(b)
$0 \leq \cos\theta(K^+\pi^-) < 0.85$
(c)
$\cos\theta(K^+\pi^-) < 0$
0.89 GeV
1.42 GeV
Events / 0.01 GeV
20
40
20
20
0.6
0.8
1.0
1.2
1.4
1.6
1.8
$M(K^+\pi^-)$ GeV
XBL705-2863

Fig. 56

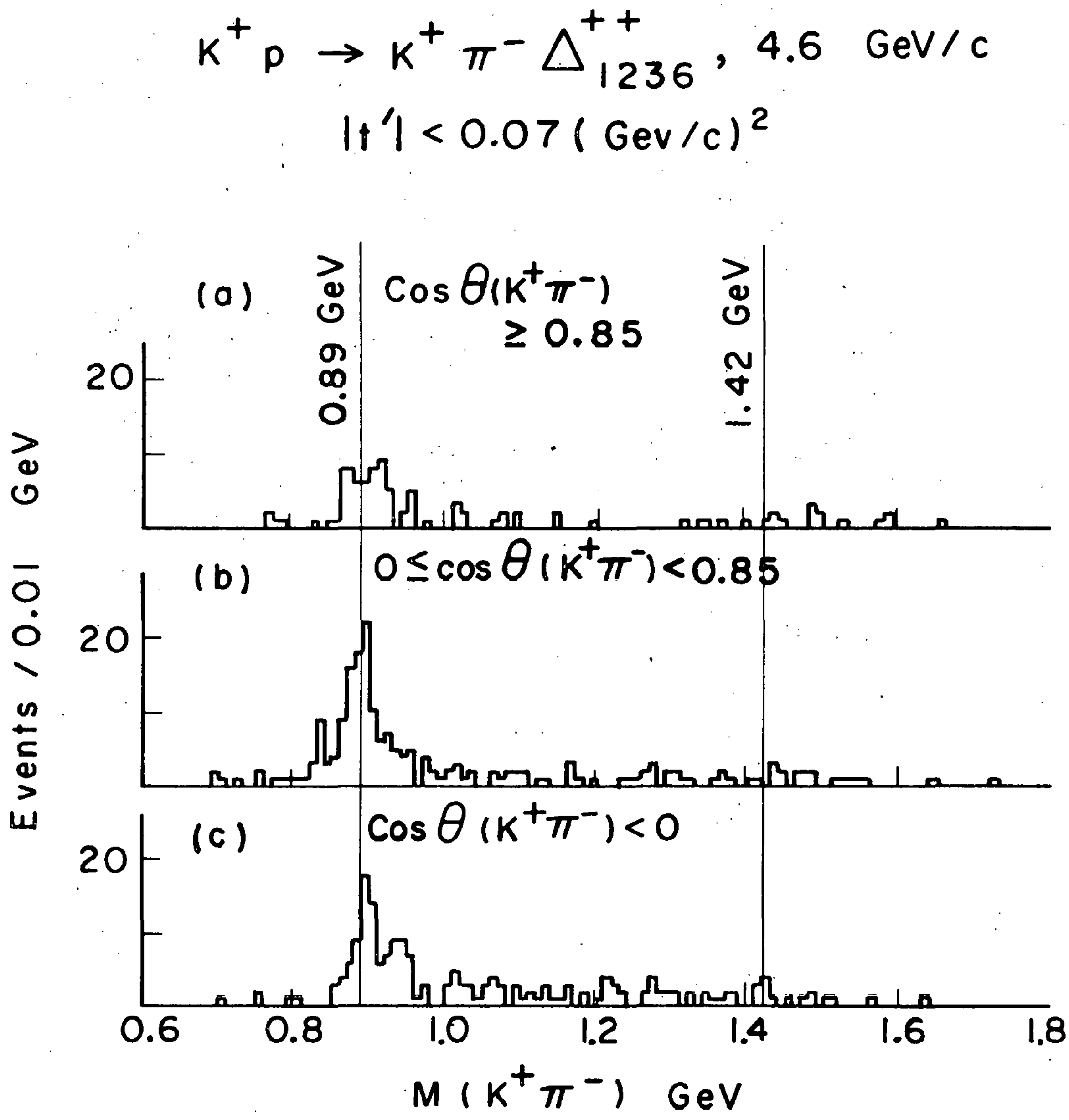

XBL705-2864

Fig. 57

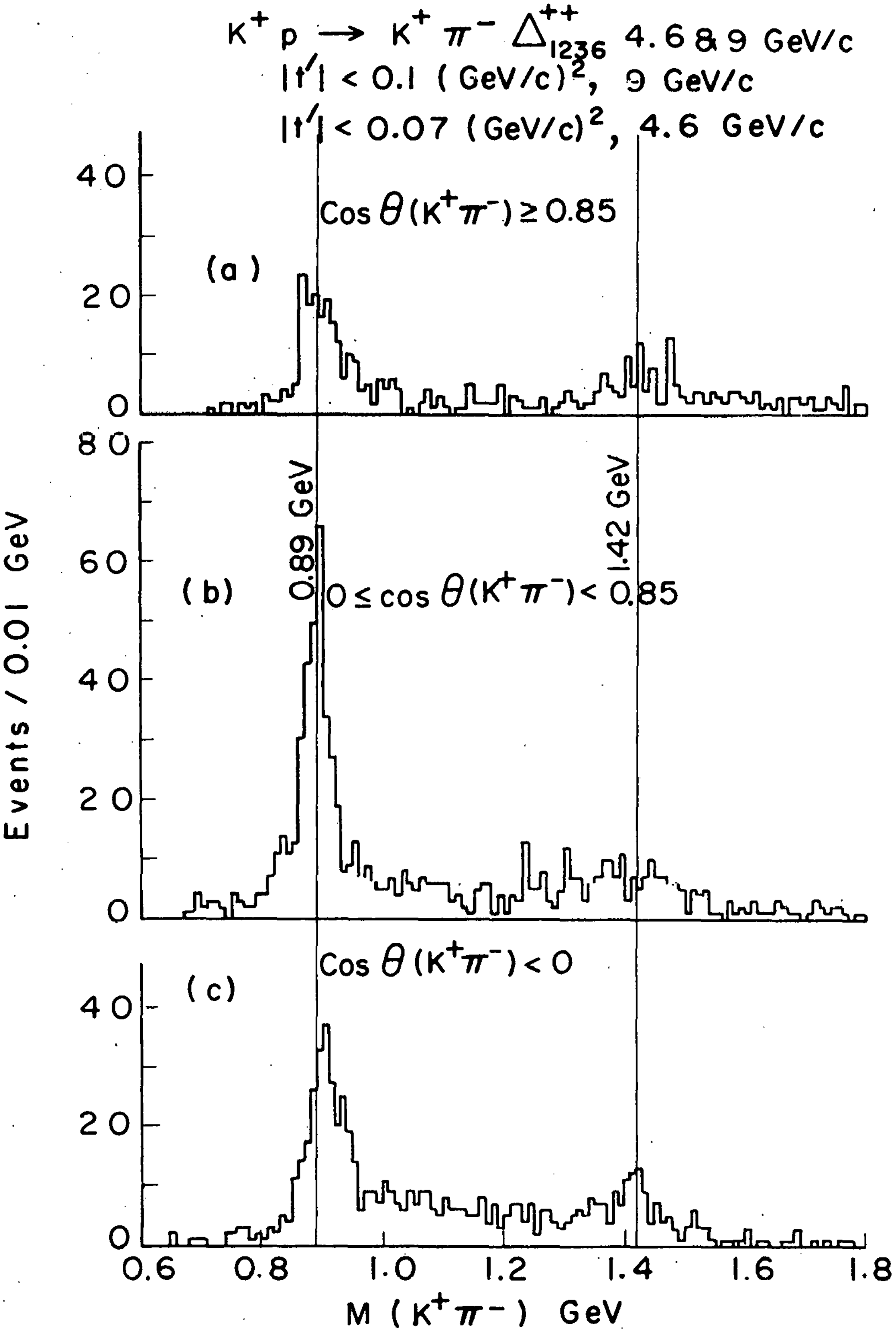

XBL705-2862

Fig. 58

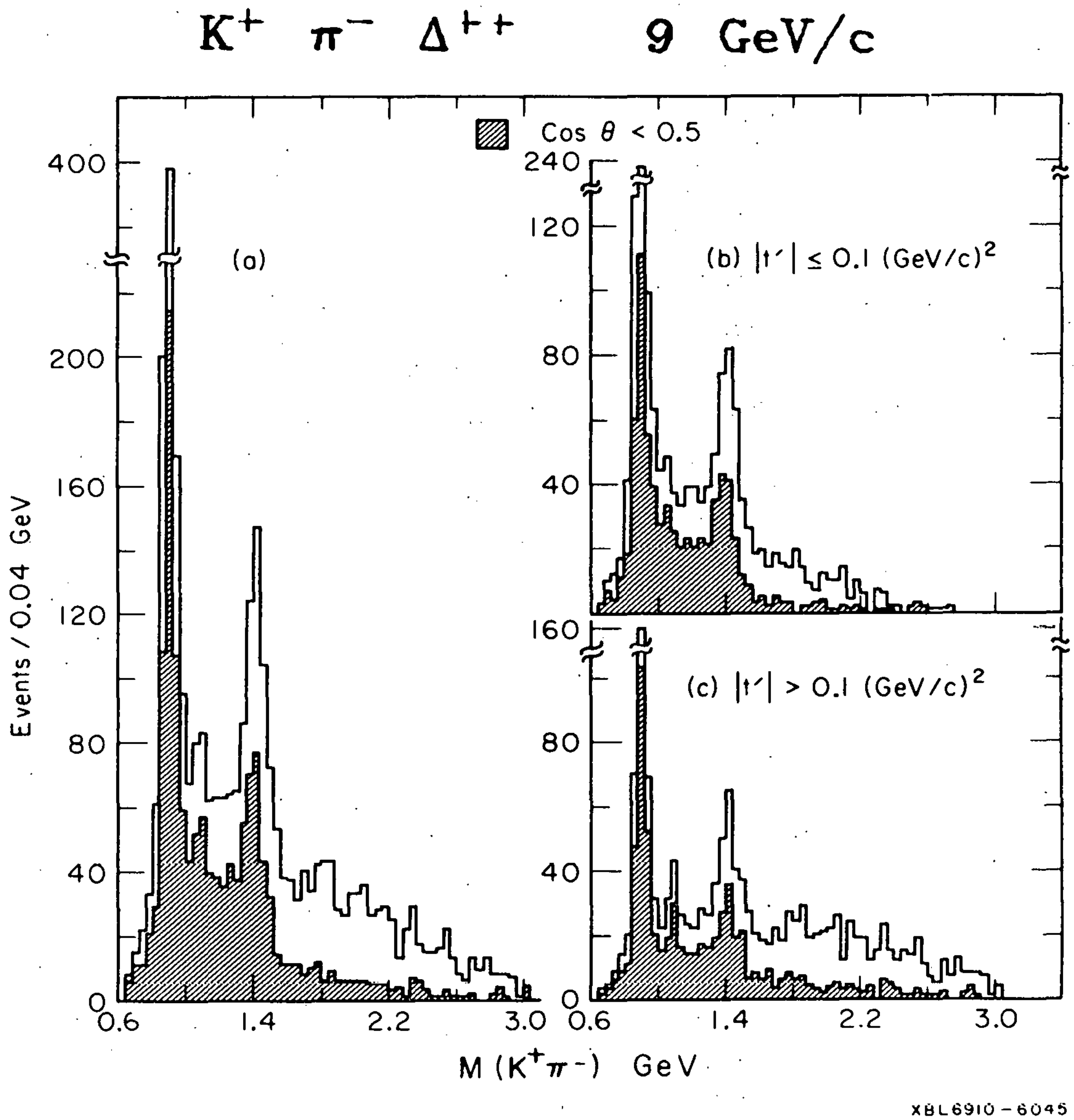

K+ π− Δ++ 9 GeV/c
Cos θ < 0.5
(a)
(b) |t′| ≤ 0.1 (GeV/c)²
(c) |t′| > 0.1 (GeV/c)²
Events / 0.04 GeV
400
200
160
120
80
40
0
240
120
80
40
160
80
40
0
0.6
1.4
2.2
3.0
0.6
1.4
2.2
3.0
M (K+π−) GeV
XBL6910-6045

Fig. 59

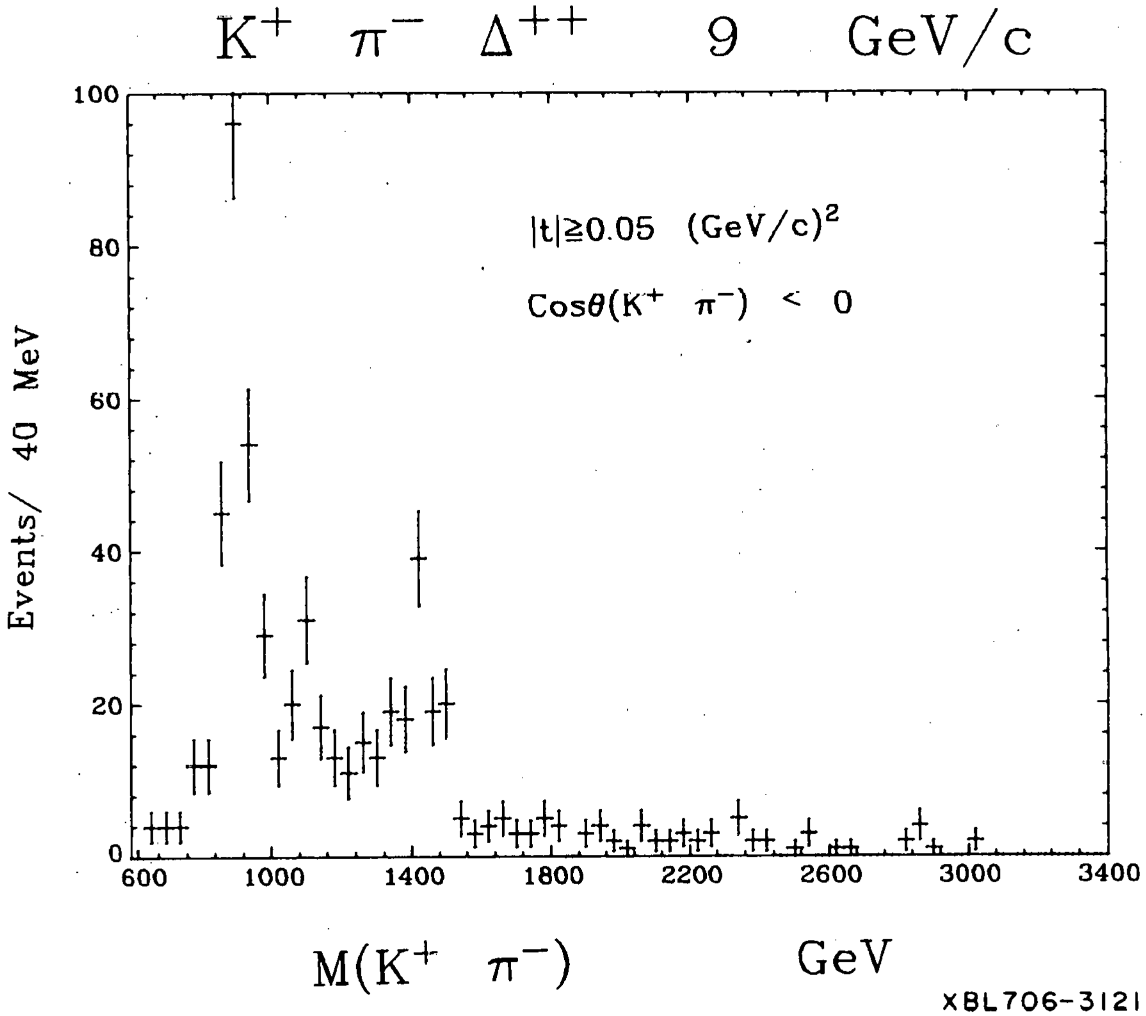

K+ π− Δ++ 9 GeV/c
|t|≧0.05 (GeV/c)2
Cosθ(K+ π−) < 0
Events/ 40 MeV
100
80
60
40
20
0
600
1000
1400
1800
2200
2600
3000
3400
M(K+ π−) GeV
XBL706-3121

Fig. 60

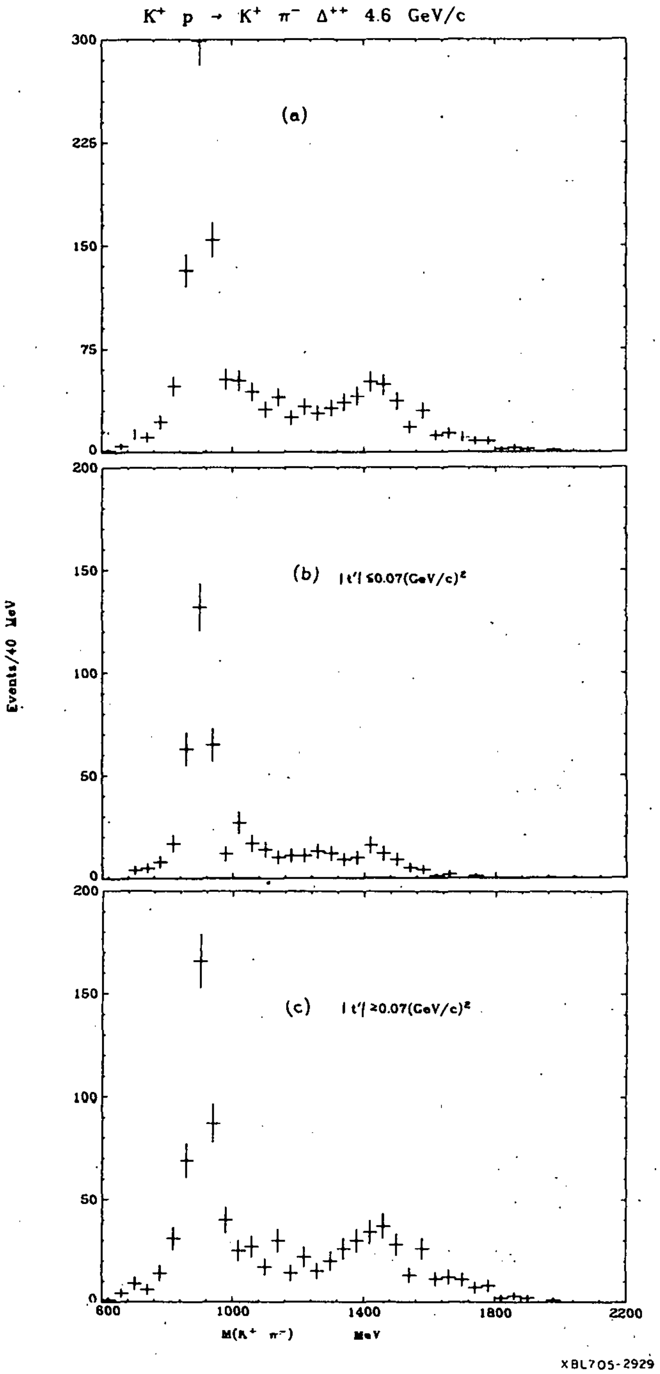

K⁺ p → K⁺ π⁻ Δ⁺⁺ 4.6 GeV/c
(a)
(b) |t'| ≤0.07(GeV/c)²
(c) |t'| ≥0.07(GeV/c)²
Events/40 MeV
M(K⁺ π⁻) MeV
XBL705-2929

Fig. 61

TECHNICAL INFORMATION DIVISION
LAWRENCE RADIATION LABORATORY
UNIVERSITY OF CALIFORNIA
BERKELEY, CALIFORNIA 94720